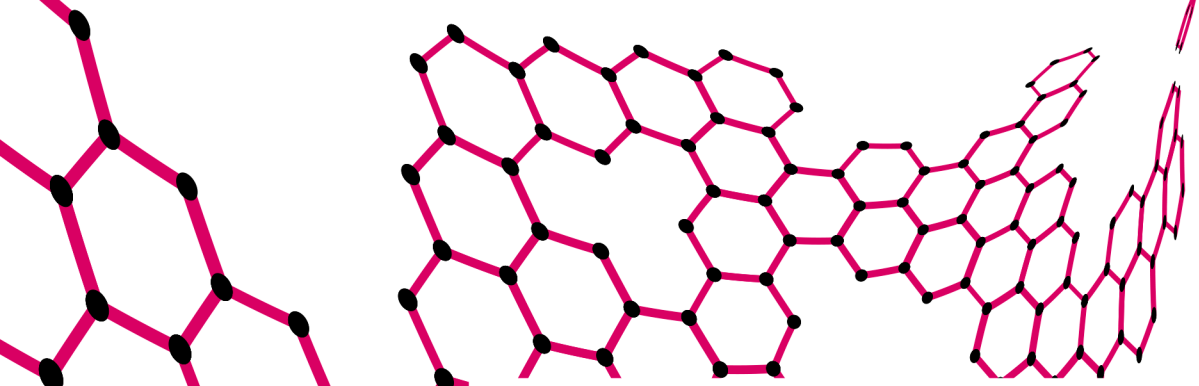

Master Thesis

Modelling of Fluid Flow and Mass Transfer in a Hollow-Fibre Membrane Oxygenator

by
Jaimy Gebbeken

Faculty of Engineering Technology
Program of Mechanical Engineering
Chair of Engineering Fluid Dynamics

Graduation committee

Prof. Dr. Ir. J. Arens	(chair)
Prof. Dr. Ir. W. Rohlfs	(supervisor)
Prof. Dr. A.R. Thornton	(internal member)
Ir. T.G. Vlogman	(external member)

December, 2023

UNIVERSITY OF TWENTE.

In loving memory of Sando and Pablo,

"The only, absolute and best friend a man has, in this selfish world, the only one that will not betray or deny him, is his dog."

— King Frederick II of Prussia, 1786.

Preface

Throughout my studies in mechanical engineering, a profound affinity for mathematics and the exploration of computational fluid dynamics consistently fueled my academic pursuits. These interests were a primary driving force in my decision to pursue a master's degree in mechanical engineering. This decision was further supported and encouraged by the daily supervisor of my first internship, Dr. A. Aydemir. His guidance extended far beyond the internship, and to this day, I continue to benefit from our fun and insightful discussions. While pursuing a master's thesis topic, I engaged in fruitful discussions with Prof. Dr. Ir. W. Rohlfs, particularly focusing on our interest in the modelling of various physical phenomena. In this regard, the topic of blood flow and oxygen transport came to the surface, as did the intricate nature of the fluid. Although not experienced with the biomechanical field of engineering, I was highly interested in understanding the fluid dynamics involved in the topic and decided to pursue it.

I would like to thank Prof. Dr. Ir. W. Rohlfs for his invaluable guidance during my master's assignment. The opportunity to delve into the mathematical modelling of blood flow phenomena under his supervision has been a rewarding academic experience and fueled my enthusiasm for the subject. I am particularly grateful for his unwavering support and excited about the prospect of extending my journey as a Ph.D. student after graduation.

I additionally would like to thank Prof. Dr. A.R. Thornton for his unwavering support, keen interest, and enthusiastic engagement with the myriad of mathematical topics that have unfolded both in the course of my assignment and during my personal explorations.

Finally, I wanted to thank my parents, brothers and their families, as well as the cherished pets of my parents. I am equally thankful to my numerous friends within and beyond the university for their unwavering support throughout my master's assignment.

December, 2023,

Jaimy Gebbeken

Summary

Hollow-fibre membrane oxygenators temporarily substitute lung function by facilitating blood oxygenation. These devices operate by a flow of blood through a container filled with thin, gas-permeable fibres. Oxygen within these fibres diffuses through the membrane directly into the bloodstream. The fibres are typically arranged in stacked or wrapped mats, facilitating relatively large inter-fibre spacings. In contrast to the length scales of the capillaries found in the lungs, these spacings are typically at least an order of magnitude greater than the size of red blood cells. At these length scales, particles such as red blood cells can migrate away from solid boundaries. This migratory behaviour results in a non-uniform distribution of the particles throughout the flow domain. While both the oxygenation of blood and the particle migration of red blood cells are extensively studied fields, the combination of both phenomena has yet to be considered in the extent of oxygenators. To this end, the main research question of this study was formulated as,

What is the effect of shear-driven particle migration, experienced by red blood cells, on the gas transfer of oxygen inside hollow-fibre membrane oxygenators?

In this thesis, an extensive review of available models for two-phase flows, blood rheology, particle migration, and oxygenation has been performed. The review allowed the establishment of well-founded considerations for the modelling of blood flow and oxygenation in membrane oxygenators. Blood can be considered a two-phase dispersed system whose flow inside membrane oxygenators is assumed to be laminar and that of a Stokesian suspension. Blood can now be modelled as a single-phase mixture with a non-Newtonian rheology. The primary rheological features considered for blood could be reduced to the sole consideration of its shear-thinning character, which depends on the local shear rate and particle concentration. The modelling of the migration of red blood cells could be done using a phenomenological model. This model considers the observation of migration to be dependent on hydrodynamic particle interactions and variations in mixture viscosity. Finally, the modelling of oxygenation was considered through a newly derived oxygenation model based on the theory of two-phase flows. The model considers the total mass of oxygen to be conserved, albeit dissolved in blood plasma or bound to the red blood cells. Numerically derived results indicate that the bulk flow behaviour of the red blood cells was the crucial factor in the observation of oxygenation resistances due to particle migration. In axisymmetric pipe flow, this is of great importance as the bulk flow exhibited significant increases in particle concentration. The observed differences between the migratory and non-migratory considerations showed a maximum of about 12% in mean flow oxygen saturation. However, these differences were not observed considering an oxygenator as a maximum value of about 1.56% was found. The particle concentration did show a significant change locally around the fibres. However, the bulk flow saw only slightly elevated concentrations.
Additionally, the influence of Newtonian rheology was studied. It showed differences in oxygen saturation up to about 9%, even considering an oxygenator. This observed be-

haviour could be related to the parametric fitting for the non-Newtonian viscosity model considered in this study and requires further research. Lastly, the considered oxygenation model showed an overestimation of oxygen saturation. This overestimation is linked to the omitted modelling consideration of interphasic oxygen transport, and a more accurate description of this behaviour warrants further research.
In conclusion, the influence of particle migration on the oxygenation of blood in hollow-fibre membrane oxygenators can typically be regarded as negligible.

Contents

Nomenclature **IX**

1 Introduction **1**
1.1 The Respiratory System and Gas Exchange in the Lungs . . . 1
1.2 Hollow-Fibre Membrane Oxygenators . . . 2
1.3 Particle Migration . . . 2
1.4 Research Goals . . . 3
1.5 Read Guide . . . 3

2 The Composition and Characteristic Properties of Whole Blood **5**
2.1 The Composition and Functions of Whole Blood . . . 5
2.1.1 Blood Plasma . . . 5
2.1.2 Blood Cells . . . 6
2.2 The Structure of Red Blood Cells . . . 6
2.2.1 Geometry . . . 6
2.2.2 Membrane . . . 7
2.2.3 Cytoplasm . . . 7
2.3 The Characteristic Behaviour of Red Blood Cells . . . 7
2.3.1 Aggregation . . . 7
2.3.2 Dynamical Cell Shapes . . . 8
2.3.3 Non-Uniform Spatial Distribution . . . 10
2.3.4 Sedimentation . . . 11
2.3.5 Thermal Agitation . . . 11
2.4 The Essential Modelling Properties of Whole Blood . . . 12

3 The Governing Relations of Immiscible Two-Phase Flows **13**
3.1 Single Phase Governing Relations . . . 13
3.2 Two-Phase Governing Relations . . . 14
3.2.1 Local-Instant Formulation . . . 14
3.2.2 Time-Averaged Formulation . . . 16
3.2.3 Mixture Formulation . . . 18
3.3 The Modelling of Two-Phase Flows . . . 20

4 Constitutive Modeling of Momentum in Dispersed Two-Phase Flows **21**
4.1 Two-Phase Flow Classifications . . . 21
4.2 Fluid Flow Classifications . . . 22
4.3 Dispersed Phase Inertia . . . 23
4.4 Phasic Stress Tensors . . . 24
4.4.1 Continuous Phase Stress Tensor . . . 24
4.4.2 Dispersed Phase Stress Tensor . . . 25

4.4.3 Mixture Stress Tensor . . . 26
4.5 Interphasic Interactions . . . 26
4.5.1 Macroscopic Phase Diffusion . . . 26
4.5.2 Interfacial Momentum Source . . . 27
4.5.3 Phase Diffusion Flux . . . 28
4.6 The Constitutive Modelling of Linear Momentum in Blood Flows . . . 28

5 The Rheology of Whole Blood 31
5.1 Rheology of Simple Particle Suspensions . . . 31
5.2 Shear-Thinning . . . 31
5.2.1 Cross Model . . . 33
5.2.2 Power-Law Model . . . 33
5.2.3 Sisko Model . . . 33
5.3 Extended Shear-Thinning Modelling . . . 33
5.3.1 Einstein-Like Models . . . 33
5.3.2 Carreau Type Models . . . 34
5.4 Thixotropy . . . 34
5.5 Viscoelasticity . . . 35
5.6 Viscoplasticity . . . 36
5.7 The Rheological Modelling of Whole Blood . . . 37

6 Shear-Induced Migration Modelling of Red Blood Cells 39
6.1 Mechanisms of Shear-Induced Migration . . . 39
6.1.1 Solid Boundary Presence . . . 39
6.1.2 Velocity Profile Curvature . . . 40
6.2 Shear-Induced Diffusion . . . 41
6.3 Shear-Induced Migration Modelling . . . 42
6.3.1 Suspension Balance Models . . . 43
6.3.2 Diffusive Flux Models . . . 43
6.4 Mathematical Model Equivalence . . . 44
6.5 The Constitutive Modelling of Shear-Induced Migration of Red Blood Cells 44

7 The Oxygenation of Blood in Hollow-Fibre Membrane Oxygenators 45
7.1 Membrane-Side Oxygen Transfer . . . 45
7.2 Blood-Side Oxygen Transfer . . . 46
7.2.1 Continuous Phase Diffusion . . . 46
7.2.2 Interphasic and Dispersed Phase Diffusion . . . 47
7.2.3 Oxygen Equilibrium, Co-operativity, and Affinity . . . 47
7.3 Oxygenation Modelling . . . 48
7.3.1 Effective Oxygen Diffusivity Model . . . 48
7.3.2 Micro-Scale Oxygenation Model . . . 49
7.3.3 Conservation of the Total Mass of Oxygen Model . . . 50
7.4 The Modelling of Oxygen Transport in Whole Blood . . . 50

8 Methodology 51
8.1 Governing Relations . . . 51
8.1.1 Blood Flow . . . 52
8.1.2 Oxygenation . . . 54
8.2 Boundary Conditions . . . 55
8.2.1 Mixture Mass and Momentum Conservation . . . 55

8.2.2 Phasic Mass Conservation . . . 56
8.2.3 Oxygen Mass Conservation . . . 56
8.3 Solver Characteristics . . . 57
8.3.1 Solution Algorithm . . . 57
8.3.2 Iterative Methods . . . 58
8.3.3 Numerical Schemes . . . 58
8.4 Numerical Domain . . . 59
8.4.1 Cyclic Pipe . . . 59
8.4.2 Axisymmetric Pipe . . . 60
8.4.3 Two-Dimensional Oxygenator . . . 60
8.5 Solver and Solution Verification . . . 61
8.5.1 Implementation Verification . . . 61
8.5.2 Migration Verification . . . 62
8.5.3 Oxygenation Verification . . . 62
8.5.4 Comparison Metrics . . . 63

9 Results and Discussion **65**
9.1 Implementation Verification . . . 65
9.2 Migration Verification . . . 66
9.2.1 The Steady-State Analytical Solution . . . 66
9.2.2 The Fåhræus Effect . . . 67
9.3 Oxygenation Verification . . . 68
9.4 The Influence of Particle Migration on Oxygenation in Axi-symmetric Pipe Flow . . . 69
9.4.1 Hydrodynamic Developed Profiles . . . 70
9.4.2 Oxygenation Boundary Layer Development . . . 71
9.4.3 Oxygenation Developed Saturation Behaviour . . . 73
9.4.4 Pipe Flow Core Particle Distribution-Induced Oxygenation Resistance 74
9.5 Fully Developed Particle Migration and Oxygenation in a Two-Dimensional Oxygenator . . . 76
9.5.1 Particle Migration Grid Sensitivity in a Cyclic Domain . . . 76
9.5.2 Shear Induced Particle Migration in a Cyclic Domain . . . 77
9.5.3 The Influence of Particle Migration on Oxygenation . . . 78
9.6 The influence of Newtonian Rheology and Particle Presence on Oxygenation in a Two-Dimensional Oxygenator . . . 79
9.6.1 The Influence of Newtonian Rheology . . . 80
9.6.2 The Influence of the Presence of Red Blood Cells . . . 81
9.7 Validity and Limitations of the Chosen Models . . . 81
9.7.1 The Mixture Formulation Consideration of Whole Blood . . . 81
9.7.2 Comparative Study of Oxygen Transport Governed by Mixture Formulation Oxygenation Models . . . 82

10 Conclusions and Recommendations **85**

Appendices **95**

A Conservation of the Total Mass of Oxygen **97**
A.1 Introduction . . . 97
A.2 Total Mass of Oxygen . . . 97
A.3 Mixture Conservation . . . 99

A.4 Constitutive Modelling of the Oxyhaemoglobin . . . 99
A.5 Constitutive Modelling of the Molecular Diffusion . . . 101
A.6 Constitutive Modelling of the Phase Diffusion . . . 102
A.7 Conservation of the Total Mass of Oxygen . . . 102
A.8 Model Derivation Verification . . . 103
A.8.1 Dimensions . . . 103
A.8.2 Limiting Behaviour . . . 104

B Solver Implementation Verification 105
B.1 Introduction . . . 105
B.2 The Method of Manufactured Solutions . . . 105
B.3 Manufactured Solutions . . . 106
B.3.1 Taylor-Green Vortex Flow . . . 106
B.3.2 Mixture Kinematic Pressure . . . 107
B.3.3 Dispersed Phase Volume Fraction . . . 107
B.3.4 Oxygen Partial Pressure . . . 107

C OpenFOAM Code Implementations 109
C.1 Governing Relations . . . 109
C.1.1 Conservation of Mixture Momentum . . . 109
C.1.2 Conservation of Dispersed Phase Mass . . . 109
C.1.3 Conservation of Oxygen mass . . . 110
C.2 Boundary Conditions and Source Terms . . . 110
C.2.1 Newtonian Inlet Velocity . . . 110
C.2.2 No-Penetration Boundary Condition . . . 110
C.2.3 Cyclic Mixture Momentum Source . . . 112
C.3 Closure Models . . . 113
C.3.1 Mixture Shear Rate Magnitude . . . 113
C.3.2 Yeleswarapu-Wu Mixture Viscosity . . . 113
C.3.3 Hill Equation . . . 113

D Additional Blood Flow Modelling Considerations 115
D.1 Interphasic Interactions . . . 115
D.1.1 Two-Fluid Model Interphasic Interactions . . . 115
D.1.2 Drag Force . . . 116
D.1.3 Virtual Mass Force . . . 116
D.1.4 Drift-Flux Model Interphasic Interactions . . . 116
D.2 Rheology of whole blood . . . 117
D.2.1 Thixotropy . . . 117
D.2.2 Viscoelasticity . . . 118
D.2.3 Viscoplasticity . . . 118
D.3 Shear-Induced Migration Modelling of Red Blood Cells . . . 118
D.3.1 Lift Force-Based Migration Modelling . . . 118
D.3.2 Mathematical Model Equivalence . . . 119

Nomenclature

Latin Characters

$\boldsymbol{\mathcal{I}}$	Identity matrix	
$\boldsymbol{\mathcal{J}}$	Boundary flux vector	
$\boldsymbol{n}$	Outward unit normal vector	
$\mathcal{C}$	Curve	
$\mathcal{F}$	Arbitrary function	
$\mathcal{I}$	Interfacial source	
$\mathcal{S}$	Volumetric source	
$\mathcal{X}$	Phase indicator function	
C	Model or proportionality coefficient	

Dimensioned Latin Characters

$\boldsymbol{\mathcal{D}}$	Strain-rate tensor	$[1/\mathrm{s}]$
$\boldsymbol{g}$	Gravitational acceleration	$\left[\mathrm{m}^2/\mathrm{s}\right]$
$\boldsymbol{q}$	Heat flux	$\left[\mathrm{W}/\mathrm{m}^2\right]$
$\boldsymbol{u}$	Velocity	$[\mathrm{m}/\mathrm{s}]$
$\boldsymbol{V}$	Relative phase velocity	$[\mathrm{m}/\mathrm{s}]$
$\boldsymbol{x}$	Position	$[\mathrm{m}]$
a	Characteristic particle size	$[\mathrm{m}]$
D	Diameter	$[\mathrm{m}]$
G	In-plane shear modulus	$[\mathrm{N}/\mathrm{m}]$
k_B	Boltzmann constant	$\left[\mathrm{m}^2 \cdot \mathrm{kg}/(\mathrm{s}^2 \cdot \mathrm{K})\right]$
L	Characteristic length	$[\mathrm{m}]$
p	Pressure	$[\mathrm{Pa}]$
R	Radius	$[\mathrm{m}]$
T	Temperature	$[\mathrm{K}]$
t	Time	$[\mathrm{s}]$
U	Characteristic velocity	$[\mathrm{m}/\mathrm{s}]$

Greek Characters

Ω	Domain	
$\partial\Omega$	Boundary	
ϕ	Arbitrary quantity	

Dimensioned Greek Characters

α	Local void fraction	$[-]$
$\boldsymbol{\sigma}$	Cauchy stress tensor	$\left[\mathrm{N/m^2}\right]$
$\boldsymbol{\tau}$	Viscous stress tensor	$\left[\mathrm{N/m^2}\right]$
$\dot{\gamma}$	Shear rate magnitude	$[1/\mathrm{s}]$
λ	Second coefficient of viscosity	$[\mathrm{Pa \cdot s}]$
μ	Dynamic viscosity	$[\mathrm{Pa \cdot s}]$
ν	Kinematic viscosity	$\left[\mathrm{m^2/s}\right]$
ρ	Mass density	$\left[\mathrm{kg/m^3}\right]$
σ	Surface tension	$[\mathrm{N/m}]$
τ	Characteristic time scale	$[\mathrm{s}]$
φ	Haematocrit, volume fraction of red blood cells in whole blood	$[-]$

Superscripts

$\widetilde{(.)}$	Favre averaged quantity
$\overline{\overline{(.)}}$	Phase averaged quantity
$\prime$	Fluctuating component
$\overline{(.)}$	Time averaged quantity
D	Phase diffusion quantity
d	Discharge quantity
T	Turbulent quantity
t	Tube quantity

Subscripts

0	Reference or zero limit quantity
∞	Infinite limit quantity
c	Continuous
d	Dispersed
I	Interface
j	Volumetric
k	Phase index

m Mixture

p Particulate

r Relative

Dimensionless Numbers

Ca Capillary

Pe Péclet

Re Reynolds

St Stokes

Abbreviations

CO_2 Carbon dioxide

Hb Haemoglobin

HbO_2 Oxyhaemoglobin

O_2 Oxygen

BP Blood plasma

CFD Computational Fluid Dynamics

HFMO Hollow-fibre membrane oxygenator

RANS Reynolds-averaged Navier-Stokes

RBC Red blood cell

vol% Volume percentage

WBC White blood cell

Chapter 1

Introduction

The blood that runs through our veins is a complicated fluid that serves an important function, namely, the transportation of oxygen throughout our bodies. This transportation is primarily fulfilled by the red blood cells suspended in the flow of blood. These cells are abundant in blood and give the fluid its distinctive red colour through an iron-rich protein in the cell known as haemoglobin. This protein makes up about a third of the cell and is the protein to which the oxygen is allowed to bind to facilitate transportation throughout the body.

1.1 The Respiratory System and Gas Exchange in the Lungs

The respiratory system is the well-oiled machine in our bodies that efficiently ensures the oxygen we breathe is loaded into the bloodstream while excreting the carbon dioxide from our system. Upon inhalation, oxygen enters the lungs and traverses the tracheobronchial tree, a branching network that extends into both lungs, facilitating gas distribution. Inside the lung, the tree contains several small successive pathways known as bronchioles through which the air is distributed [19]. Each pathway is shorter and narrower than the last and ends in a collection of tiny air pockets known as the alveoli. The tiny alveoli are covered in narrow blood veins denoted capillaries. These capillaries are generally sufficiently small, so red blood cells are forced to flow through them individually, also known as single-file red blood cell motion [95]. This type of blood flow inside the capillaries, combined with their high density around the alveoli, ensures an efficient oxygen transfer between the lungs and the bloodstream. A bronchiole with several alveoli and a close-up of the gas transfer basics between a single alveoli and capillary are illustrated in figure 1.1.

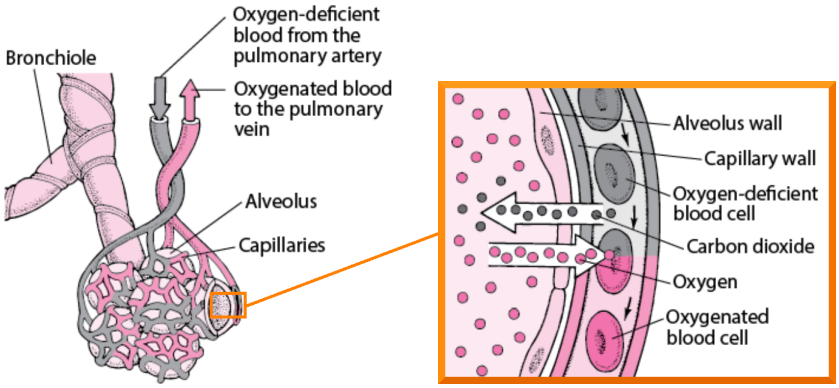

(a) Bronchiole (b) Alveoli

Figure 1.1: Gas exchange between alveolus and capillaries, adapted from [27].

1.2 Hollow-Fibre Membrane Oxygenators

In some instances, such as cardiovascular surgery, the oxygenation of our blood should be performed artificially. An important technique used in this regard is the cardiopulmonary bypass. This procedure temporarily takes over the oxygenation and circulation of blood during surgery on the heart and great blood vessels [91]. The oxygenation is accomplished through a heart-lung machine, which circulates the blood outside the body. The machine typically consists of four main components: a reservoir, pump, heat exchanger, and oxygenator [24]. The oxygenator component is then where the exciting physics of blood oxygenation happens and replicates the behaviour of the respiratory system.
One of the most popular and widely regarded oxygenator types is the hollow-fibre membrane oxygenator (HFMO) [49] illustrated in figure 1.2. This type of oxygenator is designed to mimic the natural gas exchange process in the lungs and functions by having blood flow through a container filled with thin, flexible, gas-permeable fibres [24]. These fibres are generally knitted into fibre mats, stacked at various angles or wrapped around an inner core at various angles [93]. The knitting process is a cost-effective manufacturing method that, due to the flexibility of the fibres, introduces random inter-fibre distances. These distances generally exceed the typical length scales of lung capillaries by at least an order of magnitude, and their randomness plays a crucial role in enhancing the efficiency of the oxygenation process.

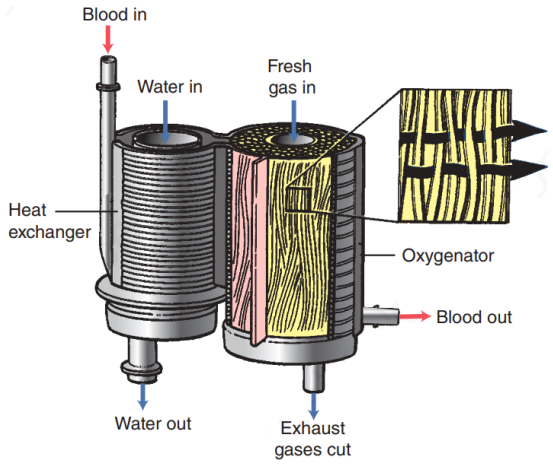

Figure 1.2: A hollow-fibre membrane oxygenator with wrapped fibres and heat exchanger unit, adopted from [24].

1.3 Particle Migration

Compared to the typical capillary size, the relatively large inter-fibre distances found in hollow-fibre membrane oxygenators allow the red blood cells to move away from the fibres. This process is known as shear-induced particle migration and is a well-studied phenomenon observed for generic particle suspensions and blood flows [104]. The red blood cells will concentrate in regions with low velocity gradients, such as the central line in pipe flow, causing a non-uniform spatial distribution. Under the right conditions, this migratory behaviour is sufficiently severe to deplete the boundary region entirely. This depleted layer is commonly referred to as the cell-free layer (CFL) and is primarily composed of the suspending fluid [22], known as blood plasma. The formation of the cell-free layer may also induce cell margination of white blood cells and platelets. This phenomenon denotes the opposing behaviour observed by the white blood cells and platelets upon red blood

cell migration. The cell-free layer, migration, and margination are illustrated in figure 1.3. The cell-free layer is influential to both the fluid flow and blood oxygenation. The smaller amount of red blood cells causes a reduction in the apparent viscosity [33], which denotes the observed viscosity when considering blood as a whole, or whole blood. This reduction is caused by the typically lower viscosity of the depleted blood plasma, which effectively lubricates the flow of the concentrated blood [104]. Additionally, the depleted layer may hinder the oxygen uptake of whole blood as the oxygen must first diffuse through before it starts saturating the cells.

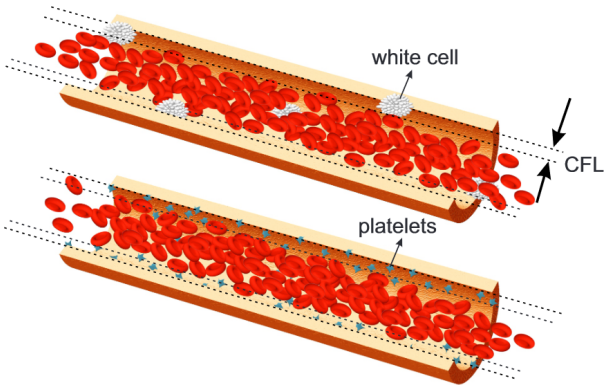

Figure 1.3: The cell-free layer and margination of white blood cells and pipe flow, adopted from [104].

1.4 Research Goals

Macroscopic continuum scale computational fluid dynamics (CFD) is a commonly considered tool in designing and researching blood flow in hollow-fibre membrane oxygenators. Typically, these studies are focused on identifying low flow velocity regions where the potential of blood clot formation is high [93]. Alternatively, at the fibre scale, the numerical investigations focus on understanding gas transport around the fibres. The aim of these studies is to understand the effect of fibre configurations [45, 51], or investigate the feasibility of new membrane geometries [29, 42]. However, these studies consider a uniform red blood cell distribution throughout the numerical domain. The uniform distribution effectively neglects the potential oxygenation resistance introduced by the cell-free layer. The influence exerted on the oxygenation by the migratory behaviour is the main interest of this study, and to this end, the main research question is formulated as follows:

What is the effect of shear-driven particle migration, experienced by red blood cells, on the gas transfer of oxygen inside hollow-fibre membrane oxygenators?

1.5 Read Guide

The modelling of blood flow is an exciting but rather complicated topic. The response of the fluid depends on the flow classifications and geometry under consideration. This requires a tailored approach to ensure the flow behaviour is accurately described, all behaviour of interest is modelled, and no effects are accounted for multiple times. First, the composition and characteristic properties of whole blood are studied in chapter 2 to understand what behaviour and effects are of interest for hollow-fibre membrane oxygenators. The composition of interest showed that blood can consist of two components: blood

plasma and suspended red blood cells. The fluid flow of such suspensions is governed by conservation laws for immiscible two-phase flows. The derivation of these governing relations required some extra care than those for single-phase flows and are presented in chapter 3.
The generic conservation laws are tailored to the problem of interest through constitutive modelling. These constitutive models should accurately describe the characteristics uncovered in chapter 2, and their considered formulations are discussed in chapter 4. While the basics of the constitutive modelling are introduced in chapter 4, the closure for the momentum equations required some additional care. This is necessary to adequately describe the non-Newtonian behaviour of the suspension and is discussed in chapter 5.
With the basics of blood flow modelling discussed, the attention can be shifted towards understanding particle migration. The mechanisms driving the interesting behaviour and the primary modelling considerations of the phenomenon are discussed in chapter 6.
The final literature to be considered is the oxygen transport from the oxygenator into the blood flow. The oxygen transfer and binding to the red blood cells are discussed in chapter 7, followed by a discussion of the commonly considered oxygenation models. Additionally, in this chapter, a newly derived model is presented to describe the oxygenation process of migrating blood and its derivation is provided in appendix A.
The methodology considered in this study to provide an answer to the main research question is presented in chapter 8. The results are presented and discussed in chapter 9, and finally, the conclusions of the current study and recommendations for further research are provided in chapter 10.

Chapter 2

The Composition and Characteristic Properties of Whole Blood

Blood as a whole is an intricate and multi-faceted fluid whose fluid dynamical properties are strongly related to its particulate nature. The study of these properties and the resulting behaviour is denoted haemodynamics, where its precise consideration varies depending on the flow domain and regime under consideration. This chapter delves into the fundamental composition and characteristic properties of blood from a physical point of view, followed by simplifying considerations for the flow typical to hollow-fibre membrane oxygenators.

2.1 The Composition and Functions of Whole Blood

The circulatory system relies on blood, a vital bodily fluid that serves numerous essential functions required to maintain the overall health and functionality of the body. This fluid consists of an aqueous liquid base known as blood plasma (BP), wherein various deformable cellular elements are densely suspended. Together, these constituents are commonly referred to as whole blood, and this section aims to introduce them and highlight their essential features.

2.1.1 Blood Plasma

Blood plasma accounts for approximately 55-60 volume percentage (vol%) of whole blood and is a light-yellow coloured fluid. It comprises approximately 91-92 vol% of water and 8-9 vol% of solids. These solids include clotting proteins, plasma proteins, electrolytes, antibodies, and waste products [90].
The solids suspended in BP were found to introduce a kind of borderline non-Newtonian behaviour, as observed by Rodrigues et al. [90]. However, because BP primarily consists of water, it is usually thought to behave like an incompressible Newtonian fluid [57].
Additionally, an essential functionality of BP for both bodily health and the fluid flow of whole blood is coagulation, which is a part of the hemostasis process. Coagulation facilitates the formation of blood clots in the event of blood vessel damage and is initiated by a complex cascade of signalling through chemical messengers [107]. These messengers activate the clotting proteins in BP, such as fibrinogen, which convert into long, thin, and sticky proteins that can capture the blood cells and effectively create the blood clot.

2.1.2 Blood Cells

The blood cells in whole blood consist of three primary types, each with its specialized functions:

1. **Red Blood Cells (Erythrocytes, RBCs):** Red blood cells are the most abundant cell type in whole blood, accounting for approximately 99 vol% of all blood cells [107]. Their primary function is to transport oxygen (O_2) from the lungs to various tissues and organs and to carry the carbon dioxide (CO_2) back to the lungs [93].
2. **White Blood Cells (Leukocytes, WBCs):** White blood cells play a crucial role in the immune system of the body, protecting it from infections and foreign invaders [104]. Unlike red blood cells, white blood cells have a nucleus and are fewer in number, constituting less than one vol% of whole blood.
3. **Platelets (Thrombocytes):** Platelets are essential in the coagulation process, as they initiate clot formation [107]. These small cells are more numerous than white blood cells but are still significantly outnumbered by red blood cells [104].

In conclusion, whole blood primarily consists of red blood cells that are densely dispersed in an aqueous liquid, or more generally, in a Newtonian fluid [57, 104]. As a result, it is commonly assumed that whole blood is a two-phase system consisting solely of these two components when there is no particular interest in the other constituents [11].

2.2 The Structure of Red Blood Cells

The abundance of red blood cells suspended in the Newtonian fluid phase suggests that the cells impact the fluidic behaviour of whole blood. This impact is amplified by the unique structure of the cells, characterized by a flexible outer membrane with a viscous inner liquid. This section aims to introduce the generic structure and geometry of the cells in more detail.

2.2.1 Geometry

The characteristic geometric shape of the red blood cell is that observed for a healthy cell in stasis, which is typically biconcave and disc-like, generally referred to as discocyte [107]. The cell shape is illustrated in figure 2.1, has an average diameter of approximately 7.5 µm and a thickness varying between $1 - 2$ µm [104]. These characteristic dimensions allow the RBCs to be considered non-colloidal particles, which allows the negligence of colloidal interactions acting on the blood cells such as van der Waals or electrostatic forces.

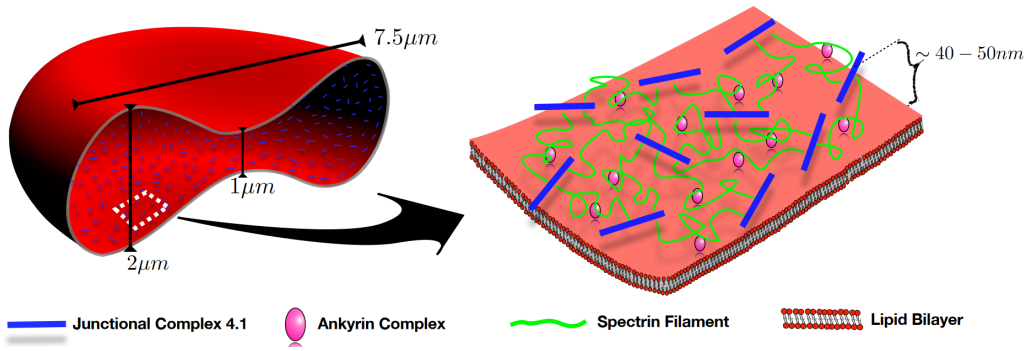

Figure 2.1: An illustration of the red blood cell geometry and the cell membrane structure, adopted from [104].

The volume and surface area of the RBC are, however, observed to decrease throughout the relatively short lifetime of the cell. This shrinkage is caused by a loss of cytoplasm, which is the viscous inner liquid [104]. The resulting averaged volume and surface area throughout the lifetime of the cell are respectively $94\,\mu m^3$ and $135\,\mu m^2$.

2.2.2 Membrane

The membrane of a red blood cell exhibits a complex composite structure that plays a crucial role in maintaining the integrity and deformability of the cell. It consists of a lipid bilayer, which can be considered as an incompressible two-dimensional fluid, supported by a network of long spectrin filaments [104]. This composite structure allows RBCs to undergo large deformations while maintaining a constant surface area. The complex structure, along with the network of spectrin filaments, can be observed on the right-hand side of figure 2.1.

2.2.3 Cytoplasm

The cytoplasm of a red blood cell refers to the fluid content enclosed by the membrane. The fluid primarily consists of an incompressible Newtonian solution of haemoglobin proteins [55], which are responsible for the transport of oxygen in the cells [104]. The dynamic viscosity of the cytoplasm, characterized by the haemoglobin concentration, is typically around five times higher compared to that of the surrounding blood plasma, and are respectively approximately $5.91 \times 10^{-3}\,\mathrm{Pa \cdot s}$ [50] and $1.23 \times 10^{-3}\,\mathrm{Pa \cdot s}$ [92]. This significant viscosity difference between the cytoplasm and BP plays a crucial role in the dynamics and deformability of the RBCs and generally elevates the apparent viscosity of whole blood [98].

In conclusion, red blood cells are non-colloidal, non-idealistically shaped, deformable particles filled with a highly viscous fluid compared to the surrounding blood plasma. Considering their abundance in whole blood, as discussed in the previous section, this combination of characteristics suggests the potential for complex rheological behaviour, which will be discussed in further detail in chapter 5.

2.3 The Characteristic Behaviour of Red Blood Cells

The preceding sections demonstrated the importance of whole blood and the intricate structure of the red blood cells within whole blood. The complicating geometry, consisting of a flexible outer membrane and a viscous inner liquid, illustrated the potential for an intricate fluid dynamical response to the fluid flow of blood. The characteristic behavioural responses to the fluid flow observed for red blood cells are discussed in this section in more detail.

2.3.1 Aggregation

Healthy red blood cells generally show two types of aggregation: blood clot and rouleaux formation. The blood clot formation was briefly discussed in section 2.1 and is essential during blood vessel damage and blood contact with foreign material [24]. Rouleaux, on the other hand, are coin-stack-shaped aggregates which can form in blood when fluid stresses are sufficiently low and may reversibly break apart as these stresses increase [90, 107]. These structures can also be observed without blood vessel damage, and their general structure is depicted in Figure 2.2.

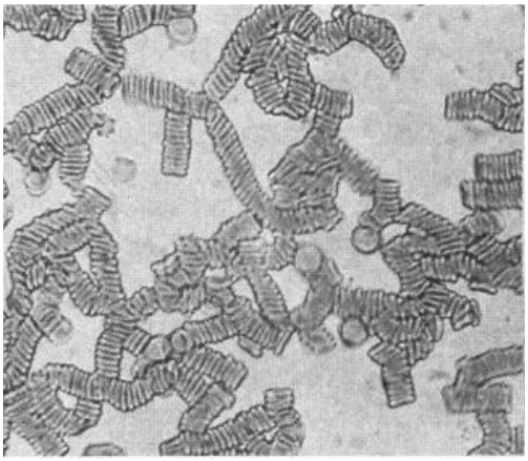

Figure 2.2: A snapshot of rouleaux in healthy blood, adopted from [32].

The aggregation of RBCs into rouleaux is driven by two prevailing theories: the 'bridging' hypothesis, where adsorbed proteins physically cross-link adjacent RBCs, and the 'depletion' hypothesis, where a depletion layer near the RBC surface leads to osmotic pressure driving RBC surfaces together [11]. The cross-linked proteins mentioned in the first hypothesis refer to the clotting proteins dissolved in the blood plasma, such as fibrinogen. This protein is crucial for the observation and behaviour of rouleaux, as the formation of these microstructures would not be observed without it [107]. On the other hand, increased levels of fibrinogen, which can be associated with cardiac diseases or sepsis [17], contribute to the resilience of rouleaux against fluid stresses. This heightened concentration of fibrinogen enhances the stability and structural integrity of rouleaux, allowing them to withstand higher shear forces and maintain their cohesive nature [89, 104].

2.3.2 Dynamical Cell Shapes

The deformable nature of the red blood cells allows for interesting behaviour and numerous stable cell membrane shapes observed in simple shear flow of red blood cell suspensions at varying shear rates. The shear rate is defined as the gradient in the velocity normal to the flow direction and planar to the vorticity direction. A variety of shapes and their relation to the flow characteristics are discussed in this section.

2.3.2.1 Isolated Cell Dynamics in a Viscous Fluid

The deformation of red blood cells suspended in a viscous fluid has been studied for relatively low shear rates as early as the 1960s and showed flipping and tank-treading behaviour [104]. The suspending viscous fluid was used to mimic the elevated viscosity of whole blood compared to that of blood plasma [57], due to the presence of RBCs containing the highly viscous cytoplasm as discussed in section 2.2.3.
The flipping behaviour was generally observed for lower shear rates and resembles the behaviour of rigid discs in a pure shear flow [104]. The general behaviour can be observed in figure 2.3, and shows that the cells flip around the major axis of the discocyte shape.

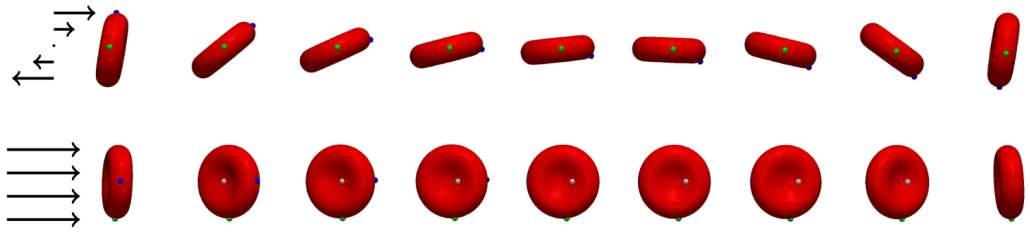

Figure 2.3: Red blood cell flipping in shear flow, adopted from [104]

The RBC starts to tank-tread at higher shear rates. Tank-treading is where the membrane starts to revolve around the inner cytoplasm and may even elongate in the direction of the flow at high shear rates [104]. The tank-treading motion observed for an elongated cell can be observed in figure 2.4.

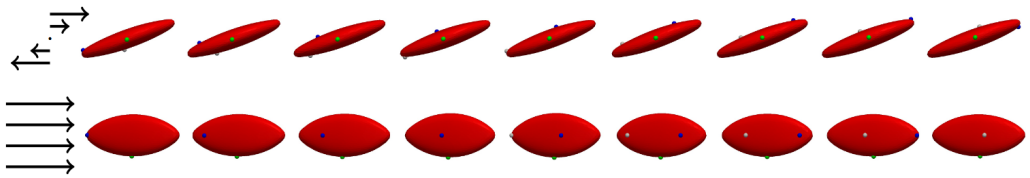

Figure 2.4: Red blood cell tank-treading in shear flow, adopted from [104]

2.3.2.2 Isolated Cell Dynamics in Blood Plasma

More recent studies, [57, 67], have shown that the red blood cells, in reality, show a richer range of stable cell shapes when considering cells suspended in a fluid with a viscosity closer to that of actual blood plasma. This extended range shows that the viscosity ratio between the cytoplasm and the BP plays a crucial role in the local dynamics of whole blood. Different cell shapes and cell dynamics can thus be observed over a range of shear rates for isolated RBCs. The shapes range from the standard discocyte and the similar stomatocyte, a disc with only a single concave side, shapes at low shear rates to highly deformed multi-lobed cells at high shear rates. The shapes for various shear rates and the probability of observation can be seen in figure 2.5, which were derived using physical and numerical considerations of the characterizing flow. The figures show that, as the shear rate increases, the observation of highly distorted cells becomes more probable. Additionally, the standard discocyte shape is rarely observed at shear rates in the range where trilobes and hexalobes cells are mainly observed.

2.3.2.3 Cell Dynamics in Dense Suspensions

The previously considered blood cell shapes were observed for isolated cells, such that the influence of cell interactions were effectively neglected. This consideration is far from the truth when considering the blood flow in an oxygenator. The dynamics of the red blood cells change drastically as the amount of blood cells in the flow increases. The cells then show an increased probability for two new shapes, multilobes and creased discocytes [57]. The two shapes can respectively be observed in figure 2.6a and 2.6b. The multilobes behave similarly to the earlier discussed trilobes and hexalobes, whereas the creased discocytes are flattened cells characterized by grooves and creases.

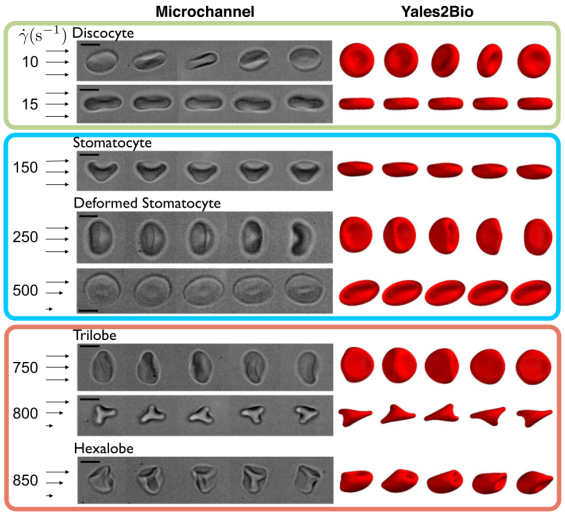

(a) Physcially and numerically observed cell shapes at various shear rates.

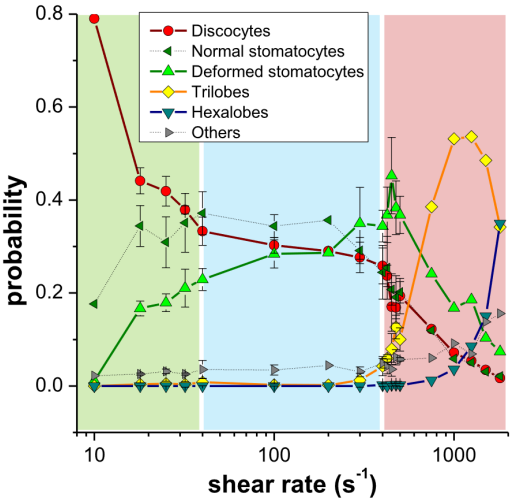

(b) Cell shape observation probability as a function of shear rate.

Figure 2.5: Isolated cell dynamics in blood plasma, adopted from [57].

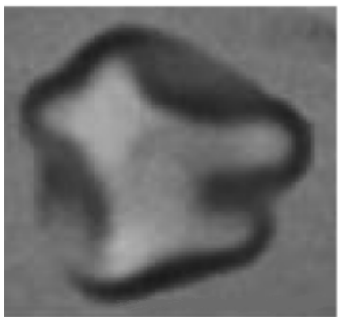

(a) Multilobe.

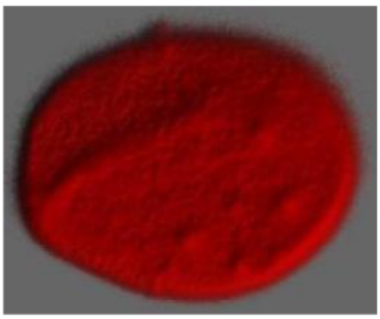

(b) Creased discocyte.

Figure 2.6: Cell dynamics in dense suspensions, adopted from [57].

2.3.3 Non-Uniform Spatial Distribution

The particulate nature of blood gives rise to non-uniform distributions of fluid properties closely tied to the spatial configuration of red blood cells. These alterations in spatial configuration arise from the migratory behaviour of RBCs in the vicinity of solid boundaries [104], and they become particularly prominent for domain sizes below 300 µm [33]. The details of the migration mechanics and modelling thereof will be discussed further in chapter 6, whereas two essential and closely related effects observed due to this non-uniform configuration are discussed here, the Fåhræus and Fåhræus-Lindqvist effects [6].

2.3.3.1 Fåhræus Effect

The Fåhræus effect was originally observed for blood flow in a glass tube by Fåhræus [32]. This effect illustrates that when a small capillary is placed between two larger vessels, the haematocrit discharged from the capillary is larger than the haematocrit observed inside the capillary [4]. The two quantities are, respectively, commonly denoted the discharge and tube haematocrit, where haematocrit refers to the volume fraction of the red blood cells in whole blood [104]. This observation is generally attributed to the lateral migration of

the RBCs towards the centre of the capillary, which allows the formation of a cell-free film near the boundary [7]. The ratio of the tube and discharge haematocrit was empirically observed to decay rapidly for decreasing tube radii and was observed by Pries et al. [86] to obey the empirical relation denoted by,

$$\frac{\varphi^t}{\varphi^d} = \varphi^d + (1-\varphi^d)(1 + 1.7e^{-0.35D} - 0.6e^{-0.01D}). \tag{2.1}$$

Where φ denotes the haematocrit, D the tube diameter in microns, and the super-scripted t and d, respectively, tube and discharge. The relation can be rewritten as an expression for the discharge haematocrit in terms of the tube haematocrit as follows,

$$\varphi^d = -\frac{D^*}{2(1-D^*)} + \left[\left(\frac{D^*}{2(1-D^*)}\right) + \frac{\varphi^t}{(1-D^*)}\right]^{\frac{1}{2}}, \tag{2.2}$$

where,

$$D^* = 1 + 1.7e^{-0.35D} - 0.6e^{-0.01D}. \tag{2.3}$$

2.3.3.2 Fåhræus–Lindqvist Effect

The closely related Fåhræus–Lindqvist effect illustrates a reduction in the apparent viscosity of whole blood as the capillary size decreases [33]. This effect is, similarly to the Fåhræus effect, attributed to the non-uniform distribution of the red blood cells and the formation of a cell-free layer near the solid boundary for small domains.

2.3.4 Sedimentation

In section 2.2.3, it was discussed that the elevated viscosity of the interior fluid of the red blood cells, cytoplasm, plays a role in the overall fluid dynamics of blood. Next to an elevated viscosity the cytoplasm also features an increased fluid density of approximately $1110\,\mathrm{kg/m^3}$ [76] compared to the fluid density of blood plasma of approximately $994\,\mathrm{kg/m^3}$ [105]. This density difference causes the RBCs to sediment in the direction of gravity at low flow rates [104].

2.3.5 Thermal Agitation

In the previous sections, the importance of the hydrodynamic interactions of the red blood cells has been demonstrated in the overall fluidic behaviour of whole blood. These interactions are not of sole importance in the consideration of particle suspension in general. In section 2.2, it was briefly discussed that colloidal interactions may also be of interest and that the characteristic size of red blood cells allows the negligence of their consideration. Additionally, the thermal agitation of red blood cells can be left out of consideration, such that whole blood can be considered as a non-Brownian suspension. This classification effectively allows the consideration of the rheology of blood, further discussed in chapter 5, to be invariant to the changes in temperature. Thermal agitation is generally important when the particulate Péclet number is of order $\mathrm{Pe}_p \lessapprox 10^3$, whereas for blood, it is generally of order $\mathrm{Pe}_p \gtrapprox 10^5$ [104]. The particulate Péclet number denotes the ratio of the characteristic time scale of particle diffusion with the characteristic time scale of the shear flow and is denoted by,

$$\mathrm{Pe}_p = \frac{6\pi\mu R^3\dot{\gamma}}{k_B T}. \tag{2.4}$$

Where μ denotes the dynamic viscosity of the suspending phase here considered to be blood plasma, R the characteristic size or radius of the particle, $\dot{\gamma}$ the shear rate magnitude and is further discussed in section 5.2, k_B the Boltzmann constant, and T the temperature.

In conclusion, the red blood cells show a wide range of challenging characteristics that form a complicated base for accurately modelling the flow of blood. However, the consideration of a membrane oxygenator as the flow domain already allows for a simplified approach. For instance, the aggregation of the blood cells into rouleaux, as discussed in section 2.3.1, is generally not observed due to the relatively high shear rates within the device. This consideration then also dictates that the effects of sedimentation are generally negligible compared to the advective forces, and the rheology becomes independent of clotting protein concentrations in the blood plasma, such as fibrinogen. Conversely, the elaborate single-particle dynamics at elevated shear rates, along with the non-uniform spatial distribution, appear of greater importance due to relatively small inter-fibre spacings in HFMOs.

2.4 The Essential Modelling Properties of Whole Blood

In this chapter, an overview was given of the composition and various characteristic properties of whole blood that are of interest in the modelling of its fluidic behaviour from a physical point-of-view. Not all of the characteristic properties of whole blood are of significant interest in the context of modelling its flow within a membrane oxygenator, and therefore, possible simplified considerations were deduced. In section 2.1, it was demonstrated that blood is generally considered a two-phase system consisting of a mixture of blood plasma and red blood cells. The RBCs were found to be non-colloidal deformable particles with a highly viscous interior fluid suspended in BP in section 2.2. These characteristics were shown in section 2.3 to be of importance in the flow response of the individual RBCs to the local fluid flow.
Furthermore, in section 2.3, the importance of the characteristic domain sizes found within HFMOs allow for the negligence of modelling the formation and behaviour of rouleaux but introduces the modelling requirement for the non-uniform distribution of RBCs. The disregard of the rouleaux decouples the overall rheology of blood flow from the complicated aggregation and de-aggregation mechanics and the concentrations of clotting proteins in BP. Lastly, it was additionally deduced that the complicated blood flow characteristics in HFMOs are not further influenced by sedimentation or thermal agitation, simplifying the overall rheology of blood flow further and decoupling it from thermal variations.

Chapter 3

The Governing Relations of Immiscible Two-Phase Flows

In section 2.1, it was demonstrated that whole blood could be considered to consist solely of red blood cells suspended in blood plasma, without particular interest of the other constituents, due to their abundance. The flow of such a particle suspension can effectively be modelled using two distinct approaches: an Eulerian-Lagrangian consideration and an Eulerian-Eulerian consideration [75]. In the Eulerian-Lagrangian approach, the suspending fluid is treated as a continuous phase, while the particles are represented as point masses and individually tracked. However, due to the computational expense of tracking a large number of particles, this method is not feasible for resolving the macroscopic flow behaviour of whole blood [11]. Conversely, the Eulerian-Eulerian approach considers both the fluid and the particles as continua, making it more suitable for macroscopic considerations. This chapter reviews the derivation of the single-phase governing relations to establish a solid foundation. Subsequently, a concise derivation of the two-phase governing relations is provided, elucidating the underlying assumptions in these models.

3.1 Single Phase Governing Relations

This section revisits the derivation of the general conservation law for single-phase flows before delving into more appropriate considerations for describing blood flow.
The conservation law can be derived by considering an arbitrarily shaped fluid element that may be moving and deforming by the surrounding fluid. A visual representation of such a fluid element is shown in figure 3.1, where $\Omega(t)$ denotes the time-dependent domain, $\partial\Omega(t)$ the time-dependent boundary of the element, $\boldsymbol{n}$ the outward unit normal vector of the boundary, and $\boldsymbol{u}$ the velocity at the boundary.

The general conservation law may now be derived by considering that the rate of change of an arbitrary scalar quantity per unit mass, ϕ, is dependent on the flux of that quantity across the boundary in combination with its production inside the element. The general conservation law in integral form for the arbitrary quantity can now be denoted by [48],

$$\underbrace{\frac{d}{dt}\int_{\Omega(t)} \rho\phi dV}_{\text{Rate of change}} = \underbrace{-\int_{\partial\Omega(t)} \boldsymbol{\mathcal{J}_\phi}\cdot\boldsymbol{n}dS}_{\text{Influx across boundary}} + \underbrace{\int_{\Omega(t)} \rho\mathcal{S}_\phi dV}_{\text{Volumetric source}}. \tag{3.1}$$

Where ρ denotes the mass density of the fluid, $\boldsymbol{\mathcal{J}_\phi}$ the boundary flux vector, and $\mathcal{S}_\phi$ the volumetric source term that describes the production in the element. The integral

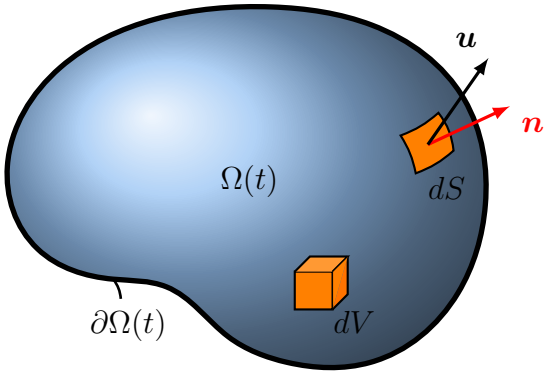

Figure 3.1: Single-phase arbitrary fluid element.

formulation may now be transformed from this Lagrangian point of view to an Eulerian by means of the Leibniz-Reynolds transport theorem [20]. The surface integral that describes the boundary flux can be expressed in terms of a volume integral using Gauss's divergence theorem [103], such that the differential formulation for the general conservation law may be denoted by [48],

$$\underbrace{\frac{\partial \rho\phi}{\partial t}}_{\text{Temporal}} + \underbrace{\nabla \cdot (\rho \boldsymbol{u}\phi)}_{\text{Advection}} = \underbrace{-\nabla \cdot \boldsymbol{\mathcal{J}}_{\boldsymbol{\phi}}}_{\text{Diffusion}} + \underbrace{\rho \mathcal{S}_{\phi}}_{\text{Source}}, \quad \forall \boldsymbol{x} \in \Omega(t), \partial\Omega(t). \tag{3.2}$$

The fundamental conservation laws can be expressed by substituting the conserved quantity, the boundary flux, and the source term with suitable considerations, along with the corresponding tensor products. These considerations are summarized in Table 3.1.

Conservation law	ϕ	$\boldsymbol{\mathcal{J}}_{\boldsymbol{\phi}}$	$\mathcal{S}_{\phi}$
Mass	1	0	0
Momentum	$\boldsymbol{u}$	$-\boldsymbol{\sigma}$	$\boldsymbol{g}$
Energy	E	$\boldsymbol{q} - \boldsymbol{\sigma} \cdot \boldsymbol{u}$	$\boldsymbol{g} \cdot \boldsymbol{u}$

Table 3.1: Fundamental single-phase conservation laws [48].

Where $\boldsymbol{g}$ denotes the gravitational acceleration vector, $\boldsymbol{q}$ the heat flux vector, and $\boldsymbol{\sigma}$ the Cauchy stress tensor.

3.2 Two-Phase Governing Relations

The general conservation law derived for single-phase flows can be extended to consider a mixture of two immiscible constituents, generally denoted two-phase flows. This section will provide an overview of this extended derivation and present the general governing relations for immiscible two-phase flows.

3.2.1 Local-Instant Formulation

A mixture of two immiscible phases is generally characterized by the presence of interfaces that separate the phases from each other [48]. These interfaces introduce discontinuous

changes in the phase properties, which necessitates the introduction of additional considerations in the derivation process. An arbitrarily shaped fluid element may again be employed to derive the general conservation laws for a mixture of two immiscible phases, now encompassing such an interface. Figure 3.2 visually depicts such an arbitrary fluid element, where the volumes and boundaries for the phases are sub-scripted with indices 1 and 2, respectively. Here, the interface is denoted by the subscript I and is assumed to be a purely geometric surface, primarily due to the consideration that the thickness of the interface is generally much smaller than its surface area. The boundary of the interface at time t can be represented by $\partial\Omega_I(t)$, and the curve enclosing this surface can be represented by $\mathcal{C}_I(t)$.

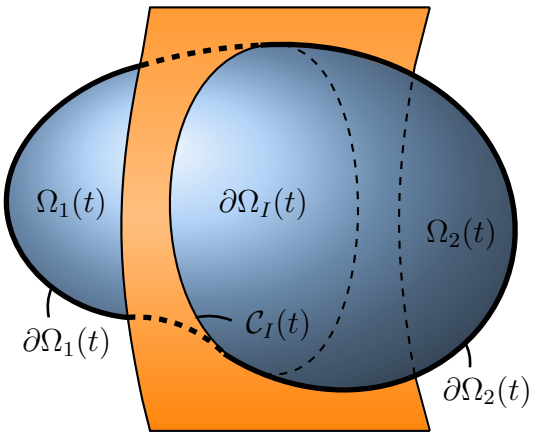

Figure 3.2: Two-phase arbitrary fluid element, inspired by [70].

The general conservation of an arbitrary quantity for the entire fluid element in integral form may then intuitively be denoted by,

$$\underbrace{\sum_k \frac{d}{dt}\int_{\Omega_k(t)} \rho_k\phi_k dV}_{\substack{\text{Rate of change}\\ \text{in both phases}}} + \underbrace{\frac{d}{dt}\int_{\partial\Omega_I(t)} \rho_I\phi_I dS}_{\substack{\text{Rate of change}\\ \text{in interface}}} = \underbrace{-\sum_k \int_{\partial\Omega_k(t)} \boldsymbol{\mathcal{J}}_{\boldsymbol{\phi_k}}\cdot\boldsymbol{n}_k dS}_{\substack{\text{Influx across both}\\ \text{phase boundaries}}}$$
$$\underbrace{-\oint_{\mathcal{C}(t)} \boldsymbol{\mathcal{J}}_{\boldsymbol{\phi_I}}\cdot\boldsymbol{n}_I d\mathcal{C}}_{\substack{\text{Influx across}\\ \text{interface boundary}}} + \underbrace{\sum_k \int_{\Omega_k(t)} \rho_k\mathcal{S}_{\phi_k} dV}_{\substack{\text{Volumetric source}\\ \text{in both phases}}} + \underbrace{\int_{\partial\Omega_I(t)} \rho_I\mathcal{S}_{\phi_I} dS}_{\substack{\text{Planar source}\\ \text{in interface}}} \quad \text{for } k=1,2. \tag{3.3}$$

Where the subscript k denotes the consideration of phases 1 and 2, and $\boldsymbol{n}_I$ the outward unit normal vector of the interface, which is generally directed tangential to the interface. It must now be noted that the conservation must hold for any volume, such that the independent contributions must hold. A general conservation law may be denoted for each phase and the interface separately [70]. These separate integral formulations may then be rewritten into differential formulations following the single-phase general conservation law derivation, as presented in section 3.1. The general local-instant conservation law for both phases is, in differential form, denoted by [48],

$$\underbrace{\frac{\partial\rho_k\phi_k}{\partial t}}_{\text{Temporal}} + \underbrace{\nabla\cdot(\rho_k\boldsymbol{u}_k\phi_k)}_{\text{Advection}} = \underbrace{-\nabla\cdot\boldsymbol{\mathcal{J}}_{\boldsymbol{\phi_k}}}_{\text{Diffusion}} + \underbrace{\rho_k\mathcal{S}_{\phi_k}}_{\text{Source}}, \quad \forall\boldsymbol{x}\in\Omega_k(t),\partial\Omega_k(t) \text{ for } k=1,2. \tag{3.4}$$

The local-instant conservation law for the interface is, in turn, denoted by [48],

$$\underbrace{\frac{\partial \rho_I \phi_I}{\partial t}}_{\text{Temporal}} + \underbrace{\nabla \cdot (\rho_I \boldsymbol{u}_I \phi_I)}_{\text{Advection}} = \underbrace{\sum_k (\rho_k \phi_k \boldsymbol{n}_k \cdot (\boldsymbol{u}_k - \boldsymbol{u}_I) + \boldsymbol{n}_k \cdot \boldsymbol{\mathcal{J}}_{\boldsymbol{\phi_k}})}_{\text{Phase fluxes}} + \underbrace{\mathcal{S}_\sigma}_{\substack{\text{Surface} \\ \text{flux}}} + \underbrace{\rho_I \mathcal{S}_{\phi_I}}_{\text{Source}}, \quad \forall \boldsymbol{x} \in \partial\Omega_I(t), \mathcal{C}_I(t). \tag{3.5}$$

Where the surface flux source term is introduced for interface curvature effects, which are generally dominated by the surface tension σ.
The fundamental conservation laws for these local-instant relations may, similarly to the single-phase relation, be retrieved by substitution of the considerations presented in table 3.1. It must be noted that the resulting conservation laws will hold only locally throughout the phase of consideration and not on or across the interface [48].

3.2.2 Time-Averaged Formulation

The local-instant relations derived in the preceding section offer a detailed description of the intricate dynamics of two-phase flows and enable the resolving of the numerous interfaces within the mixture [70]. However, solving for these detailed dynamics in practical engineering applications is often unnecessary and computationally too expensive. Instead, by utilizing appropriate averaging techniques, it becomes possible to capture the essential behaviour of the flow at a more reasonable computational cost [48].

3.2.2.1 Time Averaging

In the interest of a reduced computational cost, the technique of time averaging may be introduced, such that the two-phase flow can be treated as a mixture of continuous phases [48]. For this purpose, the flow variables and governing relations are averaged over a time interval that is sufficiently large to smooth out the complicating variations of the flow variables while also sufficiently small compared to the macroscopic time scale of the system. The time average of the arbitrary function $\mathcal{F}$ evaluated at arbitrary position $\boldsymbol{x}_0$ and time t_0, considered over a time interval $[\Delta t]$, is denoted by [48],

$$\overline{\mathcal{F}}_{k \vee I}(\boldsymbol{x}_0, t_0) \coloneqq \frac{1}{\Delta t} \int_{[\Delta t]} \mathcal{F}_{k \vee I}(\boldsymbol{x}_0, t) dt. \tag{3.6}$$

3.2.2.2 Phase Indicator Function

To keep track of which phases have passed the point $\boldsymbol{x}_0$ over the time interval $[\Delta t]$, a phase indicator function can be introduced. The function returns a value of unity when the appropriate phase or an interface is observed and zero otherwise [70],

$$\mathcal{X}_{k \vee I}(\boldsymbol{x}, t) \coloneqq \begin{cases} 1 & \text{if phase } k \text{ or the interface exists at position } (\boldsymbol{x}, t), \\ 0 & \text{otherwise.} \end{cases} \tag{3.7}$$

3.2.2.3 Local Void Fraction

An important variable may now be introduced by considering the time average of the phase indicator function, namely the local void fraction. The void fraction represents the

probability of observing a certain phase in $\boldsymbol{x}_0$ at t_0 and may be denoted by [48],

$$\alpha_{k\vee I}(\boldsymbol{x}_0, t_0) \coloneqq \frac{1}{\Delta t}\int_{[\Delta t]} \mathcal{X}_{k\vee I}(\boldsymbol{x}_0, t)dt. \tag{3.8}$$

3.2.2.4 Phase Averaging

The flow variables related to each phase can be categorized into quantities defined per unit volume of the phase or unit mass of the phase [70]. Quantities defined per unit volume are averaged most naturally using a phase average denoted by [48],

$$\overline{\overline{\mathcal{F}}}_k \coloneqq \frac{\overline{\mathcal{X}_k\mathcal{F}_k}}{\overline{\mathcal{X}}_k} \equiv \frac{\overline{\mathcal{F}}_k}{\alpha_k}. \tag{3.9}$$

3.2.2.5 Favre Averaging

The flow variables categorized per unit mass of the phase are most naturally averaged using mass, or Favre, averaging [48, 84],

$$\widetilde{\mathcal{F}}_k \coloneqq \frac{\overline{\rho_k\mathcal{F}_k}}{\overline{\rho}_k} \equiv \frac{\overline{\overline{\rho_k\mathcal{F}_k}}}{\overline{\overline{\rho}}_k}. \tag{3.10}$$

3.2.2.6 Reynolds Decomposition

The flow variables may be expressed as a combination of an averaged and a fluctuating component to express the local-instant formulations in terms of averages [48]. This consideration is sometimes denoted the Reynolds decomposition and is common practice in the derivation of Reynolds-Averaged Navier-Stokes (RANS) equations in turbulence modelling [12]. The decomposition for the volume-weighted density, mass-weighted arbitrary variable, and velocity may then be denoted by [48],

$$\rho_k = \overline{\overline{\rho}}_k + \rho_k', \quad \phi_k = \widetilde{\phi}_k + \phi_k', \quad \boldsymbol{u}_k = \widetilde{\boldsymbol{u}}_k + \boldsymbol{u}_k'. \tag{3.11}$$

Where the super-scripted $\prime$ denotes the consideration of a fluctuating component.

3.2.2.7 Two-Fluid Model

The two-fluid model may now finally be derived by considering the time average of the local-instant conservation law for the phases and is denoted by [48],

$$\begin{aligned}
&\underbrace{\frac{\partial \alpha_k\overline{\overline{\rho}}_k\widetilde{\phi}_k}{\partial t}}_{\text{Temporal}} + \underbrace{\nabla\cdot(\alpha_k\overline{\overline{\rho}}_k\widetilde{\phi}_k\widetilde{\boldsymbol{u}}_k)}_{\text{Advection}} = \underbrace{-\nabla\cdot\left(\alpha_k\overline{\overline{\boldsymbol{\mathcal{J}}}}_{\phi_k}\right)}_{\text{Diffusion}} + \underbrace{\alpha_k\overline{\overline{\rho}}_k\widetilde{\mathcal{S}}_{\phi_k}}_{\text{Source}} \\
&\underbrace{-\nabla\cdot\left(\alpha_k\boldsymbol{\mathcal{J}}^T_{\phi_k}\right)}_{\text{Turbulence}} + \underbrace{\mathcal{I}_{\phi_k}}_{\text{Interface}}, \quad \forall \boldsymbol{x} \in \Omega(t), \partial\Omega(t) \text{ for } k = 1, 2.
\end{aligned} \tag{3.12}$$

Where here $\Omega(t) = \Omega_1(t) + \Omega_2(t)$, $\partial\Omega(t) = \partial\Omega_1(t) + \partial\Omega_2(t) + \partial\Omega_I(t)$, and $\boldsymbol{\mathcal{J}}^T_{\phi_k}$ denotes the turbulent flux defined by,

$$\boldsymbol{\mathcal{J}}^T_{\phi_k} \coloneqq \overline{\overline{\rho_k\phi_k'\boldsymbol{u}_k'}}, \tag{3.13}$$

and $\mathcal{I}_{\phi_k}$ the interfacial transport source term for the phases. The time-averaged local-instant conservation law for the interface may, in turn, be denoted by [48],

$$\sum_k \mathcal{I}_{\phi_k} = \mathcal{I}_{\phi_m}. \tag{3.14}$$

Where $\mathcal{I}_{\phi_m}$ denotes the interfacial transport source term for the complete mixture, where $\mathcal{I}_{\phi_m} = \mathcal{I}_{\phi_m}(\mathcal{S}_\sigma)$.

3.2.3 Mixture Formulation

In the previous section, the two-fluid model was derived using well-established techniques in turbulent flow modelling, enabling a cost-effective description of the essential behaviour of two-phase flows. However, this model requires knowledge of the intricate interactions between the phases, which are often unknown and require extensive constitutive modelling techniques to accurately describe them, depending on the characteristics of the two-phase flow [31]. An alternative approach is to model the two-phase flow as a single mixture to alleviate the need for detailed phase dynamics. This approach reduces the amount of constitutive modelling required, making it particularly useful when precise knowledge of the dynamics of both phases is not necessary, or the phasic motions are sufficiently closely related.

3.2.3.1 Mixture Variables

The various variables found in the two-fluid model should be rewritten appropriately such that they may accurately represent a description of the mixture. The exact considerations are dependent on how the flow variables are averaged, where phase-averaged quantities may be denoted by [48],

$$\mathcal{F}_m \coloneqq \sum_k \alpha_k \overline{\overline{\mathcal{F}}}_k. \tag{3.15}$$

The mass averaged quantities may, in turn, be denoted by,

$$\mathcal{F}_m \coloneqq \frac{1}{\rho_m} \sum_k \alpha_k \overline{\overline{\rho}}_k \widetilde{\mathcal{F}}_k. \tag{3.16}$$

Where ρ_m denotes the mixture density. An intuitive interpretation of how the mixture variables are defined is given by considering the volume fractions of each phase for their local void fractions, e.g. $\alpha_k = \frac{\Omega_k(t)}{\Omega(t)}$. The mixture variables are then weighted simply by their volumetric presence in the arbitrary fluid element, depicted in figure 3.2, and will reduce to a single-phase consideration when only one phase is present.

3.2.3.2 Relative Phase Motion

The introduction of the mixture variables will simplify the final mixture formulation for the two-phase flows. However, it will lose the ability to describe some important characteristics of these flows. One of these important characteristics is the relative motion between the phases, which must be approximated using constitutive laws for the mixture formulation and will be discussed in chapters 4 and 6.
The relative motion of the phases can be described in various ways and mainly serves for more convenient closure model descriptions. The first and more obvious is the simple

consideration of a relative velocity, sometimes denoted the slip velocity, and is denoted by [48],

$$\boldsymbol{V}_r \coloneqq \widetilde{\boldsymbol{u}}_2 - \widetilde{\boldsymbol{u}}_1. \tag{3.17}$$

The second considers the relative velocity with respect to the centre of mass of the mixture and is denoted the phase diffusion velocity [48],

$$\boldsymbol{V}_{km} \coloneqq \widetilde{\boldsymbol{u}}_k - \boldsymbol{u}_m. \tag{3.18}$$

The last considers the relative velocity with respect to the centre of volume of the mixture and is denoted the phase drift velocity [48],

$$\boldsymbol{V}_{kj} \coloneqq \widetilde{\boldsymbol{u}}_k - \sum_k \alpha_k \widetilde{\boldsymbol{u}}_k. \tag{3.19}$$

3.2.3.3 Drift-Flux Model

The drift-flux model may be derived by summating the time-averaged general conservation laws from the two-fluid model for both phases [31], as was presented in equation 3.12. The various physical contributions can then be summated and replaced by the mixture quantities defined in equations 3.15 and 3.16. The resulting general conservation law for the mixture may then be denoted by [48],

$$\begin{aligned} &\underbrace{\frac{\partial \rho_m \phi_m}{\partial t}}_{\text{Temporal}} + \underbrace{\nabla \cdot (\rho_m \phi_m \boldsymbol{u}_m)}_{\text{Advection}} = \underbrace{-\nabla \cdot (\boldsymbol{\mathcal{J}}_{\phi_m})}_{\text{Diffusion}} + \underbrace{\rho_m \mathcal{S}_{\phi_m}}_{\text{Source}} \\ &\underbrace{-\nabla \cdot \left(\boldsymbol{\mathcal{J}}^D_{\phi_m}\right)}_{\text{Drift}} \underbrace{-\nabla \cdot \left(\boldsymbol{\mathcal{J}}^T_{\phi_m}\right)}_{\text{Turbulence}} + \underbrace{\mathcal{I}_{\phi_m}}_{\text{Interface}}, \quad \forall \boldsymbol{x} \in \Omega(t), \partial\Omega(t). \end{aligned} \tag{3.20}$$

Where $\boldsymbol{\mathcal{J}}^D_{\phi_m}$ denotes the macroscopic phase diffusion, or drift, flux introduced by the relative motion of the phases, and is defined by,

$$\boldsymbol{\mathcal{J}}^D_{\phi_m} \equiv \sum_k \boldsymbol{\mathcal{J}}^D_{\phi_k} \coloneqq \sum_k \alpha_k \overline{\overline{\rho}}_k \widetilde{\phi}_k \boldsymbol{V}_{km}. \tag{3.21}$$

The fundamental conservation laws for the mixture may now, similarly to all previous considerations, be retrieved by substitution of the considerations presented in table 3.1. However, to fully describe the behaviour of the mixture, an additional relation is required to describe the phase interactions. This full description can be accomplished by additionally considering the mass conservation of one of the two phases. The relation may be denoted the phase diffusion equation since it describes the macroscopic phase diffusion and is denoted for $k = 2$ by [48],

$$\underbrace{\frac{\partial \alpha_2 \overline{\overline{\rho}}_2}{\partial t}}_{\text{Temporal}} + \underbrace{\nabla \cdot (\alpha_2 \overline{\overline{\rho}}_2 \boldsymbol{u}_m)}_{\text{Advection}} = \underbrace{\alpha_2 \overline{\overline{\rho}}_2 \mathcal{S}_{1_2}}_{\text{Source}} \underbrace{-\nabla \cdot \left(\alpha_2 \overline{\overline{\rho}}_2 \boldsymbol{V}_{2m}\right)}_{\text{Drift}} + \underbrace{\mathcal{I}_{1_2}}_{\text{Interface}}, \quad \forall \boldsymbol{x} \in \Omega(t), \partial\Omega(t). \tag{3.22}$$

Where the phasic velocity is rewritten into a combination of the mixture velocity and the phase diffusion velocity using equation 3.18.

3.3 The Modelling of Two-Phase Flows

This chapter demonstrated the derivation for three types of governing relations of two-phase flows. The models at heart describe the same physics but differ in the degree of averaging of the flow variables, where the averaging generally served computationally cost-effectiveness at the cost of accuracy. The initial and un-averaged model is denoted the local-instant formulation, derived in section 3.2.1, and requires the modelling of either phase along with the separating interface. This model is the most expensive, as all governing relations are only valid in their respective phases. The technique of time-averaging was employed to derive the two-fluid model in section 3.2.2. The averaging alleviated the model expenses of the local-instant formulation and is similar to that of the derivation of the single-phase Reynolds-averaged Navier-Stokes equations. The time-averaging introduces the requirement of modelling the fluctuating components of the variable solutions, similar to the derivation of the RANS equations. The final model, derived in section 3.2.3, considers the two-phase flows in terms of a single mixture and is generally denoted the drift-flux model. This mixture consideration loses the ability to describe the detailed phase dynamics but generally requires less closure modelling.

Chapter 4

Constitutive Modeling of Momentum in Dispersed Two-Phase Flows

The two-phase flow models derived in the previous chapter generally do not obey the principle of determinism in their current form and require constitutive laws or models to get a complete description of the system. These constitutive models depend on the nature of the fluid mixture, such that there are no generally applicable models [31]. This chapter aims to introduce the primary classifications found in two-phase flows and utilize their characteristics to set the basis for modelling blood flow in hollow-fibre membrane oxygenators. Subsequently, a set of closure relations used to model the linear momentum evolution are presented that abide by the various considerations of blood flow discussed in the preceding chapters.

4.1 Two-Phase Flow Classifications

Two-phase flows can be classified into three primary categories based on the structure of the interfaces, each exhibiting distinct flow patterns. These categories are known as separated, dispersed, and mixed flows [70]. The distinct features of the primary categories, along with exemplar visual representations, are generally characterized as follows:

1. **Separated flows:** In separated flows, the two phases exist as independent fluidic regions with a limited number of interfaces [75]. Examples of separated flows include film, annular, jet, and stratified or stratified-wavy flows which is the separated flow-type illustrated in figure 4.1.

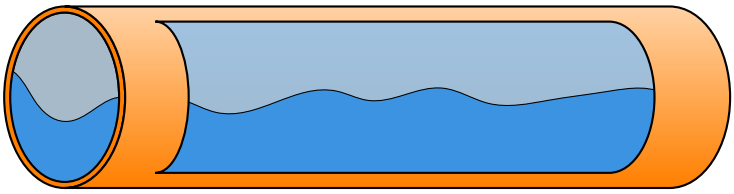

Figure 4.1: The illustrated phase separation of a stratified(-wavy) flow, inspired by [26].

2. **Dispersed flows:** Dispersed flows involve a mixture of a continuous primary phase laden with dispersed regions of a secondary phase. The dispersed phase can take

the form of bubbles, droplets, or solid particles, making this class most eligible to describe blood flow. The bubbly flow classification is illustrated in figure 4.2.

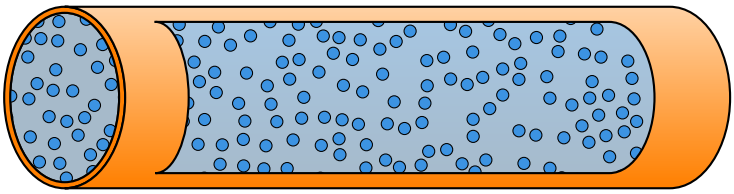

Figure 4.2: The illustrated phase separation of a bubbly flow, inspired by [48].

3. **Mixed flows:** Mixed flows, also known as transient flows, exhibit characteristics of both separated and dispersed flows. They often involve transitions between the two primary flow classes through, for example, the evaporation of a pure liquid transitioning into its vapour phase.

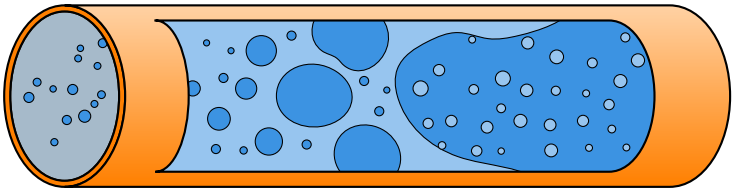

Figure 4.3: The illustrated phase separation of a mixed two-phase flows characterized by a phase transition, inspired by [100].

In conclusion, the particulate nature of blood aligns most closely with the characteristics of a dispersed flow within the generic two-phase flow classification framework discussed in this section.

4.2 Fluid Flow Classifications

Similarly to single-phase flows, dispersed two-phase flows can be classified based on the expected flow domain and regime. The well-known Reynolds number is a primary tool for distinguishing the flow regime, which can easily be derived by dimensional scaling of the single-phase Navier-Stokes equations. These equations are derived from Cauchy's equations, denoted in equation 3.2 under the consideration of linear momentum as denoted in table 3.1, where the fluid is assumed Newtonian. The Reynolds number denotes the ratio of the inertial forces with the viscous forces and is denoted by [20],

$$\mathrm{Re}_L \coloneqq \frac{\rho U L}{\mu} \equiv \frac{U L}{\nu}. \tag{4.1}$$

Where U denotes the characteristic flow velocity, L the characteristic domain size, and $\nu \coloneqq \frac{\mu}{\rho}$ the kinematic viscosity of the fluid. The Reynolds number is important as it allows the fluid flow to be characterized between laminar, transitional, and turbulent flow, essentially governing the importance of multiple contributions of the previously derived governing relations. In the limiting case of $\mathrm{Re}_L \to 0$, the flow can be considered a Stokes flow. This consideration allows the negligence of the momentum advection contribution, denoted by,

$$\nabla \cdot (\rho \boldsymbol{u} \otimes \boldsymbol{u}) \,. \tag{4.2}$$

Where the operator $\otimes$ denotes the outer or dyadic vector product [43]. The negligence of the advection simplifies the overall Navier-Stokes equations to a set of linear partial differential equations, usually denoted the Stokes equations. The Stokes equations can generally be used to describe blood flow within the body, i.e. *in vivo*, as here the Reynolds number is typically of order $\mathrm{Re}_L \approx 1 \times 10^{-3}$ [104]. This radical simplification does, however, not hold for blood flow within membrane oxygenators, i.e. *in vitro*, as here the Reynolds number is usually at least of order unity, e.g. $\mathrm{Re}_L \approx 3 - 5$ [101].

In conclusion, the flow of blood inside of an HFMO cannot be classified as a Stokesian flow. However, the generally low Reynolds number allows the consideration of a laminar flow, given that its value is much lower than the typically considered limit in pipe flow, denoted by $\mathrm{Re}_D \lessapprox 2300$ [20]. This consideration effectively permits the negligence of turbulent effects such that,

$$\boldsymbol{\mathcal{J}}^T_{\phi_{k\wedge m}} \to \mathbf{0}, \quad \forall \boldsymbol{x}, t. \tag{4.3}$$

4.3 Dispersed Phase Inertia

With the fundamental classifications of blood flow in a hollow-fibre membrane oxygenator now established, attention can be directed toward the motion of the dispersed phase with respect to the continuous phase. The fluid inertia at the scale of the dispersed phase is governed by the particulate Reynolds number, denoted by [104],

$$\mathrm{Re}_p \coloneqq \frac{\rho_c \dot{\gamma} a_d^2}{\mu_c}. \tag{4.4}$$

Where the sub-scripted c and d respectively denote the consideration of a continuous and dispersed phase variable, and a_d the characteristic size of the particle or dispersed phase. A low particulate Reynolds number characterizes a particle suspension as a Stokesian suspension, indicating negligible inertia at the length scales of the particle [69]. The characterization of a Stokesian suspension does, however, not dictate the entire flow is Stokesian, in contrast to the Reynolds number introduced in the previous section, as the motion at larger length scales may still be of an inertial nature [104]. This distinction then dictates that the suspended particles possess an inertial time scale that differs from the macroscopic inertial time scale. The Stokes number denotes the ratio of these time scales and is denoted by [69],

$$\mathrm{St} \coloneqq \frac{\tau_d}{\tau_c} \equiv \dot{\gamma} \tau_d. \tag{4.5}$$

Where τ_d denotes the inertial time scale at the length scale of the dispersed phase, sometimes denoted the relaxation time of a particle. The formulation of this time scale depends on the suspension flow regime [61], which can be assumed Stokesian when $\mathrm{Re}_p \lessapprox 1$ [69]. This consideration holds for blood flow inside an HFMO whenever $\dot{\gamma} \lessapprox 1 \times 10^5$, as follows from figure 4.4, and is assumed to hold in this study as generally $\dot{\gamma} \lessapprox 1 \times 10^4$ is experienced for non-aggregating blood in cardiovascular devices [104]. The inertial time scale for a Stokesian suspension of spherical particles is denoted by [61],

$$\tau_d \coloneqq \frac{2\rho_d a_d^2}{9\pi\mu_c}, \quad \mathrm{Re}_p \lessapprox 1. \tag{4.6}$$

The Stokes number at low particulate Reynolds is thus proportional to the particulate Reynolds number and generally an order of magnitude lower as follows from figure 4.4. The red blood cells can now be assumed to generally follow the motion of the suspending fluid, i.e. blood plasma.

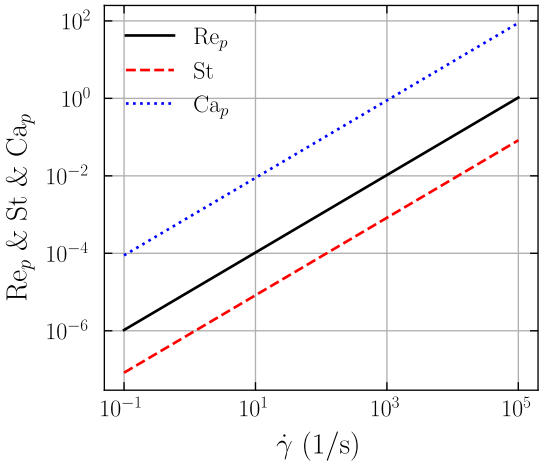

Figure 4.4: Particulate Reynolds, Stokes, and Capillary numbers as a function of shear rate, where following chapter 8, $\rho_c = \overline{\overline{\rho}}_c = 994\,\mathrm{kg/m^3}$, $\rho_d = \overline{\overline{\rho}}_d = 1110\,\mathrm{kg/m^3}$, $a_d = 3.6 \times 10^{-6}\,\mathrm{m}$, $\mu_c = \overline{\overline{\mu}}_c = 1.23 \times 10^{-3}\,\mathrm{Pa \cdot s}$, and $G = 5 \times 10^{-6}\,\mathrm{N/m}$ [60].

In conclusion, the characteristics of whole blood inside an HFMO generally align with the behaviour of a Stokesian suspension, as indicated by the typically low values of both $\mathrm{Re}_p \lessapprox 1$ and $\mathrm{St} \ll 1$. The consideration of a Stokesian suspension, along with the generally high volume fraction of red blood cells, ensures the modelling of blood can successfully be done using the computationally cost-effective mixture model formulation [61].

4.4 Phasic Stress Tensors

The drift-flux model now governs the linear momentum of whole blood, denoted in equation 3.20, following the considerations of the previous sections. The first contribution in the governing relation that must be modelled is the diffusive flux of linear momentum. In the two-phase system, this flux is governed by the Cauchy stress tensor of both phases and their phasic average for the mixture. The stress tensor is conventionally decomposed into an elastic and viscous contribution as follows [35],

$$\boldsymbol{\sigma} = \boldsymbol{\sigma}_0 + \boldsymbol{\tau}. \tag{4.7}$$

Where $\boldsymbol{\sigma}_0$ denotes the stress experienced by the fluid element at rest and $\boldsymbol{\tau}$ the viscous stress tensor, which is entirely dependent on the fluid motion.

4.4.1 Continuous Phase Stress Tensor

The continuous phase of blood consists of blood plasma, which may show a slight non-Newtonian viscoelastic response to fluid stresses [18, 90]. However, it is generally assumed to behave like a viscous, Newtonian, isotropic, fully fluid material [11]. The customary stress decomposition, presented in equation 4.7, may then be rewritten as [64],

$$\overline{\overline{\boldsymbol{\sigma}}}_c = -\overline{\overline{p}}_c \boldsymbol{\mathcal{I}} + \overline{\overline{\boldsymbol{\tau}}}_c = \left[-\overline{\overline{p}}_c + \overline{\overline{\lambda}}_c \,\mathrm{tr}(\boldsymbol{\mathcal{D}}_c)\right] \boldsymbol{\mathcal{I}} + 2\overline{\overline{\mu}}_c \boldsymbol{\mathcal{D}}_c \tag{4.8}$$

Where p denotes the hydrostatic pressure, μ the dynamic viscosity, λ the second coefficient of viscosity, which may by consideration of Stokes' hypothesis denoted as $\lambda = -\frac{2}{3}\mu$ [35], $tr(.)$ the trace norm, $\boldsymbol{\mathcal{I}}$ the identity matrix, and $\boldsymbol{\mathcal{D}}$ the strain-rate tensor. The strain-rate

tensor is given by the symmetric contribution of the Jacobian matrix of the velocity field and may be denoted by [12],

$$\boldsymbol{\mathcal{D}} \coloneqq \frac{1}{2}\left(\nabla \otimes \boldsymbol{u} + (\nabla \otimes \boldsymbol{u})^{+}\right). \tag{4.9}$$

Where $\nabla \otimes \boldsymbol{u}$ denotes the velocity gradient tensor, often more concisely but mathematically inconsistent, denoted by $\nabla \boldsymbol{u}$ [43], and $(.)^{+}$ the transpose operator.

4.4.2 Dispersed Phase Stress Tensor

The dispersed phase of blood is commonly assumed to consist solely of red blood cells, as was discussed in section 2.1. The non-idealistic shape, deformability, aggregability, and relatively high viscosity of the cytoplasm compared to that of the continuous phase necessitate the representation of an anisotropic, viscoelastic, non-Newtonian stress tensor that is dependent on the local void fraction, its gradient, the orientation, and the strain-rate of the red blood cells [64]. However, an appropriate stress tensor for this consideration will become quite complicated. A generalized model where the aggregability was not considered, initially derived to describe electro-rheological materials, already requires eleven contributions [64, 87],

$$\overline{\overline{\boldsymbol{\sigma}}}_d = \overline{\overline{\boldsymbol{\sigma}}}_d\left(\alpha_d, \nabla\alpha_d, \boldsymbol{n}_d, \mathcal{D}_d, \mathcal{D}_d^2\right). \tag{4.10}$$

In this model, the anisotropy is governed by assuming the particles may have some principal direction, $\boldsymbol{n}_d$, but resolving this anisotropy consideration in itself already requires an additional governing relation. It is therefore generally neglected [62, 64]. For simplicity, compound contributions are also neglected, such that the dispersed phase stress tensor is denoted by [65],

$$\overline{\overline{\boldsymbol{\sigma}}}_d = \left[C^{[0]}_{\overline{\overline{\boldsymbol{\sigma}}}_d} + C^{[1]}_{\overline{\overline{\boldsymbol{\sigma}}}_d}\nabla\alpha_d \cdot \nabla\alpha_d + C^{[2]}_{\overline{\overline{\boldsymbol{\sigma}}}_d}\operatorname{tr}(\boldsymbol{\mathcal{D}}_d)\right]\boldsymbol{\mathcal{I}} + C^{[3]}_{\overline{\overline{\boldsymbol{\sigma}}}_d}\boldsymbol{\mathcal{D}}_d + C^{[4]}_{\overline{\overline{\boldsymbol{\sigma}}}_d}\nabla\alpha_d \otimes \nabla\alpha_d + C^{[5]}_{\overline{\overline{\boldsymbol{\sigma}}}_d}\boldsymbol{\mathcal{D}}_d^2. \tag{4.11}$$

Where $C^{[0,\ldots,5]}_{\overline{\overline{\boldsymbol{\sigma}}}_d}$ denote flow and material properties of the dispersed phase. The first coefficient is generally given by the hydrostatic pressure of the dispersed phase, $C^{[0]}_{\overline{\overline{\boldsymbol{\sigma}}}_d} = -\overline{\overline{p}}_d$. The second and fifth coefficients, $C^{[1\wedge 4]}_{\overline{\overline{\boldsymbol{\sigma}}}_d}$, are related to the distribution of the dispersed phase and describe an additional normal stress contribution [87]. The normal stresses in blood are not well studied [64], such that the coefficients may be taken from measurements of granular materials [63], or given by complicated models derived through the kinetic theory of gasses [14]. In general, however, it is assumed that these normal stress effects are negligible such that $C^{[1\wedge 4]}_{\overline{\overline{\boldsymbol{\sigma}}}_d} = 0$ [53, 65]. The third coefficient corresponds to the second coefficient of viscosity of the dispersed phase, $C^{[2]}_{\overline{\overline{\boldsymbol{\sigma}}}_d} = \overline{\overline{\lambda}}_d$. The fourth coefficient is related to the dynamic viscosity of the dispersed phase. It takes into account the non-Newtonian, viscoelastic rheology of the phase by its dependence on the local dispersed phase volume fraction and the strain-rate tensor, which will be discussed in more detail in chapter 5. There are generally two ways this coefficient is described, by direct consideration of the dynamic viscosity, $C^{[3]}_{\overline{\overline{\boldsymbol{\sigma}}}_d} = 2\overline{\overline{\mu}}_d(\alpha_d, \boldsymbol{\mathcal{D}}_d)$ [48, 92], or additional local dispersed phase volume fraction dependence, $C^{[3]}_{\overline{\overline{\boldsymbol{\sigma}}}_d} = (1+\alpha_d)\overline{\overline{\mu}}_d(\alpha_d, \boldsymbol{\mathcal{D}}_d)$ [63, 64]. The sixth and last coefficient is similar to the cross-viscosity defined for the Reiner-Rivlin fluid model [64]. The cross-viscosity is for blood generally not defined, and consideration of this last contribution is usually neglected due to its higher order dependence on the strain-rate tensor such that,

$C^{[5]}_{\overline{\overline{\boldsymbol{\sigma}}}_d} = 0$. The most fundamental formulation for the dispersed phase stress tensor is then denoted by,

$$\overline{\overline{\boldsymbol{\sigma}}}_d = \left[-\overline{\overline{p}}_d + \overline{\overline{\lambda}}_d \operatorname{tr}(\boldsymbol{\mathcal{D}}_d)\right]\boldsymbol{\mathcal{I}} + 2\overline{\overline{\mu}}_d(\alpha_d, \boldsymbol{\mathcal{D}}_d)\boldsymbol{\mathcal{D}}_d. \tag{4.12}$$

Which resembles the customary stress tensor decomposition denoted in equation 4.7.

4.4.3 Mixture Stress Tensor

The mixture stress tensor can be derived by considering that the phasic diffusion fluxes, and therefore the phasic stress tensors, are phase-averaged quantities. The mixture stress tensor may thus, following equation 3.15, be denoted by,

$$\boldsymbol{\sigma}_m = \alpha_c \overline{\overline{\boldsymbol{\sigma}}}_c + \alpha_d \overline{\overline{\boldsymbol{\sigma}}}_d. \tag{4.13}$$

Where the stress tensors derived in the preceding sections may be substituted. However, this substitution will not immediately result in a complete consideration in terms of the mixture quantities as the strain-rate tensors are solely in terms of the phasic velocities. To this end, the phasic velocities may be substituted using the definition of the phase diffusion velocity, as denoted in equation 3.18 [48],

$$\boldsymbol{\sigma}_m = -p_m\boldsymbol{\mathcal{I}} + 2\mu_m(\alpha_d, \boldsymbol{\mathcal{D}}_d)\boldsymbol{\mathcal{D}}_m + \sum_{k=c,d} 2\alpha_k\overline{\overline{\mu}}_k\left[\boldsymbol{\mathcal{D}}_{km} - \frac{1}{3}\operatorname{tr}(\boldsymbol{\mathcal{D}}_k)\boldsymbol{\mathcal{I}}\right]. \tag{4.14}$$

Where p_m and μ_m are also phase averaged quantities, $\boldsymbol{\mathcal{D}}_m$ is defined using the mixture velocity and not an average of the phasic contributions, $\boldsymbol{\mathcal{D}}_{km}$ is defined using the phase diffusion velocity denoted in equation 3.18, and the two contributions of the last term are generally neglected. The strain-rate tensors in terms of the phase diffusion velocities can generally be assumed to approach zero when the particulate Reynolds number is small [106], i.e. $\mathrm{Re}_p \lessapprox 1$. Low particulate Reynolds number considerations were assumed to hold for blood flow in HFMOs, as discussed in section 4.3. The trace of the individual phasic strain-rate tensors generally also approaches zero, $\operatorname{tr}(\boldsymbol{\mathcal{D}}_k) \to 0$, under the assumption of both phases being incompressible, as was discussed in sections 2.1 and 2.2.

4.5 Interphasic Interactions

Three separate contributions govern the interphasic interactions in the drift-flux model. The first two are the macroscopic phase diffusion flux and interfacial momentum source defined for the mixture momentum equation, following equation 3.20. The third and last contribution is the consideration of the drift flux in the additional phasic mass conservation equation, denoted in equation 3.22, for which generally the dispersed phase is considered.

4.5.1 Macroscopic Phase Diffusion

The macroscopic phase diffusion for the mixture momentum is generally governed by the substitution of the phasic velocities into equation 3.21 and may be expanded using the phase diffusion velocity, as denoted in equation 3.18,

$$\boldsymbol{\mathcal{J}}^D_{\boldsymbol{u}_m} = \sum_k \alpha_k\overline{\overline{\rho}}_k\widetilde{\boldsymbol{u}}_k \otimes \boldsymbol{V}_{km} = \sum_k \left[\alpha_k\overline{\overline{\rho}}_k\boldsymbol{V}_{km} \otimes \boldsymbol{V}_{km} + \alpha_k\overline{\overline{\rho}}_k\boldsymbol{u}_m \otimes \boldsymbol{V}_{km}\right]. \tag{4.15}$$

Where the second contribution can be equated to zero using the following phase diffusion velocity identity [48],

$$\sum_k \alpha_k \overline{\overline{\rho}}_k \boldsymbol{V}_{km} = \boldsymbol{0}. \tag{4.16}$$

The resulting macroscopic phase diffusion flux is now proportional to the square of the phase diffusion velocity and may, in consideration of small particulate Reynolds, be neglected [106], i.e. $\mathrm{Re}_p \lessapprox 1$, such that,

$$\boldsymbol{\mathcal{J}}^D_{\boldsymbol{u}_m} \to \boldsymbol{0}, \quad \forall \boldsymbol{x}, t. \tag{4.17}$$

4.5.2 Interfacial Momentum Source

The interfacial transport source term, especially concerning interfacial momentum, is primarily influenced by surface tension, as discussed in section 3.2.2.7. The source term, in consideration of blood flow, aims to model the momentum absorption of the cell membrane to generate the intricate particle shapes discussed in sections 2.5 and 2.6. The significance of the surface tension on the fluid motion is generally quantified using the capillary number. The capillary number denotes the ratio of the viscous forces with the surface tension and is denoted by [20],

$$\mathrm{Ca} \coloneqq \frac{\mu_c U}{\sigma}. \tag{4.18}$$

Where a small capillary number denotes the surface tension governs the deformation of the suspended particles, generally when $\mathrm{Ca} \lessapprox 0.1$ [104], allowing the negligence of the deformability. Conversely, a large capillary number indicates that the particles are generally substantially deformed under the hydrodynamic stresses in the suspension. In such cases, the interphasic hydrodynamic interactions become of great importance due to the interface deformation. In the consideration of vesicles, such as red blood cells, the interface is characterized by a mechanical membrane rather than the generally considered interfacial layer. The mechanical membrane is generally not characterized by a surface tension, but rather an in-plane shear modulus [60]. To this end, should the capillary number be redefined using this shear modulus [104], which is denoted the particulate capillary number in this study for naming consistency,

$$\mathrm{Ca}_p \coloneqq \frac{\mu_c \dot{\gamma} a_d}{G}. \tag{4.19}$$

Where G denotes the in-plane shear modulus, and this capillary number definition is sometimes denoted the elastic capillary number [60]. Under physiological conditions the particulate capillary number is generally considered to be $\mathrm{Ca}_p \lessapprox 1$ [104], such that the contribution of the interfacial momentum source is generally not negligible. These elevated particulate capillary numbers are also visualized in figure 4.4 as a function of the shear rate. The figure shows that the capillary number may increase, considering blood flow in hollow-fibre membrane oxygenators. However, considering HFMOs, the generally considered range appears unreported, and the formulation of the interfacial momentum source in continuum modelling is typically omitted. Instead, the effect is typically considered through the heightened dissipation rate modelled using the rheology of the mixture. The rheology modelling is further discussed in chapter 5 and is also considered in this study to model the interfacial momentum source contribution.

4.5.3 Phase Diffusion Flux

In the context of the drift-flux model, the final modelling consideration pertains to the macroscopic phase diffusion flux within the mass conservation of the dispersed phase, typically governed by equation 3.22. This phase diffusion flux can be modelled either through its relation to the relative phase motion, as discussed in section 3.2.3.2, or by the closure of the entire flux.
The relative motion is often modelled through the slip relation, which generally depends on the exact flow regime and flow type, i.e. sub-classifications of dispersed flows, under consideration and is modelled through a complicated combination of analytical and empirical considerations [73]. A variety of generalized algebraic and differential analytical models are discussed in [13] and empirical models in [48]. Additionally, a force-based modelling approach can be taken to model the relative motion based on the closure relations required for the two-fluid model. As the derivation for closure models for the two-fluid model was considered out-of-scope, these considerations are further discussed in appendix D.1.
The direct modelling of the flux is generally considered in studies where the migration of the dispersed phase is dominant and will be considered in more detail in chapter 6. Considering that migration is of major interest in this study, the models discussed there will also be considered as closure models for the phase diffusion flux of the dispersed phase mass conservation in this study.

4.6 The Constitutive Modelling of Linear Momentum in Blood Flows

This chapter deduced the primary classifications of blood flow in hollow-fibre membrane oxygenators. Blood can be considered a two-phase dispersed system whose flow inside an HFMO generally abides that of a laminar Stokesian suspension. These classifications effectively show that the red blood cells will generally follow the flow of the blood plasma and may successfully be described using the mixture model formulation, discussed in section 3.2.3.
The derivation of the constitutive models of the various unclosed contributions of the mixture linear momentum equation proved a complicated task that required several additional assumptions. The derivation of the Cauchy stress tensor, applicable to the mixture, was discussed in section 4.4. The deformability of the RBCs and anisotropy due to the non-sphericity of the cells, along with higher-order strain-rate tensor considerations, were required to be neglected. These assumptions were required along with the exclusion of the cell aggregation, whose feasibility was evidenced in chapter 2. The resulting stress tensor applicable to the mixture followed the customary decomposition of stress tensors, shown in equation 4.7, and still requires the closure of a non-Newtonian dynamic viscosity. This dynamic viscosity definition should depend on the local volume fraction and strain-rate tensor of the dispersed phase, which follows directly from the considerations in section 4.4.2, and its derivation will be further discussed in chapter 5.
Furthermore, the interphasic interactions between the cells and the plasma required closure for various contributions. While the macroscopic phase diffusion flux for the mixture momentum could be considered negligible in the context of a Stokesian suspension, the closure of phase diffusion for the dispersed phase mass conservation equation remains an open question. This topic will be addressed in detail in chapter 6. Additionally, it is worth noting that the interfacial momentum source may not be easily dismissed, especially when considering particulate capillary numbers typically observed under physiological condi-

tions. However, this contribution appears commonly omitted in the continuum modelling of blood flow and considered through the non-Newtonian rheology modelling. Therefore, this contribution is also considered to be modelled through rheology in this study.

Chapter 5

The Rheology of Whole Blood

The rheological behaviour of whole blood is complicated and typically characterized by the presence and interactions of the suspended red blood cells [46]. The interesting dynamical response and interactions were already introduced in section 2.3, where it was shown that they consist of the deformability of the cells, hydrodynamic interactions for dense suspensions, and the aggregation of red blood cells. Additionally, it was shown in the preceding chapter, in section 4.4.2, that the consideration of the rheology is manifested in the description of the fluid stresses. The rheology depended solely on the local dynamic viscosity of the dispersed phase, under the negligence of many interesting interactions. The additional consideration of these interactions shows that whole blood exhibits four primary rheological features: shear-thinning, thixotropy, viscoelasticity, and viscoplasticity [3]. This chapter aims to introduce the essential rheological behavioural aspects of blood and how to model them. Firstly, the rheology of a simple arbitrary suspension is considered, followed by an in-depth consideration of shear-thinning and concluding with an overview of the remaining rheological features.

5.1 Rheology of Simple Particle Suspensions

First, a simple dilute suspension of small neutrally buoyant rigid spherical particles is considered to generate a better understanding of how and why the complicating behaviour of red blood cells is modelled using its rheology. Such a suspension allowed the treatment of isolated particles and was considered in the first theoretical work in the modelling of suspension rheology by Albert Einstein within the context of his doctoral dissertation [30]. The model directly considers the viscosity of the complete mixture and is generally denoted by,

$$\mu_m = \overline{\overline{\mu}}_c(1 + [\mu]\alpha_d). \tag{5.1}$$

Where $[\mu]$ denotes the intrinsic viscosity, which describes the non-dimensional proportionality of the particle viscosity due to geometry, deformability, and molecular weight [39], and is equal to $[\mu] = \frac{5}{2}$ for rigid spherical particles [104]. The model was derived using a single spherical particle in parallel flow [81], showing that the enhanced viscosity models the increase in viscous energy dissipation. This additional dissipation results from the flow deflection around the particle due to its deformation resistance [8, 104].

5.2 Shear-Thinning

Shear-thinning is a well-known and extensively studied rheological effect observed in the fluid flow of whole blood [11]. In general, shear-thinning is characterized by a decreas-

ing mixture viscosity for an increasing shear rate. The resulting mixture viscosity often exhibits limiting Newtonian behaviour on either side, generally denoted by μ_0 and μ_∞ respectively [8].
The shear-thinning behaviour of whole blood is influenced by different types of blood cell interactions at low and high shear rates. At low shear rates, it is primarily governed by the formation of rouleaux [11], as discussed in section 2.3.1. On the other hand, at high shear rates, the aggregates break up, and the deformability of blood cells becomes the dominant factor [104], as explained in section 2.3.2. The impact of both phenomena is visualized in figure 5.1, which illustrates the shear rate-dependent relative mixture viscosity. The shear rate is here generally expressed through the shear rate magnitude of the mixture using the double inner product of the mixture strain-rate tensor [92],

$$\dot{\gamma}_m \coloneqq \sqrt{2\boldsymbol{\mathcal{D}}_m : \boldsymbol{\mathcal{D}}_m}. \tag{5.2}$$

The consideration of a shear rate, in general, results in an isotropic modelling approach for the dispersed phase strain-rate tensor-dependent dynamic viscosity, discussed in section 4.4.2, i.e. $\mu_m = \mu_m(\alpha_d, \boldsymbol{\mathcal{D}}_d) \approx \mu_m(\alpha_d, \dot{\gamma}_m)$. Where additionally the Stokesian suspension consideration of section 4.3 allows the consideration of the mixture strain-rate tensor to be equivalent to that of the dispersed phase, $\boldsymbol{\mathcal{D}}_d \approx \boldsymbol{\mathcal{D}}_m$, $\mathrm{Re}_p \lessapprox 1$. The relative mixture viscosity is, in turn, denoted by the ratio of the mixture viscosity and the viscosity of the continuous fluid phase [95],

$$\mu_r \coloneqq \frac{\mu_m}{\overline{\overline{\mu}}_c}. \tag{5.3}$$

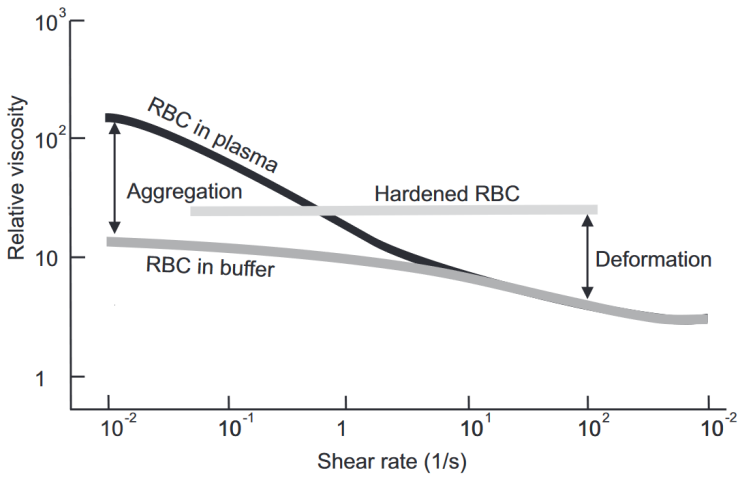

Figure 5.1: Shear-thinning rheology of whole blood at 45 vol% red blood cells for three types of treatment, adopted from [104].

In continuum-modelling of whole blood, numerical studies often consider this shear-thinning behaviour as the primary rheological effect of interest [92]. The modelling of the shear-thinning curve, with respect to the shear rate magnitude, is typically done by fitting an appropriate model to empirical data [113]. The choice of the model here depends on the region and included effects of interest. In a fundamental consideration of shear-thinning, the three models discussed in the following sections can be employed [8].

5.2.1 Cross Model

The Cross model can describe the complete curve as a function of the shear rate and is denoted by,

$$\mu_m(\dot{\gamma}_m) = \mu_\infty + \frac{\mu_0 - \mu_\infty}{1 + (k\dot{\gamma}_m)^m}. \tag{5.4}$$

Where k denotes the cross-model coefficient, and m the degree of shear-thinning.

5.2.2 Power-Law Model

The power-law model is generally most applicable in the transition region between the low and high shear rate behaviour and is denoted by,

$$\mu_m(\dot{\gamma}_m) = k\dot{\gamma}_m^{m-1}. \tag{5.5}$$

Where k denotes the consistency coefficient, and m the power-law index

5.2.3 Sisko Model

The third and last model is the Sisko model and is generally most applicable in the high shear rate region,

$$\mu_m(\dot{\gamma}_m) = k\dot{\gamma}_m^{m-1} + \mu_\infty. \tag{5.6}$$

Where k and m also denote the consistency coefficient and the power-law index.

In conclusion, the steady state shear-thinning is essential in the rheological modelling of whole blood and considers the decrease in apparent viscosity for an increasing shear rate. Considering the shear rate dependence, rather than the entire strain-rate tensor, limits the modelling consideration to an isotropic approach.

5.3 Extended Shear-Thinning Modelling

The simple models for shear-thinning, presented in the preceding section, are generally only applicable in simple dilute suspensions. Like the Einstein model presented in equation 5.1, such models will break down for non-uniform distributions and high concentrations of the dispersed phase [8]. A great variety of extended models have been proposed in the literature to resolve these limitations, and a review of a large amount of these models is available in [2, 113]. These models are generally extensions of the previously presented models and can roughly be categorized as Einstein-like, Carreau-type, and Casson-type models. The Casson-type models are typically extensions of the Sisko model, denoted in equation 5.6, and include viscoplasticity. For this reason, they are further discussed in appendix D.2.3.

5.3.1 Einstein-Like Models

The Einstein-like models are generally modelled after equation 5.1 and come in two flavours. The first considers a higher-order expansion in terms of the dispersed phase volume fraction and can be denoted by [104],

$$\mu_m(\alpha_d) = \overline{\overline{\mu}}_c(1 + [\mu]\alpha_d + k\alpha_d^2 + \dots). \tag{5.7}$$

Where k denotes a real-valued proportionality coefficient and a uniform dispersed phase volume fraction is typically assumed throughout the flow domain.

The second are more commonly employed and include well-known models such as the Quemada and Krieger-Dougherty type models [92]. These models replace the intrinsic viscosity consideration with that of a maximum allowable dispersed phase volume fraction reciprocal, e.g. a maximum packing density, and introduce a non-unity exponent,

$$\mu_m(\alpha_d) = \overline{\overline{\mu}}_c \left(1 - k\frac{\alpha_d}{\alpha_d^{\max}}\right)^{-m}. \tag{5.8}$$

Where k denotes a real-valued proportionality coefficient, which for the Krieger-Dougherty model is set to unity, $\alpha_d^{\max}$ the maximum packing density which for spherical particles is equal to $\frac{\sqrt{3}\pi}{8} \approx 0.68$, and m the non-unity exponent. The inclusion of additional effects, such as the non-uniformity of the dispersed phase volume fraction, is generally done by considering the volume fraction as variable. Either the proportionality coefficient or the exponent is taken as a function of shear rate and other essential variables such that $\mu_m = \mu_m(\alpha_d, \dot{\gamma}_m, \dots)$.

5.3.2 Carreau Type Models

The Carreau type models are generally an extension of the Cross model, see equation 5.4, and thus feature a good approximation to the complete curve. The generalized Carreau-Yasuda model is denoted by [113],

$$\mu_m(\alpha_d, \dot{\gamma}_m) = \mu_\infty + (\mu_0 - \mu_\infty)\left[1 + (k\dot{\gamma}_m)^p\right]^{\frac{m-1}{p}}. \tag{5.9}$$

Where k denotes a real-valued proportionality coefficient, and p and m real-valued exponents where the original Carreau model may be derived for $p = 2$. A modified Carreau-type model is the Yeleswarapu-Wu model, which was originally derived based on a model to include viscoelasticity in the modelling of whole blood [113]. While the model itself may also be utilized to describe the entire mixture, it is often used solely for the dispersed phase viscosity and is denoted by [92],

$$\mu_m(\alpha_c, \alpha_d, \dot{\gamma}_m) = \alpha_c\overline{\overline{\mu}}_c + \alpha_d\left(\mu_\infty + (\mu_0 - \mu_\infty)\frac{1 + \log(1 + k\dot{\gamma}_m)}{1 + k\dot{\gamma}_m}\right). \tag{5.10}$$

The inclusion of dependence on the local haematocrit value in Carreau-type models is generally done through polynomial modelling of the two limiting viscosities. Consider, e.g. [92], where the limiting viscosities for the Yeleswarapu-Wu model are modelled according to,

$$\begin{aligned} \mu_0(\alpha_d) &= a_1\alpha_d + a_2\alpha_d^2 + a_3\alpha_d^3, \\ \mu_\infty(\alpha_d) &= b_1\alpha_d + b_2\alpha_d^2 + b_3\alpha_d^3. \end{aligned} \tag{5.11}$$

Where a_n and b_n, $n \in [1, 2, 3]$, are real-valued proportionality coefficients to be derived using data fitting of empirically measured whole blood viscosities. Additional important physiological parameters such as fibrinogen concentration and temperature dependence can be included in the shear-thinning modelling of whole blood. Such models are further discussed in [2, 11, 113], but were exempt from modelling in the consideration of blood flow in this study as they were either out-of-scope or exempt from modelling following the conclusions of chapter 2.

5.4 Thixotropy

Thixotropy is another important rheological property displayed by whole blood, which complements its shear-thinning behaviour. It is considered the change of the mixture

viscosity with time rather than the shear rate [8]. The property is generally observed in the elevated-viscosity recovery when shear forces are removed from the mixture. The generic behaviour of a thixotropic fluid is illustrated in figure 5.2, where the viscosity of a shear-thinning fluid is compared to that of a shear-thinning thixotropic fluid over time for a sudden change in shear rates.

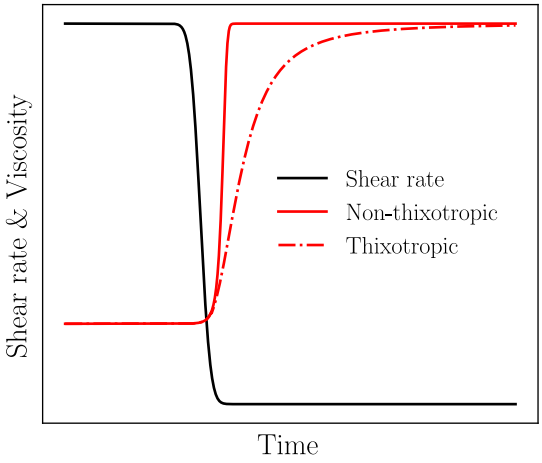

Figure 5.2: The illustrated time dependence of a thixotropic and non-thixotropic fluid for a sudden change in shear rate, inspired by [80].

The figure illustrates that the recovery of the limiting viscosity at zero shear for the thixotropic fluid takes a long time. In contrast, the viscosity recovery of a non-thixotropic fluid is nearly instant.
The observation of thixotropy in whole blood is then predominantly governed by the time-dependent phenomenon of rouleaux formation and breakdown in response to changing shear rates [3, 83], which was discussed in section 2.3.1. The blood cells simply require time to rearrange themselves into a new equilibrium configuration within the rouleaux after a change in shear rates. The observation and interest in this behaviour are more recent than that of shear-thinning and originate partially due to interest in pulsatile flow [46], and blood flow at low shear stresses [113]. The modelling of thixotropy was consequently considered out-of-scope for this study, and basic modelling considerations of the property are further discussed in appendix D.2.1.

In conclusion, the dependence of thixotropy on the observation of rouleaux within blood flow allows the exclusions of the modelling of the rheological property within the context of blood flow in a hollow-fibre membrane oxygenator. This exclusion of consideration follows directly from the assumption that rouleaux are generally not observed in HFMOs due to the typically small characteristic domain sizes and high shear rates in the flow of whole blood, as concluded in chapter 2.

5.5 Viscoelasticity

The viscoelastic behaviour of blood is closely related to its thixotropic character and is also a time-dependent phenomenon [11]. In general, viscoelasticity combines the viscous effects observed in fully fluid materials and elastic effects observed in solid materials [104]. An intuitive analogous example for understanding viscoelastic behaviour is a simple me-

chanical system consisting of a linear spring, and a viscous dash-pot [8]. For these system components, the stresses are respectively denoted by $\sigma_E^{VE} = \varepsilon E$, $\sigma_\mu^{VE} = \mu\dot{\gamma}$, where E denotes the elasticity modulus and ε the elastic strain. The response of the strain for a sudden and constant application of stress for a serial combination of a spring and a dash-pot, generally denoted the Maxwell model [8], is illustrated as a function of time in figure 5.3.

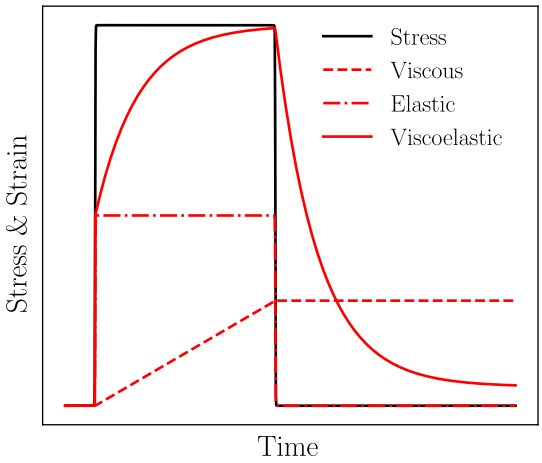

Figure 5.3: The illustrated time dependence of a Maxwell model viscoelastic strain and individual elastic and viscous strains for a step-function application of stress in time, inspired by [56].

The figure illustrates that, upon the instantaneous application of stress, the spring will be excited and the overall strain elevated to the permissible level. Conversely, the dash-pot takes time to reach an equilibrium state, causing a gradual increase in overall strain over time during loading. Upon stress unloading, the elastic contribution facilitates a rapid reduction in strain. However, complete strain recovery may not be achieved [56].
In blood, the effects of viscoplasticity are manifested in the deformation of the flexible red blood cells as they will regain their original discocyte shape after shear stresses are removed [11], along with the elastic response of the stretching of the bonds between the red blood cells in rouleaux [46]. Just like thixotropy, the observation of the viscoelasticity of blood is mainly of interest in pulsatile flow and regions of low shear [113]. The modelling of viscoelasticity was consequently considered out-of-scope for this study, and basic modelling considerations of the property are further discussed in appendix D.2.2.

In conclusion, the viscoelasticity can, similarly to the thixotropy discussed in the previous section, be exempt from modelling when considering blood flow within a hollow-fibre membrane oxygenator following the conclusions of chapter 2.

5.6 Viscoplasticity

The viscoplasticity of whole blood is characterized by its yield stress [11]. Fluids that include a yield stress are usually denoted as Bingham fluids [8] and are characterized by the requirement of an initial stress application before the fluid is allowed to flow. The resulting behaviour of a viscoplastic fluid is best envisioned by comparing the observed shear stresses over a range of shear rates, as illustrated in figure 5.4.

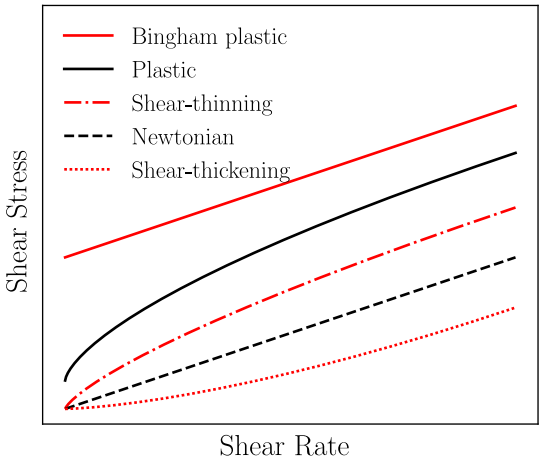

Figure 5.4: The illustrated shear rate dependence of various non-Newtonian fluids, inspired by [80].

The figure illustrates that viscoplastic fluids such as Bingham or regular plastics generally contain a minimum stress threshold. In contrast, fluids with a Newtonian, shear-thinning, or shear-thickening classification start at zero stress. The shear-thickening classification here denotes the opposite behaviour of shear-thinning discussed in section 5.2, i.e., the viscosity increases for an increasing shear rate.
The yield stresses of blood are manifested in the breakage of the bonds in the rouleaux structure [3]. These stresses are generally relatively small, typically considered in the order of $\sigma_y^{VP} = 1\,\text{mPa}$ [11]. The small magnitudes of these stresses also cause considerable uncertainty in its exact value as it is generally difficult to measure. The modelling of viscoplasticity was consequently considered out-of-scope for this study, and basic modelling considerations of the property are further discussed in appendix D.2.3.

In conclusion, the observation of viscoplasticity in whole blood depends primarily on the observation of rouleaux. The resulting typical yield stresses are additionally relatively small, such that the viscoelastic feature is allowed to be exempt from modelling in consideration of blood flow within a hollow-fibre membrane oxygenator following the conclusions of chapter 2.

5.7 The Rheological Modelling of Whole Blood

This chapter introduced the rheological modelling of whole blood with a particular interest in its shear-thinning characteristic. The shear-thinning generally shows a reduction in the apparent viscosity of whole blood for an increasing shear rate and is related to the breakage of red blood cell aggregates at low shear rates and deformation of red blood cells at high shear rates, as discussed in section 5.2. The shear-thinning characteristic also proved the most important in consideration of non-aggregating whole blood, as the other characteristics, i.e. thixotropy, viscoelasticity and viscoplasticity, are generally only important at low shear rates under the observation of rouleaux.
The modelling of shear-thinning can be realized in numerous ways, with some fundamental considerations introduced in sections 5.2 and 5.3. However, a universally agreed-upon modelling strategy is lacking [113]. Consequently, the selection of a viscosity model often seems to be driven more by individual preferences than by strict adherence to performance or accuracy-based criteria.

Chapter 6

Shear-Induced Migration Modelling of Red Blood Cells

The deformable red blood cells suspended in the blood plasma not only ensure an interesting rheological behaviour for whole blood, as evidenced in the previous chapter, but the particles also tend to migrate lateral relative to the dominant flow direction. This migratory behaviour is not specific to blood cells and may be observed in any particle suspension. The behaviour is especially pronounced in small domains, as was evidenced by the Fåhræus and Fåhræus–Lindqvist effects discussed in section 2.3.3, or for low, but finite, Reynolds flows discussed in section 4.2. The dominant mechanisms that induce these particle migrations and the modelling thereof are discussed in this chapter.

6.1 Mechanisms of Shear-Induced Migration

The initial observations of the lateral migration of particles in the work of Poiseuille [85], concerning the flow of whole blood, predate the observations of the Fåhræus and Fåhræus–Lindqvist effects [66]. In contrast to these findings, Bretherton [16] demonstrated that these observations are not possible for an isotropic, neutrally buoyant, rigid body in unidirectional Stokes flow of a Newtonian fluid due to the linearity and flow reversibility of the Stokes equations [37]. The first experimental evidence of lateral, neutrally buoyant particle migration in low-Reynolds flow in the work of Segré and Silberg [96] then demonstrates the importance of inertial effects on the observation of the migratory behaviour [102]. The mechanisms that were found to introduce this migratory behaviour are discussed in this section.

6.1.1 Solid Boundary Presence

The migratory behaviour of dense, neutrally buoyant particle suspensions was first observed in a Couette flow of a dense suspension of rigid spheres [36]. The suspended particles in the Couette flow were observed to migrate towards the central plane due to the influence of the solid boundaries [66].
The underlying mechanism responsible for this boundary presence-induced particle lift arises from an asymmetrical distribution of forces exerted by the suspending fluid on the surface of the particle, introduced by the solid boundary [40]. This mechanism is easily envisioned by considering a fluid flow where particles are suspended and moving alongside a solid boundary, as illustrated in figure 6.1. The solid boundary prevents a deflection of the flow around the particle, leading to the separation of streamlines at a point closer to the wall. This results in greater pressure on the side of the particle near the solid

boundary, forcing the particle away from the solid boundary [66].
The influence exerted by a solid boundary is not the exclusive factor responsible for the disruption of the force symmetry. The presence of neighbouring particles or a broken geometrical symmetry will additionally lead to the lateral migration of particles [37, 102]. The geometrical symmetry is generally broken through non-symmetrical shapes and deformability. Consequently, deformable non-idealistically shaped particles or rigid spherical particles in the proximity of a flexible boundary [9] can also be observed to migrate, even in Stokes flows [95].

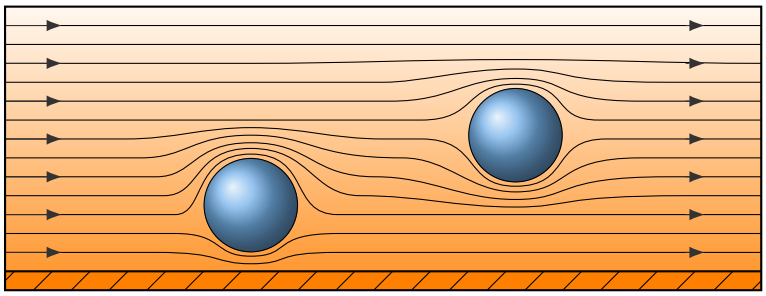

Figure 6.1: The illustrated wall-induced lift lateral migration mechanism for particles near a solid boundary, inspired by [102].

6.1.2 Velocity Profile Curvature

Another mechanism of lateral migration may arise when considering more complicated flow profiles than simple linear shear flows. This mechanism is induced by a curvature in the velocity profile, or a non-constant shear rate, and is extensively studied for Poiseuille flow profiles [25, 34, 52, 59].
Rigid spherical particles are typically observed to migrate away from the central line of the paraboloid velocity profile [102]. This movement opposes the boundary presence-induced lift discussed in the previous section, as illustrated in figure 6.2a. The underlying mechanism responsible for this velocity profile-induced particle lift is believed to originate from the asymmetry of the velocity acting on the surface of the particle. The velocity asymmetry results in a pressure asymmetry with a higher pressure acting on the side where the local flow velocity is higher [66].
On the contrary, the resulting migratory behaviour of deformable soft particles, like red blood cells or droplets, shows a far richer behaviour. Deformable particles can typically migrate in both directions and may even stop at intermediate positions [34]. The migratory behaviour depends on particle geometry, the dispersed and continuous phase viscosity ratio, and the capillary number. The capillary number describes the ratio between the viscous drag forces and the surface tension forces, as was previously introduced in chapter 4, and is denoted by,

$$\mathrm{Ca} \coloneqq \frac{\mu_c U}{\sigma}. \tag{4.18}$$

Specifically, for red blood cells, the elevated viscosity ratio is sufficient to reverse the direction of migration. Consequently, ensuring a migratory behaviour towards the central line of the velocity profile [34, 52], as illustrated in figure 6.2b.

In conclusion, the behaviour of particles in a suspension is complicated and easily influenced by many factors. Even a factor as simple as the mere presence of a solid boundary may introduce particle migration. The consideration of deformable non-spherical parti-

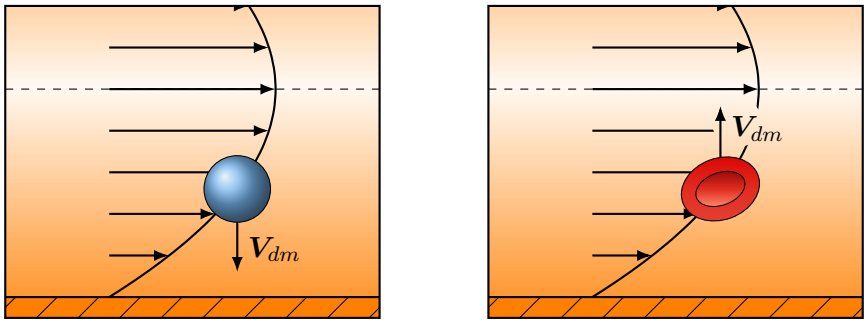

(a) Sphere (b) Red blood cell

Figure 6.2: The illustrated velocity profile-induced migratory behaviour of a rigid spherical particle and a red blood cell, inspired by [95].

cles, such as red blood cells, compliment the intricate flow response of the particles and may even reverse the direction of migration.

6.2 Shear-Induced Diffusion

The shear-induced migration is not the sole migratory effect for sufficiently dense suspensions of deformable particles in shear- or pressure-driven flow. The hydrodynamic interactions between the suspended particles also become of significance [37]. The frequent and repeated irreversible interactions of particles in the suspension result in a self-diffusive-like migratory behaviour normal to the plane of shear [114]. This phenomenon was first observed for a suspension of rigid spheres in the work of Leighton and Acrivos [58].
The underlying mechanism of shear-induced diffusion may best be understood by first considering a pair-collision of two particles moving in a simple pressure-driven flow on differing streamlines [104]. The interaction of these particles results in an oscillatory displacement within the flow centred around their original streamline. This displacement is characterized by a length proportional to the characteristic size of the particle and a frequency proportional to the local shear rate [58]. However, the oscillatory behaviour around the original streamline is only observed for perfectly smooth spherical particles and sometimes denoted a random walk. Particles with broken geometrical symmetry, through non-symmetrical shapes or deformability, will show an irreversible displacement towards neighbouring streamlines [37, 104], as is illustrated in figure 6.3.

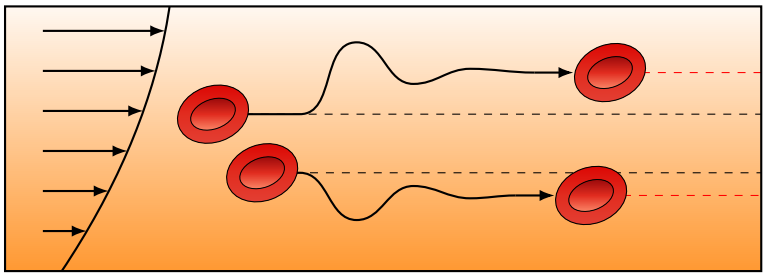

Figure 6.3: The illustrated pair-collision red blood cell trajectories resulting in irreversible streamline displacement in Poiseuille flow, inspired by [41].

In dense suspensions, the migratory mechanisms discussed in the preceding section lead to

the accumulation of particles near the central line of the velocity profile. This accumulation increases the observation of hydrodynamic interactions, such as inter-particle collisions, as illustrated in figure 6.4. Consequently, this results in a more pronounced diffusive flux in the opposite direction of the migration mechanisms [104]. The combined dependence of the characteristic particle size, local shear rate, and the local dispersed phase volume fraction are thus essential in the observation of shear-induced diffusion. This importance is evidenced by an effective diffusivity formulation, applicable to red blood cells, which may be denoted by [37],

$$\mathcal{D}_{\alpha_d}^{\mathrm{SID}} \equiv C_{\alpha_d}^{\mathrm{SID}} a_d^2 \dot{\gamma} \alpha_d. \tag{6.1}$$

Where $C_{\alpha_d}^{\mathrm{SID}}$ denotes a dimensionless diffusivity in the direction of the vorticity, and the product $\dot{\gamma}\alpha_d$ is generally denoted the frequency of pair interactions. The diffusivity effectively denotes that particles typically migrate away from the dense particle-laden core flow due to the increased probability of collisions. Additionally, the particles migrate away from regions of high shear rate as here collisions are typically more frequent [104].

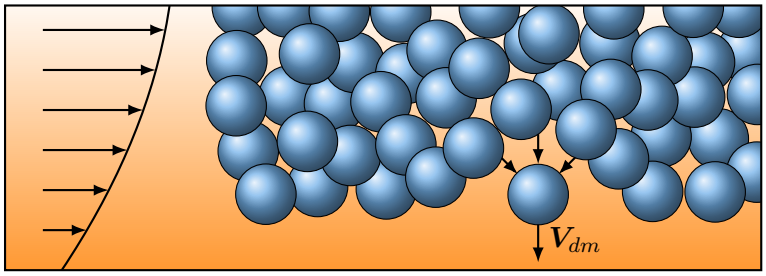

Figure 6.4: The illustrated particle dispersion due to hydrodynamic interactions in dense suspensions, inspired by [95].

In conclusion, the particle migration mechanism discussed in the preceding section induce a concentration of particles near the central line of the fluid flow. This concentration, in dense suspensions, allows for an increased observation of particle collisions that cause the particles to migrate away from the central line in a self-diffusive-like behaviour.

6.3 Shear-Induced Migration Modelling

The constitutive modelling of particle migration is generally done through the macroscopic phase diffusion for the mass conservation of the dispersed phase, denoted in equation 3.21, in the absence of other external forces. Two primarily considered model types exist to model the migration flux, the suspension balance and the diffusive flux models [104]. The derivation of both model types assumes a mixture momentum balance at steady state without additional source contributions. Drag forces solely govern the interphasic momentum exchange. Additionally, for the mixture momentum, the relative phase motion is neglected, such that the mixture momentum equation reduces to [106],

$$\mathbf{0} = \nabla \cdot (\boldsymbol{\sigma}_m). \tag{6.2}$$

In a two-phase formulation, denoted by equation 3.12, the migration modelling can alternatively be done by modelling individual lift-related forces. These formulations were considered out-of-scope in this study and are therefore further discussed in appendix D.3.

6.3.1 Suspension Balance Models

The suspension balance model was derived by Nott and Brady [77] and aims to relate the suspension rheology to the macroscopic phase diffusion flux. In this context, the phase diffusion flux of the dispersed phase mass conservation is considered and modelled through the dispersed phase stress tensor [78]. A variety of models exist based on this idea [106], but the most fundamental is that by Morris et al. [71]. Here, the diffusion flux is assumed linear in the divergence of the dispersed phase stress tensor and denoted as [71],

$$\boldsymbol{\mathcal{J}}^{D}_{1_d} = \overline{\overline{\rho}}_d \frac{2a_d^2}{9\overline{\overline{\mu}}_c} C^{\mathrm{SH}}_{\boldsymbol{\mathcal{J}}^{D}_{1_d}}(\alpha_d) \nabla \cdot \overline{\overline{\boldsymbol{\sigma}}}_d \tag{6.3}$$

Where $C^{\mathrm{SH}}_{\boldsymbol{\mathcal{J}}^{D}_{1_d}}$ denotes a sedimentation hindrance coefficient, dependent on the local dispersed phase volume fraction. The dispersed phase stress tensor here is not necessarily modelled as given in equation 4.12 and is generally the differing factor in various existing models. The dispersed phase stress tensor modelling here faces the same difficulties and variety of required assumptions discussed in section 4.4.2.
The consideration of the dispersed phase stress tensor ensures the freedom in the model as here an anisotropic stress tensor can be utilized, required in the observation of possible secondary flows induced by normal stress differences [88]. A significant and well-known limitation of the model is the possibility of it breaking down in regions of zero shear rate, observed in, e.g. the central line of Poiseuille flow, which is commonly resolved by including a small contribution to the shear rate [104].

6.3.2 Diffusive Flux Models

The diffusive flux model is a phenomenological model derived by Phillips et al. [82] based on the parameter scaling arguments derived by Leighton and Acrivos [58]. For the dispersed phase mass conservation, the macroscopic phase diffusion flux was assumed to consist of three contributions. The first is introduced by shear-induced diffusion due to particle collisions, as discussed in section 6.2. The second originates due to spatial variations in the mixture viscosity. The third and last originates due to Brownian motion and may generally be neglected for red blood cells, as evidenced in section 2.3.5. The application of this model appears extensively within the continuum modelling literature for whole blood, including work such as [22, 92, 111, 112]. The diffusion flux is generally denoted as [82],

$$\boldsymbol{\mathcal{J}}^{D}_{1_d} = -\overline{\overline{\rho}}_d C^{\mathrm{C}}_{\boldsymbol{\mathcal{J}}^{D}_{1_d}} a_d^2 \alpha_d \nabla(\alpha_d \dot{\gamma}_m) - \overline{\overline{\rho}}_d C^{\mu}_{\boldsymbol{\mathcal{J}}^{D}_{1_d}} a_d^2 \alpha_d^2 \frac{\dot{\gamma}_m}{\mu_m} \nabla \mu_m. \tag{6.4}$$

Where the Brownian motion contribution was omitted, and $C^{\mathrm{C}}_{\boldsymbol{\mathcal{J}}^{D}_{1_d}}$ and $C^{\mu}_{\boldsymbol{\mathcal{J}}^{D}_{1_d}}$ denote model coefficients of order unity. The usage of the shear rate magnitude instead of the full stress tensor, in contrast to the suspension balance models discussed in the preceding section, is a limiting factor to the accuracy of the model. This consideration essentially assumes an isotropic response, which is limiting in regions with high anisotropic behaviour such as stagnation points [92]. The model also suffers from the inability to describe zero shear rate regions in the flow properly. However, the model allows for a cost-effective and convenient initial modelling simplification, which surprisingly performs well, even at length scales comparable to that of a few red blood cells [22]. The model can, in some cases, in addition to the inclusion of Brownian motion, be extended to describe migration in curvilinear flows or sedimentation effects [111, 112].

6.4 Mathematical Model Equivalence

The shear-induced migration models discussed in the preceding section are seemingly vastly different but were shown to be mathematically relatable by means of a total derivative of an effective potential by Vollebregt et al. [106]. The migration models were shown to follow the subsequent generic framework under the assumption of an isotropic particle stress tensor,

$$\begin{aligned}\boldsymbol{\mathcal{J}}_{1_d}^{D} &= -C_{\boldsymbol{\mathcal{J}}_{1_d}^{D}}^{\mathrm{M}} \nabla \mu^{*} \\ &= -C_{\boldsymbol{\mathcal{J}}_{1_d}^{D}}^{\mathrm{M}} \left[\frac{\partial \mu^{*}}{\partial \alpha_d} \nabla \alpha_d + \frac{\partial \mu^{*}}{\partial \dot{\gamma}_m} \nabla \dot{\gamma}_m \right] \\ &= \mathcal{D}_{\alpha_d} \nabla \alpha_d + \mathcal{D}_{\dot{\gamma}_m} \nabla \dot{\gamma}_m .\end{aligned} \tag{6.5}$$

Where $C_{\boldsymbol{\mathcal{J}}_{1_d}^{D}}^{\mathrm{M}}$ denotes a mobility coefficient related to the dispersed phase volume fraction and the drag coefficient, $\mathcal{D}_{\alpha_d}$ and $\mathcal{D}_{\dot{\gamma}_m}$ effective diffusivities, and μ^{*} an excess chemical potential. The chemical potential is related to the particulate normal stresses, typically assumed to reduce to the particulate pressure [106]. This particulate pressure is similarly behaved to an osmotic pressure [104], which denotes the minimum pressure required to separate the particulate phase from the continuous phase using a permeable membrane [12]. This correlation indicates that the shear-induced migration of particles is linked to thermodynamics [106].

6.5 The Constitutive Modelling of Shear-Induced Migration of Red Blood Cells

This chapter introduced the various mechanisms of shear-induced migration and diffusion along with commonly considered modelling approaches. The migratory behaviour of particles generally shows a rich and complicating behaviour strongly related to the flow domain, flow regime and particle characteristics such as size, shape, and deformability. The primary mechanisms were discussed to be:

1. Migration due to the presence of solid boundaries, as discussed in section 6.1.1.
2. Migration due to velocity profile curvature, as discussed in section 6.1.2.
3. Self-diffusive-like migration due to particle interactions, such as inter-particle collisions, as discussed in section 6.2.

The modelling of these migration mechanisms is generally considered through two model types: the suspension balance and diffusive flux models. The suspension balance models generally aim to relate the migration to the rheological properties of whole blood by considering the migration flux as a function of the dispersed phase stress tensor. On the other hand, the diffusive flux models are phenomenological models based on scaling parameters related to the mechanisms.
Finally, it was discussed that in the consideration of an isotropic particle stress tensor, which is typically assumed, the suspension balance and diffusive flux models are equivalent. The assumption of isotropy then ensures that the migration model selection is driven by individual preference rather than strict accuracy or performance adherence.

Chapter 7

The Oxygenation of Blood in Hollow-Fibre Membrane Oxygenators

The oxygenation of whole blood in hollow-fibre membrane oxygenators consists of four stages. Firstly, the oxygen inside the fibres must diffuse through the porous membrane. The diffused oxygen is then dissolved in the blood plasma directly adjacent to the fibres and diffuses towards the red blood cells. The dissolved oxygen then needs to diffuse through the red blood cell membrane and the cytoplasm, and lastly, it is bound to the haemoglobin suspended in the cytoplasm. This chapter introduces the primary considerations of these four stages and models capable of describing the blood-side oxygen transfer and haemoglobin binding process.

7.1 Membrane-Side Oxygen Transfer

Hollow-fibre membrane oxygenators are designed to mimic the natural gas exchange process in the lungs. They function by allowing blood to flow through a container filled with thin, gas-permeable membranes [24]. Specifically, this type of oxygenator employs thin, hollow fibres typically made of hydrophobic micro-porous polypropylene or polymethylpentene. In long-term oxygenation applications, these fibres may also be coated with a thin layer of silicone [49, 93]. The fibres generally have an interior diameter of about $100 - 200\,\mu m$ [91], an exterior diameter of about $300 - 380\,\mu m$ [93], and require an inter-fibre spacing as low as $100\,\mu m$ for efficient oxygenation [24].
The basic micro-porous structure of the fibres, alongside an exterior bloodstream, is illustrated in figure 7.1. The illustration shows that the hydrophobic nature of the porous structure enables significant gas exchange, achieved by ensuring the pores remain saturated with air [110]. To this end, the oxygen concentration on the interior and exterior of the fibres becomes approximately equal [50].
In conclusion, the fibre dimensions and inter-fibre spacings are typically at least an order magnitude greater than the red blood cells. The RBCs are about $8\,\mu m$ in diameter, as discussed in section 2.2. The fibres provide a very efficient method of oxygen supply as the porous structure allows for the oxygen concentration on either side to be equivalent.

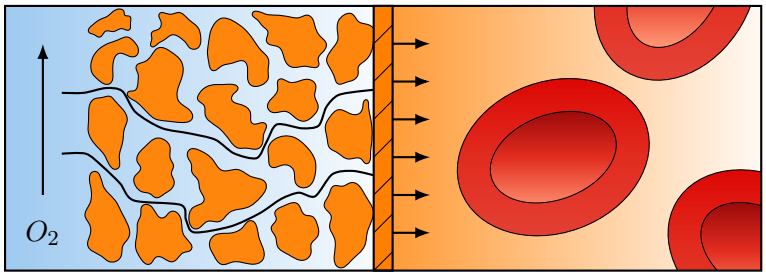

Figure 7.1: The illustrated membrane-side oxygen transfer, inspired by [94].

7.2 Blood-Side Oxygen Transfer

7.2.1 Continuous Phase Diffusion

The oxygen transfer through the continuous phase of whole blood, blood plasma, is generally governed by Fickian diffusion [97]. The diffusive flux is then governed by Fick's first law of binary diffusion, which is generally denoted by [12],

$$\boldsymbol{\mathcal{J}}_{\omega_a} = -\rho_t \mathcal{D}_{a,b} \nabla \omega_a. \tag{7.1}$$

Where ω_a denotes the mass fraction of species a, ρ_t the total mass density, and $\mathcal{D}_{a,b}$ the molecular diffusivity of species a in species b. The mass fraction itself is given by the ratio of the mass density of the species over the total mass density [12],

$$\omega_a \coloneqq \frac{\rho_a}{\rho_t} \equiv \rho_a \left(\sum_k \rho_k \right)^{-1}. \tag{7.2}$$

The mass density may also be related to the molar concentration [12],

$$c_a \equiv \frac{\rho_a}{M_a}. \tag{7.3}$$

Where M_a denotes the molecular mass of species a. The mass and molar concentrations of oxygen dissolved in blood plasma are generally rather low in magnitude and may, therefore, be related to the partial pressure of oxygen using the Henry-Dalton law [44],

$$p_a = \frac{c_a}{\beta_{a,b}}. \tag{7.4}$$

Where $\beta_{a,b}$ denotes the Bunsen solubility coefficient of a gaseous species a in a liquid species b. The coefficient quantifies the volume of a gas absorbed by a unit volume of liquid, or more accurately, solvent [15]. The complete transport of oxygen throughout the continuous phase is now governed by the commonly considered species continuity equations. In the consideration of constant material properties these are denoted by [12],

$$\frac{\partial \phi_a}{\partial t} + \boldsymbol{u} \cdot \nabla \phi_a = \mathcal{D}_{a,b} \nabla^2 \phi_a. \tag{7.5}$$

Where $\nabla^2(.) \coloneqq \nabla \cdot \nabla(.)$ denotes the Laplace operator, and ϕ can be replaced by ρ, c, or p depending on the coefficient of interest.

7.2.2 Interphasic and Dispersed Phase Diffusion

The cell membrane generally constrains the uptake of oxygen by red blood cells. However, this resistance is not primarily attributed to the membrane itself, which has been determined to be negligible [47]. Instead, the resistance is linked to the potential formation of a diffusion boundary layer around the membrane, creating a notable hindrance. This diffusion boundary layer may also manifest within the interior of the red blood cells. As a result, the cumulative oxygen resistance at the membrane contributes to a nearly uniform oxygen concentration field within the cell's interior [23].

7.2.3 Oxygen Equilibrium, Co-operativity, and Affinity

Haemoglobin is the protein dissolved in the cytoplasm inside the red blood cells and is responsible for the transportation of oxygen. The protein consists of four heme groups, each containing an iron atom to which the oxygen may bind reversibly to form oxyhaemoglobin [5]. The binding process is so-called co-operative, ensuring subsequent bindings become easier, resulting in differing reaction rates for each binding. These differing reaction rates are most comprehensively described using the four-step Adair reaction scheme. However, due to unfamiliarity with these rates, a common approach is to model them through a one-step approximation, which may be denoted by [23],

$$1 \text{ mol } O_2 + 1 \text{ mol } Hb \rightleftharpoons 1 \text{ mol } HbO_2. \tag{7.6}$$

Where Hb denotes an independently considered heme group of the haemoglobin and HbO_2 the oxyhaemoglobin. Moreover, the co-operative binding results in a non-linear relation between the amount of oxygen, generally represented by the partial pressure of oxygen, and the saturation of these heme groups [97]. The oxygen saturation here is denoted by [50],

$$S_{O_2}(p_{O_2}) \coloneqq \frac{c_{HbO_2}}{c_{Hb,t}} \equiv \frac{c_{HbO_2}}{c_{Hb,t} + c_{HbO_2}}. \tag{7.7}$$

Where $c_{Hb,t}$ denotes the total haemoglobin concentration, which is a constant. A simple but accurate and often considered model for oxygen saturation is the Hill equation denoted by [1],

$$S_{ODC}(p_{O_2}) = \frac{p_{O_2,m}^n}{p_{O_2}^n + p_{50}^n}. \tag{7.8}$$

Where the exponent n denotes the Hill constant, and p_{50} the partial pressure observed at 50% oxygenation. The saturation over the partial pressure is visualized in figure 7.2, which is generally a sigmoidal curve denoted the Hill plot or oxygen dissociation curve (ODC) [97].

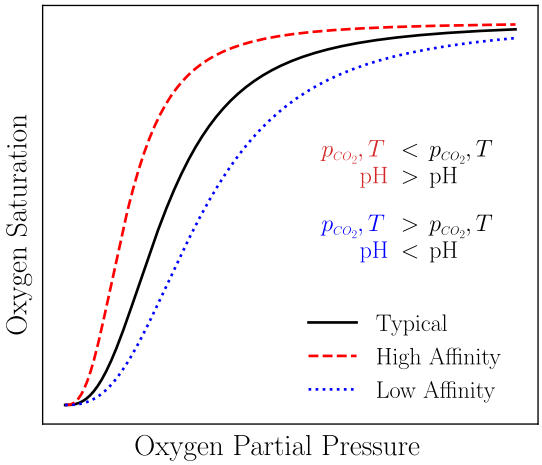

Figure 7.2: The illustrated oxygen saturation dependence of dissolved oxygen partial pressure for various degrees of oxygenation, modelled by means of the Hill equation, inspired by [94].

The figure illustrates that the oxygen uptake can differ significantly depending on the amount of dissolved oxygen present. Additionally, the effect of oxygen uptake affinity is illustrated. The affinity typically depends on factors such as carbon dioxide concentration, temperature, and pH of blood plasma, and concentrations of organic phosphates and proteins [5]. A more comprehensive model than the previously presented Hill model includes dependence on these factors and was proposed by Siggaard-Andersen et al. [99]. However, the dependence of the oxygen saturation on the affinity is typically neglected, and the Hill model coefficients are taken as constants.

In conclusion, the transport of oxygen through the blood plasma is similarly behaved to any generic gas dissolved in a liquid. The cell membrane may limit the oxygen uptake of the red blood cells through the formation of internal and external diffusion boundary layers. Consequently, the oxygen concentration throughout the cell is approximately uniform. The reversible bonding process of oxygen and haemoglobin is complicated. The binding rates typically depend on the amount of previously bound oxygen molecules. Consequently, the amount of bound oxygen present depends non-linearly on the available oxygen. Furthermore, these rates are influenced by the oxygen affinity, which depends on the local concentration of carbon dioxide, temperature, and blood pH. However, these considerations are typically neglected when modelling the saturation profile.

7.3 Oxygenation Modelling

The modelling of oxygenation in hollow-fibre membrane oxygenators is typically done using two models, the effective oxygen diffusivity model (EOD) and the micro-scale oxygenation model (MSM). The models were derived based on differing considerations and will be discussed in this section. Additionally, a newly derived model is discussed at the end of the section for which the detailed derivation is presented in appendix A.

7.3.1 Effective Oxygen Diffusivity Model

The effective oxygen diffusivity model is the most commonly considered and was originally derived by Weissman and Mockros [109]. The derivation considered the physical principle

of mass conservation of oxygen within whole blood at steady state, where the oxygen uptake of the red blood cells was modelled using an elevated advection. The resulting model effectively denoted a mixture consideration for oxygen transport throughout whole blood rather than explicitly modelling blood as a two-phase flow. The resulting steady-state advection-diffusion equation is generally denoted by [101],

$$\boldsymbol{u}_m \cdot \nabla c_{O_2,m} = \mathcal{D}_{\text{eff}}^{\text{EOD}} \nabla^2 c_{O_2,m}. \tag{7.9}$$

Where $\mathcal{D}_{\text{eff}}^{\text{EOD}}$ denotes the effective diffusivity coefficient. This coefficient is constructed using a constant continuous phase diffusivity and the reciprocal of the coefficient of elevated advection. The effective diffusivity is generally denoted by,

$$\mathcal{D}_{\text{eff}}^{\text{EOD}} \coloneqq \frac{\mathcal{D}_c}{1 + \dfrac{\alpha_d}{\beta_{O_2,m}} \dfrac{\partial S_{O_2}}{\partial p_{O_2}}}. \tag{7.10}$$

Where the derivative of the oxygen saturation with respect to the partial pressure aims to model the oxygen uptake of the red blood cells dynamically.
The model was derived under various simplifying assumptions, potentially limiting its accuracy under the consideration of non-uniform spatial distributions of red blood cells, all explained in more detail in [108]. The first is precisely the consideration of a uniform distribution of RBCs throughout the flow. Additionally, the RBCs are assumed to behave like reversible oxygen sinks or depositories that are advected in the flow. The fluid is considered a homogeneous mixture, and, lastly, the saturation derivative is modelled using the Hill model using the mixture oxygen partial pressure.

7.3.2 Micro-Scale Oxygenation Model

The micro-scale oxygenation model was recently derived by Kaesler et al. [50], under the consideration of a two-fluid model. The model consists of three governing relations, one for the continuous phase dissolved oxygen, the dispersed phase dissolved oxygen, and lastly, the dispersed phase bound oxygen. The model includes closure models for the interactions between the three considered oxygen species and was derived to improve an observed overestimation of saturation values by the effective oxygen diffusivity model discussed in the previous section. The governing relations under steady state are denoted,

$$\begin{aligned}
\nabla \cdot (\alpha_c \widetilde{\boldsymbol{u}}_c \widetilde{c}_{O_2,c}) &= \nabla \cdot (\alpha_c \mathcal{D}_{O_2,c} \nabla \widetilde{c}_{O_2,c}) - \mathcal{I}_{c_{O_2,c\to d}}, \\
\nabla \cdot (\alpha_d \widetilde{\boldsymbol{u}}_d \widetilde{c}_{O_2,d}) &= \nabla \cdot (\alpha_d \mathcal{D}_{O_2,d} \nabla \widetilde{c}_{O_2,d}) - \mathcal{S}_{c_{O_2\to HbO_2,d}} + \mathcal{I}_{c_{O_2,c\to d}}, \\
\nabla \cdot (\alpha_d \widetilde{\boldsymbol{u}}_d \widetilde{c}_{HbO_2,d}) &= \nabla \cdot (\alpha_d \mathcal{D}_{HbO_2,d} \nabla \widetilde{c}_{HbO_2,d}) + \mathcal{S}_{c_{O_2\to HbO_2,d}}.
\end{aligned} \tag{7.11}$$

Where $\mathcal{I}_{c_{O_2,c\to d}}$ denotes the diffusion of oxygen through the red blood cell membrane, and is denoted by,

$$\mathcal{I}_{c_{O_2,c\to d}} = \frac{A_d}{C_I^R \beta_{O_2,d}} (c_{O_2,c} - c_{O_2,d}). \tag{7.12}$$

Where A_d denotes the surface area of the red blood cell and C_I^R a measurement of the resistance to interphasic oxygen diffusion. The oxygen binding reaction sink term is denoted by,

$$\mathcal{S}_{c_{O_2\to HbO_2,d}} = C_{d,0}^R (S_{ODC} - S_{O_2})^3. \tag{7.13}$$

Where $C_{d,0}^R$ denotes the reference reaction rate determined by scaling the oxygen transfer rate to empirical observations, and the oxygen dissociation curve was modelled using the comprehensive model by Siggaard-Andersen et al. [99]. Here the partial pressure of the oxygen dissolved in the dispersed phase is considered as input for the ODC.

7.3.3 Conservation of the Total Mass of Oxygen Model

The last model was newly derived in this study, for which the detailed derivation is presented in appendix A. The model was, similarly to the effective diffusivity model, derived on the physical principle of mass conservation of oxygen within whole blood. The derivation did, however, not consider a steady state, but the conservation of the mass fraction of the total mass of oxygen governed by the drift-flux model derived in section 3.2.3. Additionally, the dispersed phase volume fraction was not assumed uniform. The resulting incompressible steady-state advection-diffusion equation in terms of the oxygen molar concentration is denoted by,

$$(1 + C_{HbO_2})\boldsymbol{u}_m \cdot \nabla c_{O_2,m} + C_{HbO_2}\boldsymbol{V}_{dm} \cdot \nabla c_{O_2,m} = \nabla \cdot (\mathcal{D}_{\text{eff}} \nabla c_{O_2,m}) \,. \tag{7.14}$$

Where C_{HbO_2} denotes an oxyhaemoglobin transport coefficient, and $\mathcal{D}_{\text{eff}}$ an effective diffusivity. These model coefficients, as introduced in equation A.28, are respectively denoted by,

$$\begin{aligned} C_{HbO_2} &\coloneqq \alpha_d \frac{c_{Hb,t}}{\beta_{O_2,m}} \frac{\partial S_{O_2}}{\partial p_{O_2,m}}, \\ \mathcal{D}_{\text{eff}} &\coloneqq \mathcal{D}_{O_2,c} + \mathcal{D}_{HbO_2,d} \frac{M_{HbO_2}}{M_{O_2}} C_{HbO_2}. \end{aligned} \tag{A.28}$$

7.4 The Modelling of Oxygen Transport in Whole Blood

This chapter introduced the basics of the four stages of oxygen transport through whole blood in hollow-fibre membrane oxygenators and commonly considered modelling approaches. Due to the permeable nature of the fibres, the membrane-side oxygen transfer is an efficient process. This permeable nature allows the oxygen concentration on either side of the fibre membrane to be assumed to be approximately equal. The oxygen transport through the continuous phase of whole blood is considered to be governed by the well-known Fickian diffusion. The interphasic diffusion is constrained by diffusion boundary layers external and internal to the cells. This constraint results in typically uniform oxygen concentration profiles throughout the interior of the red blood cells. Oxygen binding in the blood cells is complicated, including many influencing parameters. The co-operative process of the binding results in varying binding rates depending on how much oxygen is already bound in the blood cell.
Additionally, the solids suspended in blood plasma, the presence of carbon dioxide, temperature, and pH modify the oxygen affinity of the blood cells. The variable oxygen affinity results in the oxygen saturation, with respect to the partial pressure, dependent on these factors. Lastly, three models were described. The first is the typically considered effective oxygen diffusivity model, which describes the oxygenation process for blood as a mixture. The second is the recently derived micro-scale model, which considers blood flow from a two-phase perspective. The last is the conservation of the total mass of oxygen model derived in this study, which also considers a mixture description of the oxygenation process but was in contrast to the effective oxygen diffusivity model derived using the modelling consideration of chapter 3.

Chapter 8

Methodology

The preceding chapters discussed the physics underlying shear-induced particle migration and oxygenation. Alongside these physical considerations, various models were introduced to approximate the response of whole blood. This chapter discusses how these models were combined into a set of governing relations. It details how the dependent variables were constrained to reflect the physical behaviour of whole blood in hollow-fibre membrane oxygenators. The necessary considerations for numerical solution approximation are explored, along with defining the representative spatial domains relevant to the study of migration, oxygenation, and their combination. Finally, the chapter outlines the tools utilized for verifying and comparing the derived numerical solutions.

8.1 Governing Relations

The mathematical modelling of blood flow and its oxygenation, with its intricate features, is a complicated affair requiring a large set of closure models, as demonstrated in the preceding chapters. A large subset of possible closure models have been discussed, allowing for many model variations. The models utilized in this study, along with the underlying reasoning behind their selection, are discussed in this section.
Whole blood was considered a two-phase dispersed mixture following the considerations in chapter 2. The dispersed phase was assumed to consist solely of the red blood cells, while the continuous phase consisted of blood plasma. To this end, the axiom of continuity is denoted by,

$$\alpha_d + \alpha_c = 1. \tag{8.1}$$

Where α_d denotes the volume fraction of the dispersed phase, and thus identical to the volume fraction of the red blood cells, more commonly denoted the haematocrit. Furthermore, in chapter 4, it was deduced that generally, in hollow-fibre membrane oxygenators, whole blood can be considered as a Stokesian suspension. The red blood cells are then considered to follow the streamlines of the flow, and particle detachment is minimal. This consideration effectively allowed the modelling of the conserved quantities through the drift-flux model, which was derived in section 3.2.3. The influence of turbulence was neglected following the low-Reynolds considerations discussed in section 4.2. Lastly, it was additionally assumed that the flow of whole blood and oxygenation are invariant to thermal fluctuations following the considerations denoted in section 2.3.5, such that the consideration and rheological dependence of the thermal energy evolution could be neglected.

8.1.1 Blood Flow

The flow of whole blood is now governed by three types of conservation, the conservation of mass of the mixture, the conservation of linear momentum of the mixture, and the conservation of mass of either the dispersed or the continuous phase.

8.1.1.1 Conservation of Mixture Mass

The conservation of mass of the mixture reduced to a divergence-free, or solenoidal, velocity field restriction. This constraint was the result of three assumptions. Firstly, there is no mass transfer between the dispersed and continuous phases, effectively neglecting the cytoplasm loss of the red blood cells discussed in section 2.2. Secondly, there are no mixture mass sources or sinks, i.e. no creation nor destruction of whole blood. Lastly, the mixture and its constituents were assumed incompressible fluids following the considerations of section 2.1 and 2.2. The mixture mass conservation is now denoted by,

$$\nabla \cdot \boldsymbol{u}_m = 0. \tag{8.2}$$

8.1.1.2 Conservation of Mixture Momentum

The conservation of linear momentum of the mixture simplified greatly by considering the particulate Reynolds and Stokes numbers are generally low, as followed from section 4.3. This allowed the negligence of the macroscopic phase diffusion fluxes for the mixture momentum, as discussed in section 4.5.1. The body forces, such as gravity, were for simplicity in this study neglected and the interfacial mixture momentum source was assumed modelled through the rheological modelling as discussed in section 4.5.2. The momentum diffusion and rheology of whole blood were assumed to be governed by shear-thinning solely, following the considerations of section 4.4 and chapter 5, such that the mixture stress tensor reduced to,

$$\boldsymbol{\sigma}_m = -p_m \boldsymbol{\mathcal{I}} + 2\mu_m \left(\alpha_d, \dot{\gamma}_m\right) \boldsymbol{\mathcal{D}}_m. \tag{8.3}$$

Where the low particulate Reynolds number consideration, along with an isotropic momentum diffusivity assumption, allowed the consideration of the shear rate magnitude of the mixture, rather than that of the dispersed phase, i.e. $\mu_m \left(\alpha_d, \boldsymbol{\mathcal{D}}_d\right) \approx \mu_m \left(\alpha_d, \dot{\gamma}_m\right)$. The shear-thinning mixture viscosity was modelled in this study using the Yeleswarapu-Wu model, denoted in equation 5.10, and was chosen for its familiar phase-averaged definition. The dependence of the viscosity on the dispersed phase volume fraction was modelled following the considerations of Schenkel and Halliday [92] using the limiting viscosities, denoted in equation 5.11. The viscosity model parameters in turn are denoted in table 8.1, and the resulting relative viscosity for various dispersed phase volume fractions are illustrated with respect to the mixture shear rate magnitude in figure 8.1. The figure shows that the dispersed phase volume fraction dependence of the relative dynamic viscosity is most prominent in the range of low shear rates, but its variety is still non-negligible in the limit of $\mu_m \to \mu_\infty$.
The mixture momentum conservation equation may now be denoted by,

$$\frac{\partial \boldsymbol{u}_m}{\partial t} + \nabla \cdot \left(\boldsymbol{u}_m \otimes \boldsymbol{u}_m\right) = -\nabla p_m^k + \nabla \cdot \left(2\nu_m \left(\alpha_d, \dot{\gamma}_m\right) \boldsymbol{\mathcal{D}}_m\right). \tag{8.4}$$

Where $p_m^k \coloneqq \frac{p_m}{\rho_m}$ denotes the kinematic pressure, and $\nu_m \left(\alpha_d, \dot{\gamma}_m\right) \coloneqq \frac{1}{\rho_m} \mu_m \left(\alpha_d, \dot{\gamma}_m\right)$ the kinematic viscosity. The mixture density itself was taken constant using the phasic average

Parameter	Value	Dimension
$\overline{\overline{\mu}}_c$	1.23×10^{-3}	Pa · s
k	8.001	s
a_1	$-0.027\,79$	Pa · s
a_2	1.012	Pa · s
a_3	-0.636	Pa · s
b_1	0.0749	Pa · s
b_2	-0.1911	Pa · s
b_2	0.1624	Pa · s

Table 8.1: Viscosity model parameters, adopted from [92].

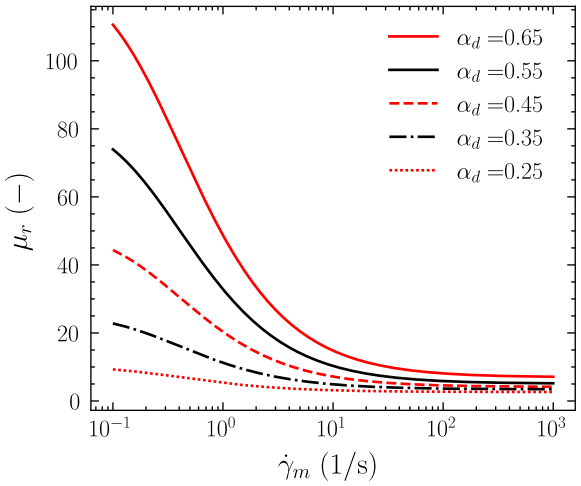

Figure 8.1: The relative viscosity dependence of the haematocrit and shear rate magnitude of the Yeleswarapu-Wu viscosity model, where the fitting coefficients are denoted in table 8.1.

of the densities using a reference haematocrit,

$$\rho_m = (1 - \alpha_{d,0})\,\overline{\overline{\rho}}_c + \alpha_{d,0}\overline{\overline{\rho}}_d. \tag{8.5}$$

Where the reference haematocrit is taken equal to the area-averaged value at the inlet, as denoted by equation 8.32, generally considered throughout this study to be equal to $\alpha_{d,0} = \langle \alpha_d\,(\boldsymbol{x}) \rangle_{\partial\Omega_{\text{inlet}}} = 0.45$, following the considerations of Secomb [95]. The phasic densities are in turn taken constant as the two phases were assumed incompressible, discussed in the previous section, and were taken equal to $\overline{\overline{\rho}}_c = 994\,\text{kg/m}^3$ and $\overline{\overline{\rho}}_d = 1110\,\text{kg/m}^3$ following the considerations of section 2.3.4. The mixture density considered in this study finally equates to $\rho_m = 1046.2\,\text{kg/m}^3$.

8.1.1.3 Conservation of Dispersed Phase Mass

The conservation of the phasic mass, where here the dispersed phase was considered, is governed by equation 3.22. The formulation simplified, similarly to the conservation of mixture mass, by neglecting inter-phasic mass transfer, the creation or destruction of mass, and finally assuming the dispersed phase is an incompressible fluid. The macroscopic phase diffusion flux was here modelled through the consideration of a diffusive flux model, as

denoted in equation 6.4, for its simplicity and common consideration in particle migration studies of whole blood. The dispersed phase mass conservation is now denoted by,

$$\begin{aligned}\frac{\partial \alpha_d}{\partial t} + \nabla \cdot (\alpha_d \boldsymbol{u}_m) &= -\nabla \cdot (\alpha_d \boldsymbol{V}_{dm}) \\ &= C^C_{\mathcal{J}^D_{1_d}} a_d^2 \nabla \cdot (\alpha_d \dot{\gamma}_m \nabla \alpha_d) + C^C_{\mathcal{J}^D_{1_d}} a_d^2 \nabla \cdot \left(\alpha_d^2 \nabla \dot{\gamma}_m\right) \\ &+ C^\mu_{\mathcal{J}^D_{1_d}} a_d^2 \nabla \cdot \left(\alpha_d^2 \frac{\dot{\gamma}_m}{\nu_m} \nabla \nu_m\right).\end{aligned} \tag{8.6}$$

Where no further formulation expansion was considered as the dispersed phase volume fraction field may not be continuous in space. Additionally, the kinematic viscosity was considered in the third contribution rather than the dynamic viscosity. Both considerations are equivalent as the mixture density was taken constant, as discussed in the preceding section, i.e. $\frac{1}{\nu_m}\nabla\nu_m \equiv \frac{1}{\mu_m}\nabla\mu_m$ if $\rho_m = \text{const}$. Lastly, a base value for the shear rate magnitude of $\dot{\gamma}_{m,0} = 0.5$ was considered to improve the stability of the diffusive flux model when $\nabla\dot{\gamma}_m \to \mathbf{0}, \dot{\gamma}_m \to 0$. The sole influence exerted by this consideration on the dispersed phase volume fraction results was a local decrease. The model parameters for the diffusive flux model are denoted in table 8.2, following the considerations of Chandran et al. [22].

Parameter	Value	Dimension
a_d	3.6×10^{-6}	m
$C^C_{\mathcal{J}^D_{1_d}}$	0.4	–
$C^\mu_{\mathcal{J}^D_{1_d}}$	0.6	–

Table 8.2: Migration model parameters, adopted from [22].

8.1.2 Oxygenation

The oxygenation of whole blood is governed by the conservation of the total mass of oxygen model described in section 7.3.3 and derived in appendix A. In this study, the formulation in terms of the partial pressure of oxygen was considered as it should slightly reduce the computational complexity of the numerical solver without loss of accuracy. The governing relation is now denoted by,

$$(1 + C_{HbO_2})\frac{D_m p_{O_2,m}}{Dt} + C_{HbO_2} \boldsymbol{V}_{dm} \cdot \nabla p_{O_2,m} = \nabla \cdot (\mathcal{D}_{\text{eff}} \nabla p_{O_2,m}). \tag{8.7}$$

Where the phase diffusion velocity, $\boldsymbol{V}_{dm}$, was left out of consideration in this study. In consideration of migration, these velocities were required to converge to zero, whereas, for non-migratory cases, the influence was assumed to be non-physical. The model coefficients are denoted by,

$$\begin{aligned} C_{HbO_2} &\coloneqq \alpha_d \frac{c_{Hb,t}}{\beta_{O_2,m}} \frac{\partial S_{O_2}}{\partial p_{O_2,m}}, \\ \mathcal{D}_{\text{eff}} &\coloneqq \mathcal{D}_{O_2,c} + \mathcal{D}_{HbO_2,d} \frac{M_{HbO_2}}{M_{O_2}} C_{HbO_2}. \end{aligned} \tag{A.28}$$

Where the Hill equation, as denoted in equation 7.8, was used to describe the oxygen saturation of whole blood and its derivative with respect to the partial pressure is denoted by,

$$\frac{\partial S_{O_2}}{\partial p_{O_2,m}} = \frac{n p_{50} p^n_{O_2,m}}{(p^n_{50} + p^n_{O_2,m})^2}. \tag{8.8}$$

The required oxygenation and saturation model parameters are denoted in table 8.3.

Parameter	Value	Dimension	Source
$c_{Hb,t}$	7.457	$\mathrm{mol/m^3}$	[50]
$\beta_{O_2,m}$	1.56×10^{-3}	$\mathrm{mol/(mmHg \cdot m^3)}$	[50]
$\mathcal{D}_{O_2,c}$	9.5×10^{-10}	$\mathrm{m^2/s}$	[1]
$\mathcal{D}_{HbO_2} \approx \mathcal{D}_{Hb}$	1.44×10^{-11}	$\mathrm{m^2/s}$	[1]
M_{O_2}	32	g/mol	[74]
$M_{HbO_2} \approx M_{Hb}$	6.7×10^4	g/mol	[23]
p_{50}	26.4	mmHg	[23]
n	2.65	–	[23]

Table 8.3: Oxygenation and saturation model parameters.

8.2 Boundary Conditions

In this study, typically, three types of boundaries were considered. The inlet, outlet, and wall. Physically, these correspond to the surfaces where whole blood enters, exits, and encounters a barrier, such as the fibres in hollow-fibre membrane oxygenators. Mathematically, these regions define the boundary conditions for the governing relations discussed in the preceding section. These conditions act as constraints on the solution variables, ensuring they reflect the physical conditions of the system. Moreover, these boundary conditions play a crucial role in formulating a well-posed problem, allowing for a unique solution to the differential equations and a stable algorithm. The boundary conditions considered in this study are discussed in this section.

8.2.1 Mixture Mass and Momentum Conservation

The mixture mass and momentum conservation require boundary conditions for the kinematic pressure and mixture velocity fields. These conditions remained equivalent to the generic boundary conditions employed in the consideration of Newtonian flow. The inlet conditions then generally denoted a Dirichlet boundary condition for the velocity field and a Neumann boundary condition for the pressure field, as denoted by,

$$\boldsymbol{u}_m = \boldsymbol{u}_m(\boldsymbol{x}), \nabla_{\boldsymbol{n}} p_m^k = 0, \quad \forall \boldsymbol{x} \in \partial\Omega_{\text{inlet}}. \tag{8.9}$$

Where $\nabla_{\boldsymbol{n}}(.) \coloneqq \nabla(.) \cdot \boldsymbol{n}$ denotes the boundary normal gradient. The velocity boundary condition was observed to cause solver divergence when a non-physical solution was employed in combination with the non-Newtonian viscosity model. To this end the analytical solutions for the Newtonian counterparts were utilized, such as the well-known (Hagen-) Poiseuille velocity field. The conditions imposed on the outlet were identical to the Newtonian counterpart and are denoted by,

$$\nabla_{\boldsymbol{n}} \otimes \boldsymbol{u}_m = \boldsymbol{0}, p_m^k = 0, \quad \forall \boldsymbol{x} \in \partial\Omega_{\text{outlet}}. \tag{8.10}$$

Where the Dirichlet boundary condition for the kinematic pressure ensures the uniqueness of the solution. The no-slip boundary condition was applied on the solid boundaries of the domain, which is denoted by,

$$\boldsymbol{u}_m = \boldsymbol{0}, \nabla_{\boldsymbol{n}} p_m^k = 0, \quad \forall \boldsymbol{x} \in \partial\Omega_{\text{wall}}. \tag{8.11}$$

8.2.2 Phasic Mass Conservation

The boundary conditions imposed on the inlet and outlet for the dispersed phase volume fraction were equivalent to the conditions imposed on the velocity field, and are respectively denoted by,

$$\alpha_d = \alpha_d(\boldsymbol{x}), \quad \forall \boldsymbol{x} \in \partial\Omega_{\text{inlet}}, \tag{8.12}$$

$$\nabla_{\boldsymbol{n}} \alpha_d = 0, \quad \forall \boldsymbol{x} \in \partial\Omega_{\text{outlet}}. \tag{8.13}$$

Where $\alpha_d(\boldsymbol{x}) = \langle \alpha_d \rangle_{\partial\Omega_{\text{inlet}}} = 0.45$ was considered following the considerations of Secomb [95]. Here the application of a uniform inlet profile, in contrast to the velocity, did not show any divergence problems. The boundary conditions at the solid boundaries, however, were not as straightforward. The migration flux, given for the diffusive flux model in equation 6.4, normal to the boundary was required to be zero [82],

$$\left(\boldsymbol{\mathcal{J}}^D_{1_d} \cdot \boldsymbol{n}\right)\big|_{\partial\Omega_{\text{wall}}} = \left(\alpha_d \boldsymbol{V}_{dm} \cdot \boldsymbol{n}\right)\big|_{\partial\Omega_{\text{wall}}} = 0 \tag{8.14}$$

This type of boundary condition is sometimes denoted the no-penetration boundary [72]. A variety of methods are proposed in the literature, ranging from simplified relations for the gradient of the dispersed phase volume fraction normal to the wall [22] to the consideration of a simple slip boundary condition [72]. These methods did however not show the required conservative behaviour in the analyses performed here, and therefore a condition was defined based on the normal flux directly. The normal flux was rewritten in terms of the normal gradient of the dispersed phase volume fraction. This allowed a gradual application over a number of fixed-point iteration steps every time step. The iterative application initiated with a zero gradient, and greatly improved the stability of the solver. A direct application would generally result in solver divergence due to the strong coupling between the momentum and phasic mass conservation equations. The applied normal gradient is denoted by,

$$\left(\nabla_{\boldsymbol{n}} \alpha_d\right) = -\left(\frac{\alpha_d}{\dot{\gamma}} \nabla_{\boldsymbol{n}} \dot{\gamma} + \frac{C^{\mu}_{\boldsymbol{\mathcal{J}}^D_{1_d}}}{C^{C}_{\boldsymbol{\mathcal{J}}^D_{1_d}}} \frac{\alpha_d}{\nu_m} \nabla_{\boldsymbol{n}} \nu_m \right), \quad \alpha_d \neq 0, \quad \forall \boldsymbol{x} \in \partial\Omega_{\text{wall}}. \tag{8.15}$$

Which essentially required the dispersed phase diffusion velocity normal to the boundary, $\boldsymbol{V}_{dm} \cdot \boldsymbol{n}$, to approach zero under the assumption that $\alpha_d \neq 0$. The intuition for this boundary condition may further be expanded by considering the definition of the dispersed phase diffusion velocity, denoted in equation 3.18, along with the no-slip condition imposed for the velocity field. The combination of these considerations result in the requirement of a zero dispersed phase velocity normal to the wall, elucidating the accuracy of the no-penetration name for the boundary condition. The implementation of the boundary condition within the OpenFOAM framework is presented in appendix C.2.2.

8.2.3 Oxygen Mass Conservation

The boundary conditions for the partial pressure of oxygen at the inlet and outlet were also equivalent to those considered for the velocity field. The imposed conditions are denoted by,

$$p_{O_2} = p_{O_2}(\boldsymbol{x}), \quad \forall \boldsymbol{x} \in \partial\Omega_{\text{inlet}}, \tag{8.16}$$

$$\nabla_{\boldsymbol{n}} p_{O_2} = 0, \quad \forall \boldsymbol{x} \in \partial\Omega_{\text{outlet}}. \tag{8.17}$$

Where $p_{O_2}(\boldsymbol{x}) = \langle p_{O_2} \rangle_{\partial\Omega_{\text{inlet}}} = 0$ was considered to solely consider an inflow of oxygen through the solid boundaries. At the solid boundaries a Dirichlet boundary condition

was considered for the partial pressure of oxygen following the considerations of section 7.1. The boundary condition is similarly to the inlet condition denoted by,

$$p_{O_2} = p_{O_2}(\boldsymbol{x}), \quad \forall \boldsymbol{x} \in \partial\Omega_{\text{wall}}, \tag{8.18}$$

Where now $p_{O_2}(\boldsymbol{x}) = \langle p_{O_2} \rangle_{\partial\Omega_{\text{wall}}} = 688$ was considered following the considerations of Hormes [44].

8.3 Solver Characteristics

8.3.1 Solution Algorithm

The solutions to the governing equations for fluid flow and oxygenation were approximated using an altered implementation of the PIMPLE algorithm within the open-source OpenFOAM framework. The nonlinearity in OpenFOAM solvers is resolved by linearization with respect to the previously obtained solutions. This linearization type generally does not result in an extensive compromise of accuracy for Newtonian fluid flow [38]. However, the strong non-linear coupling between the phasic mass conservation and mixture momentum conservation typically required a large number of outer loop fixed-point iterations or tiny time steps. These requirements originated from the problematic convergence of the phasic mass conservation along with the sensitivity of the mixture mass conservation constraint to large fluctuations in the viscosity. An additional stability and numerical cost improvement was retrieved by resolving the mixture momentum and mass conservation at a larger time step interval. The larger interval effectively considered differing time step sizes per conservation equation. The steps for the segregated solution retrieval every time steps can be enumerated by:

1. Retrieval of the shear rate magnitude, denoted in equation 5.2, corresponding to the result of the previous time step.
$$\dot{\gamma}_m = \textbf{setShearRateMagnitude}(\boldsymbol{u}_m).$$
2. Initiation of the outer loop fixed-point iterations, or so-called PIMPLE loop.
WHILE $(n \leq N_{\text{PIMPLE}})$.
3. Determination of the non-Newtonian viscosity, denoted in equation 5.10.
$$\nu_m = \textbf{setKinematicViscosity}(\dot{\gamma}_m, \alpha_d).$$
4. Solving for the mixture momentum and mass conservation, respectively denoted in equations 8.2 and 8.4.
SOLVE **UEqn**.
SOLVE **pEqn**.
5. Solving for the dispersed phase mass conservation, denoted in equation 8.6.
SOLVE **HtEqn**.
6. Solving for the oxygen mass conservation, denoted in equation 8.7.
SOLVE **PO2Eqn**.

The previous time step consideration of the shear rate magnitude greatly improved the observed stability of the solver. The accuracy did not diminish greatly by the consideration, as the shear rate magnitude did not show great differences between time steps.

8.3.2 Iterative Methods

The iterative methods chosen for each solver were tailored to the characteristics of the specific domain and the symmetry of the coefficient matrix of the linear system. The preference was to employ pre-conditioned Krylov subspace methods, with a focus on the Bi-Conjugate Gradient Stabilized method (Bi-CGSTAB/PBiCGStab). For asymmetric systems such as mixture momentum conservation, phasic mass conservation, and oxygen mass conservation, the Diagonal incomplete-LU (ILU/DILU) pre-conditioning was applied.
In the case of the pressure equation, utilized to enforce the mass conservation constraint, the Diagonal incomplete-Cholesky (IC/DIC) pre-conditioning was selected based on the symmetry of its coefficient matrix. However, numerical instabilities were encountered when resolving the pressure equation in the two-dimensional oxygenator domain, presented in section 8.4.3. The non-stationary iterative method was replaced with the (multi-grid accelerated) symmetric Gauss-Seidel method to address this issue.
Furthermore, stationary methods were found to smear the dispersed phase volume fraction solution in the centroid of the domain in consideration of the cyclic pipe domain, presented in section 8.4.1.

8.3.3 Numerical Schemes

The governing equations are discretized within OpenFOAM using the commonly considered finite volume method on a collocated polyhedral grid arrangement. The solution variables are stored in the grid cell centres, and the cell interactions across the interfaces are approximated using interpolated data. The typically considered numerical schemes for temporal and spatial discretization in this study were second-order accurate and are denoted in table 8.4.

OpenFOAM Variable	Mathematical formulation	Numerical Scheme
ddtSchemes	$\partial_t \phi$	CrankNicolson 0.9
gradSchemes	$\nabla \phi$	Gauss linear
divSchemes	$\nabla \cdot (\boldsymbol{u}_m \otimes \boldsymbol{u}_m)$	Gauss linear
	$\nabla \cdot (\nu_m \operatorname{dev}(\nabla \otimes \boldsymbol{u}_m)^+)$	Gauss linear
	$\nabla \cdot (\boldsymbol{u}_m \alpha_d)$	Gauss MUSCL
	$\nabla \cdot (\boldsymbol{u}_m p_{O_2})$	Gauss MUSCL
laplacianSchemes	$\nabla \cdot (\Gamma \nabla \phi)$	Gauss linear orthogonal
	$\nabla \cdot \left(\frac{1}{\mathcal{A}^h_{\boldsymbol{u}_m}} \nabla p^k_m \right)$	Gauss linear bounded
interpolationSchemes	ϕ_f	linear
snGradSchemes	$(\nabla_{\boldsymbol{n}} \phi)_f$	
	Structured grid	orthogonal
	Unstructured grid	corrected

Table 8.4: The numerical schemes utilized throughout this study for arbitrary solution variable ϕ, unless specified otherwise. The variable and scheme names correspond to the naming conventions of OpenFOAM.

Where dev denotes the deviatoric part of a second rank tensor, which is for the gradient

of the velocity field denoted by [38],

$$\nabla \otimes \boldsymbol{u} = \underbrace{\nabla \otimes \boldsymbol{u} - \frac{1}{3}(\mathrm{tr}\,(\nabla \otimes \boldsymbol{u})\,\boldsymbol{\mathcal{I}}}_{\text{Deviatoric}} + \underbrace{\frac{1}{3}(\mathrm{tr}\,(\nabla \otimes \boldsymbol{u})\,\boldsymbol{\mathcal{I}}}_{\text{Spherical}} = \mathrm{dev}\,(\nabla \otimes \boldsymbol{u}) + \mathrm{sph}\,(\nabla \otimes \boldsymbol{u})\,. \quad (8.19)$$

The consideration of the trace of the velocity field Jacobian should equate to zero in consideration of a divergence-free velocity field, but is in the solver still considered. The inclusion generally improves the stability of the non-converged system [43]. Additionally, $\mathcal{A}^h_{\boldsymbol{u}_m}$ denotes the diagonal of the coefficient matrix of the discretized mixture momentum equation without the pressure gradient. The consideration of the Total Variation Diminishing Monotone Upstream-centered Scheme for Conservation Laws (TVD-MUSCL) was required for the divergence discretization of the phasic mass conservation. As the solution of the dispersed phase volume fraction converged, the migratory flux would vanish, resulting in a hyperbolic character for the system.

8.4 Numerical Domain

Three primary domain types were utilized throughout this study. Their use case and characteristics are denoted in this section.

8.4.1 Cyclic Pipe

The cyclic pipe domain was primarily utilized to study the migratory behaviour of the red blood cells. This two-dimensional domain is illustrated in figure 8.2 and allowed for a computational cost-effective approach to approximate the steady-state solutions. The domain was chosen to be a so-called OH grid where an exterior O-shaped mesh is considered with an internal structured grid. The external mesh allowed refinement of the grid adjacent to the wall boundary to improve the approximation of normal gradients. The structured inner grid should, in turn, minimize the observation of numerical diffusion.

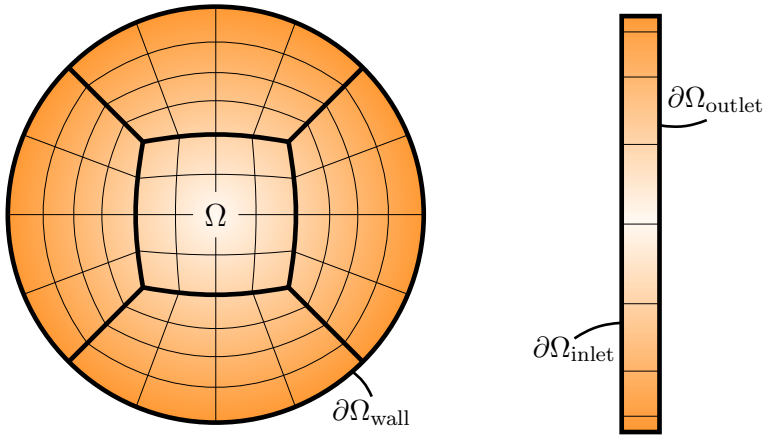

(a) Front view (b) Side view

Figure 8.2: The illustrated cyclic pipe flow domain discretization utilizing the commonly considered five block OH-grid, inspired by [103].

The illustrated inlet and outlet boundaries in this consideration did not adhere to the conditions presented in section 8.2. The inlet and outlet were typically considered translational cyclic or periodic. This periodic consideration ensured the inlet and outlet fields

were equivalent to promote the simplified approximation of steady-state solutions. The initial conditions, however, did adhere to the Dirichlet type inlet and outlet conditions. Additionally, the cyclic consideration required a momentum source term to model the flow correctly, which was modelled using the average flow velocity. The implementation within the OpenFOAM framework is presented in appendix C.2.3.
This domain type could not be simplified further to a one-dimensional axisymmetric domain as the so-called wedge boundary conditions applied in such a consideration enforce a zero gradient. The consideration of a zero gradient would result in an inflow of dispersed phase mass, as this did not necessarily enforce a zero migration flux.

8.4.2 Axisymmetric Pipe

The axisymmetric pipe domain was primarily utilized to study the oxygenation of whole blood. This two-dimensional domain is illustrated in figure 8.3 and, in contrast to the migration description, did allow the consideration of zero gradients on the wedge boundaries.

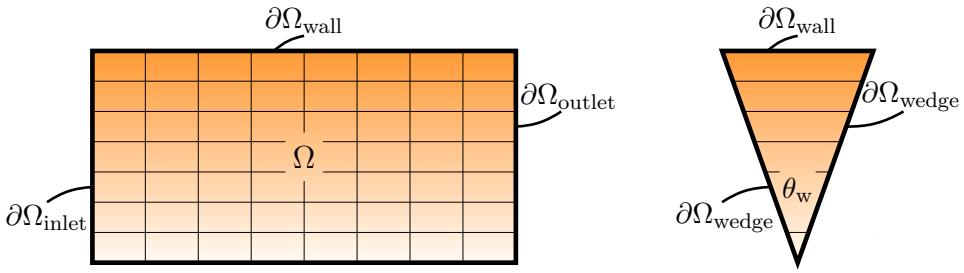

(a) Side view (b) Front view

Figure 8.3: The illustrated axisymmetric pipe flow domain discretization utilizing a simple structured grid, inspired by [38].

The illustrated axisymmetric domain generally introduces a geometrical error because the wall consideration is entirely normal to the radial direction. The error becomes negligible by consideration of a wedge angle of $\theta_{\text{w}} = 1°$ [38] which was, therefore, considered in this study. The introduction of the migration of red blood cells was realized in this domain by mapping the results retrieved on the cyclic domain discussed in the previous section. Since the cell centres of the finite volumes between the two domains were not always perfectly aligned, a linear interpolation based on the SciPy Python library was used.

8.4.3 Two-Dimensional Oxygenator

A simple two-dimensional staggered fibre arrangement was considered to more realistically model migration and oxygenation within a hollow-fibre membrane oxygenator. In this regard, two variants were utilized: a fully and semi-cyclic domain. The fully cyclic domain was primarily considered to study the particle migration and is illustrated along with its domain characteristics in figure 8.4. The semi-cyclic domain is illustrated in figure 8.5 and was considered to additionally study oxygenation. The domain comprises N consecutive fully cyclic domains, including an inlet and outlet region.

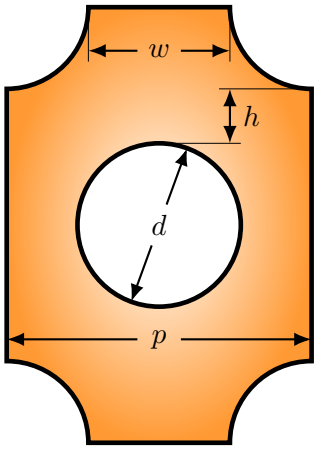

Figure 8.4: The illustrated fully cyclic two-dimensional oxygenator domain, inspired by [51].

Unfortunately, during the meshing of the semi-cyclic domain, a domain with differing characteristics from the fully cyclic domain was considered. The differences in characteristics are denoted in table 8.5. The typical long calculation times of the flow and oxygenation within this domain did not permit the consideration of the correct characteristics.

	d (mm)	h (mm)	p (mm)	w (mm)	N $(-)$
fully	0.3	0.1	0.56	0.26	-
semi	0.4	0.0	0.8	0.4	20

Table 8.5: The domain characteristics of the fully and semi-cyclic two-dimensional oxygenator numerical domain. The fully cyclic dimensions were considered following the considerations of Kaesler et al. [51].

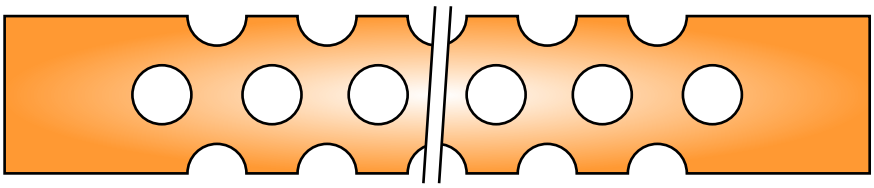

Figure 8.5: The illustrated semi-cyclic two-dimensional oxygenator domain, inspired by [51].

8.5 Solver and Solution Verification

The verification of the solver and its produced solutions is an integral part of any numerical study. The tools considered in this study in this regard are discussed within this section.

8.5.1 Implementation Verification

The workings of the solver itself can first be verified before diving into the physical correctness of the solutions. This study employed the method of manufactured solutions (MMS).

The method provides a systematic approach to validate whether the numerical solutions are congruent with solutions to the original differential equation. MMS involves proposing a known analytical solution, introducing it into the governing equations, and using the resulting remainder to correct the numerical implementation.
A more complete explanation, including a worked example, is provided in appendix B.2, along with the imposed manufactured solutions employed in this study in appendix B.3.

8.5.2 Migration Verification

The verification of the physical correctness of the migratory behaviour involved two methods. Firstly, the solution to the phasic mass conservation under steady state was compared to an analytical solution considering the Krieger-Dougherty viscosity model, as denoted in equation 5.8. The analytical solution, derived by Phillips et al. [82], is expressed for pipe flow denoted by,

$$\alpha_d^{\mathrm{KD}}(r) = \frac{\alpha_d^{\max}}{1 + \dfrac{\alpha_d^{\max} - (\alpha_d)_{\partial\Omega_{\mathrm{wall}}}}{(\alpha_d)_{\partial\Omega_{\mathrm{wall}}}} \dfrac{r}{R}}. \tag{8.20}$$

Where $\alpha_d^{\max} = 0.68$ is the maximum packing density and $(\alpha_d)_{\partial\Omega_{\mathrm{wall}}}$ the value observed at the wall. In this study, solver divergence occurred when applying the no-penetration boundary condition, leading to the adoption of a constant value, $(\alpha_d)_{\partial\Omega\mathrm{wall}} = 0.3$.
The second verification method was already introduced in chapter 2. The method concerns comparing area and mass flow rate averaged dispersed phase volume fraction solutions to the empirical observations by Pries et al. [86]. The empirical relation was denoted in equation 2.1,

$$\frac{\varphi^t}{\varphi^d} = \varphi^d + (1 - \varphi^d)(1 + 1.7e^{-0.35D} - 0.6e^{-0.01D}). \tag{2.1}$$

Where the tube haematocrit, φ^t, denoted the area averaged value further introduced in section 8.5.4.3. The mass flow rate averaged results denote the discharge haematocrit, φ^d, further introduced in section 8.5.4.2.

8.5.3 Oxygenation Verification

The results of the oxygenation model should be conservative in terms of the amount of oxygen that enters and leaves the numerical domain under steady-state conditions. This conservative nature can be tried by comparing the inflow and outflow of material. The inflow was solely considered over the wall, and the outflow over the outlet. Integrating the governing conservation equation over the numerical domain can determine the material flows. For the inflow, this is relatively straightforward as this is governed by the diffusive flux and is denoted by,

$$\mathcal{Q}_{\mathrm{in}} = \int_\Omega \nabla \cdot (\mathcal{D}_{\mathrm{eff}} \nabla p_{O_2,m})\, dV \overset{\mathrm{Gauss}}{=} \int_{\partial\Omega} (\mathcal{D}_{\mathrm{eff}} \nabla p_{O_2,m}) \cdot \boldsymbol{n}\, dS. \tag{8.21}$$

Where the inflow boundary is taken as $\partial\Omega = \partial\Omega_{\mathrm{wall}}$. The outflow cannot be derived as straightforwardly as the structure of the relation does not allow the immediate application of Gauss' divergence theorem. Instead, the advective contribution is split into an outflow

and a source contribution as denoted by,

$$\begin{aligned}
&\int_{\Omega}(1+C_{HbO_2})\nabla\cdot(\boldsymbol{u}_m p_{O_2,m})\,dV \\
&=\int_{\Omega}\nabla\cdot([1+C_{HbO_2}]\boldsymbol{u}_m p_{O_2,m})\,dV-\int_{\Omega}(\boldsymbol{u}_m p_{O_2,m})\cdot\nabla C_{HbO_2}dV \\
&\overset{\text{Gauss}}{=}\underbrace{\int_{\partial\Omega}(1+C_{HbO_2})\boldsymbol{u}_m p_{O_2,m}\cdot\boldsymbol{n}\;dS}_{\mathcal{Q}_{\text{out}}}\underbrace{-\int_{\Omega}(\boldsymbol{u}_m p_{O_2,m})\cdot\nabla C_{HbO_2}dV}_{\mathcal{S}_{\text{adv}}}.
\end{aligned}\tag{8.22}$$

Where the out flow boundary is taken as $\partial\Omega=\partial\Omega_{\text{outlet}}$ and $\mathcal{S}_{\text{adv}}$ denotes the advective source term. The numerical source term is now denoted by,

$$\mathcal{Q}_{\text{out}}+\mathcal{S}_{\text{adv}}+\mathcal{S}_{\text{num}}=\mathcal{Q}_{\text{in}}\Rightarrow\mathcal{S}_{\text{num}}=\mathcal{Q}_{\text{in}}-(\mathcal{Q}_{\text{out}}+\mathcal{S}_{\text{adv}}).\tag{8.23}$$

8.5.4 Comparison Metrics

In this study several comparison metrics were utilized for more convenient comparison between large sets of data. These comparison metrics and their notation are discussed in this section.

8.5.4.1 Normalized P-Norm

The normalized p-norm is a commonly used vector magnitude measure, normalized using the vector length N. The norm allows the comparison of vector data using a single number and is for an arbitrary vector quantity ϕ denoted by,

$$\|\phi\|_p\coloneqq\left(\frac{1}{N}\sum_{n=0}^{N-1}|\phi_n|^p\right)^{\frac{1}{p}},\quad\phi_n\in\phi.\tag{8.24}$$

In the limiting case, typically denoted the supremum norm, the norm evaluates the maximum value of the vector as denoted by,

$$\|\phi\|_\infty\coloneqq\lim_{p\to\infty}\|\phi\|_p=\max\left(|\phi_0|,|\phi_1|,\ldots,|\phi_{N-1}|\right).\tag{8.25}$$

8.5.4.2 Mass Flow Rate Averaging in Two-Phase Flows

In internal incompressible flows, no generic reference variable can be used to average over, as generally seen in external flows [21]. To this end, the flow quantities are averaged using mean quantities derived from conservation principles. In two-phase flows, there is, however, not a single way of deriving this, but three. All three are in turn related. The mixture consideration is equivalent to the single-phase and is denoted by,

$$\dot{m}_m\coloneqq\rho_m\langle|u_m|\rangle_m A_\perp\equiv\int_{\partial\Omega}\rho_m u_m dS.\tag{8.26}$$

Where $A_\perp$ denotes the cross-sectional area perpendicular to the dominant flow direction. The mixture consideration can be split up into the two phasic contributions using equation 3.16,

$$\Rightarrow\dot{m}_m=\underbrace{\int_{\partial\Omega}\alpha_d\overline{\overline{\rho}}_d\widetilde{u}_d dS}_{\substack{\text{Dispersed phase}\\\text{mass flow rate}}}+\underbrace{\int_{\partial\Omega}\alpha_c\overline{\overline{\rho}}_c\widetilde{u}_c dS}_{\substack{\text{Continuous phase}\\\text{mass flow rate}}}=\dot{m}_d+\dot{m}_c.\tag{8.27}$$

Where the contribution of the dispersed phase was of most interest in this study, and its value could be approximated using the mixture velocity under the Stokesian suspension assumption,

$$\dot{m}_d = \int_{\partial\Omega} \alpha_d \overline{\overline{\rho}}_d \widetilde{u}_d dS \approx \int_{\partial\Omega} \alpha_d \overline{\overline{\rho}}_d u_m dS. \tag{8.28}$$

The mass flow rate averaged velocity for the mixture is now denoted by,

$$\langle |u_m| \rangle_m = \frac{1}{\rho_m A_\perp} \int_{\partial\Omega} \rho_m u_m dS. \tag{8.29}$$

The mass flow rate averaging can also be extended to consider other arbitrary considerations, such as energy. The generalized consideration for a mixture mass flow rate averaged arbitrary variable ϕ is denoted by,

$$\langle |\phi_m| \rangle_m = \frac{1}{\dot{m}_m} \int_{\partial\Omega} \rho_m u_m \phi_m dS. \tag{8.30}$$

Additionally, the dispersed phase mass flow rate averaged arbitrary variable ϕ is denoted by,

$$\langle |\widetilde{\phi}_d| \rangle_d \approx \frac{1}{\dot{m}_d} \int_{\partial\Omega} \alpha_d \overline{\overline{\rho}}_d u_m \widetilde{\phi}_d dS. \tag{8.31}$$

8.5.4.3 Area Averaging

The technique of area averaging is, in addition to mass flow rate averaging, a commonly considered technique. For area averaging, no additional phasic considerations were done, and the area-averaged arbitrary quantity ϕ is denoted by,

$$\langle \phi \rangle_{\partial\Omega} = \frac{1}{A_{\partial\Omega}} \int_{\partial\Omega} \phi dS. \tag{8.32}$$

Where $A_{\partial\Omega}$ denotes the area of boundary $\partial\Omega$.

Chapter 9

Results and Discussion

The numerically derived results are presented and discussed in this chapter. Before the detailed discussion of the results, the credibility of the numerical framework is established by addressing the solver implementation, migration model, and oxygenation model verification.
For a comprehensive understanding, the influence of the particle migration is studied in the context of axisymmetric pipe flow. Subsequently, the analysis is extended to the consideration of a two-dimensional oxygenator. In addition to the influence of particle migration modelling, rheological modelling and the presence of particles are discussed. Finally, the underlying assumptions of the mixture modelling consideration and a comparison between the newly derived oxygenation model and a commonly considered model are discussed.

9.1 Implementation Verification

In the numerical analysis of physical phenomena, the processes of model verification and validation are essential considerations before delving into the numerical solutions. In this study, a new solver was implemented and utilized using the open-source OpenFOAM framework. An implementation verification is indispensable to ensure the quality of the implementation and verify that the solver approximates solutions to the intended differential equations. This verification is conducted using the method of manufactured solutions, as discussed in section 8.5.1 and appendix B.2.
The manufactured solutions imposed on the system are discussed in appendix B.3, and the resulting numerical errors for a grid study on a unity cube are presented in figure 9.1. The boundary conditions imposed on the numerical system were Dirichlet boundary conditions that follow from the imposed solutions evaluated at the boundaries.

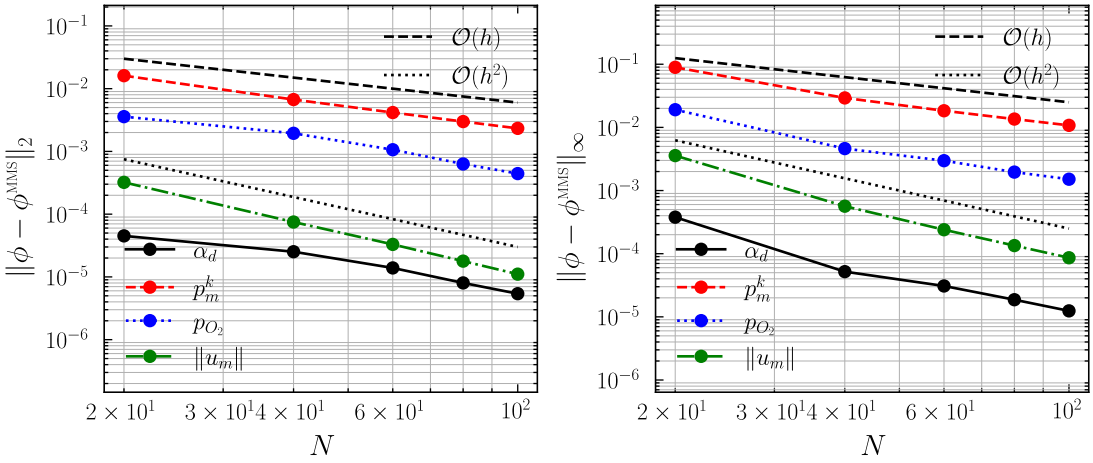

(a) Normalized Euclidean norm

(b) Supremum norm

Figure 9.1: The numerical error with respect to manufactured solutions for the four dependent solution variables and the expected numerical scheme convergence order. The results were derived using an equispaced grid of N discrete volumes in each spatial dimension on a unity cube at time $t = 1$.

The resulting numerical errors presented in figure 9.1, as a function of the number of grid cells N in any spatial direction, show good agreement with the order-of-accuracy of the numerical schemes employed in this study. The utilized schemes are generally second-order accurate and were denoted in section 8.3.3. The order of accuracy in the figures was depicted using the equidistant grid spacing h. This spacing reduces to the reciprocal of the number of grid cells due to the unity domain size and is defined as $h \coloneqq \frac{L}{N} = \frac{1}{N}$.
One solution that stands out is that for the kinematic pressure, as it generally showed an accuracy one order lower. Such behaviour is typically linked to the boundary treatment, where the elliptic nature of the pressure equation narrows it down to the discretization of the surface normal gradient. The consideration of a first-order accurate boundary treatment appears consistent with the gradient boundary discretization discussed in [38].

9.2 Migration Verification

With the mathematical consistency of the solver verified in the preceding section, attention should be shifted towards the physical correctness of the numerical solutions. In this section, the behaviour of the implementation regarding the particle migration modelling is discussed.

9.2.1 The Steady-State Analytical Solution

The numerical approximations can be compared to analytical solutions to verify whether the implemented migration model can produce physically relevant solutions. The analytical solution for the drift flux model was discussed in section 8.5.2 and required utilising the Krieger-Dougherty viscosity model. The model parameters utilised in this analysis where $\alpha_d^{\max} = 0.68$ and $m = 1.82$ following the considerations of Phillips et al. [82]. The analytical solution, as denoted in equation 8.20, required a wall value due to solver instability observed in the utilisation of the no-penetration boundary condition.

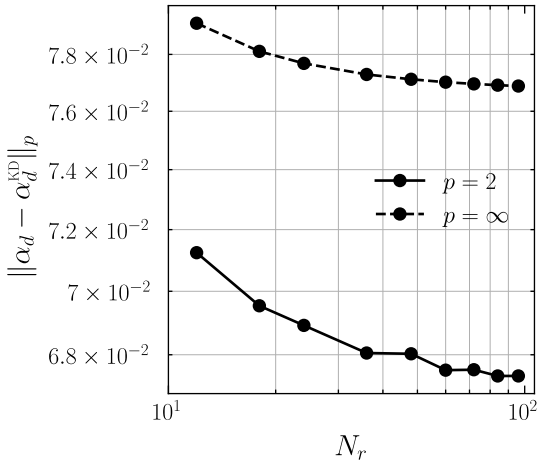

(a) Numerical error

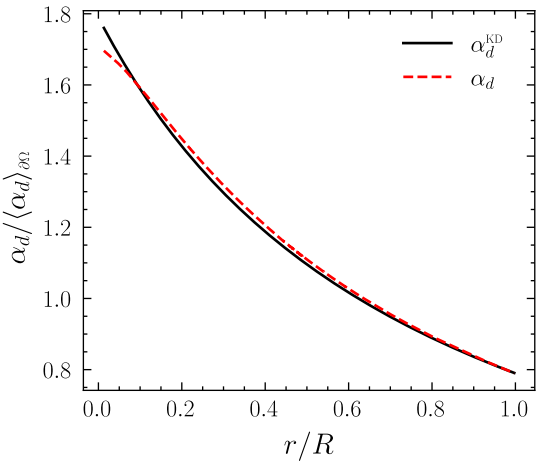

(b) **Analytical** and **finest grid numerical** solutions.

Figure 9.2: The numerical error and profile comparison for the steady state dispersed phase volume fraction using the Krieger-Dougherty viscosity model, where $\alpha_d^{\max} = 0.68$, $m = 1.82$ [82], and $(\alpha_d)_{\partial\Omega_{\mathrm{wall}}} = 0.3$.

The comparison of the analytical and numerical solutions is depicted in figure 9.2 and was derived for cyclic pipe flow with a singular cell in the longitudinal direction. The analysis considered a tube radius of $R = 50\,\mu\mathrm{m}$, average velocity of $U = 9.55\,\mathrm{mm/s}$, an initial uniform dispersed phase volume fraction of $\alpha_{d,0} = \langle \alpha_d \rangle_{\partial\Omega} = 0.38$, and a wall value of $(\alpha_d)_{\partial\Omega_{\mathrm{wall}}} = 0.3$.
The numerical errors presented in figure 9.2a generally show a decrease for an increasing number of grid cells in the radial direction. However, the order of reduction, indicated by the gradient of the graph, seems to decline as the number of grid cells increases. This decline can be linked to the nonphysical nature of the viscosity model near the central line of the pipe flow. The value of the dispersed phase volume fraction here approaches the maximum value of $\alpha_d^{\max}$ such that $\lim_{\alpha_d \to \alpha_d^{\max -}} \mu_m^{\mathrm{KD}} = +\infty$.
Naturally, an infinite viscosity is impossible to converge to, such that the central line value for the dispersed phase volume fraction converges to a value slightly lower than $\alpha_d^{\max}$. These differing values of the viscosity profile additionally result in differing shear rate magnitudes, resulting in a small error throughout the entire approximation, as presented in figure 9.2b.

9.2.2 The Fåhræus Effect

In addition to the comparison with an analytical solution, the derived numerical solutions could also be compared to empirical observations. Typically, in literature, this verification is done using the empirical relation denoted in equation 2.1, which quantified the Fåhræus effect. Although a proper validation by, e.g. comparison to profile development, would be preferred, these considerations appear unreported in the literature. Therefore, the numerical solutions are also compared to the Fåhræus effect quantification for which the results are presented in figure 9.3a.

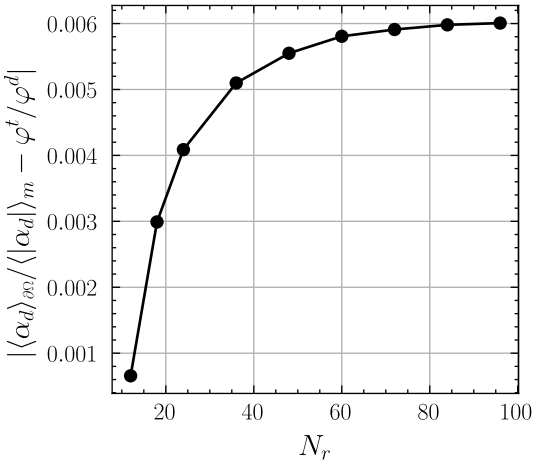

(a) The absolute error of the ratio of the tube and discharge haematocrit compared to the empirical relation derived by Pries et al. [86] with respect to the number of radial grid cells.

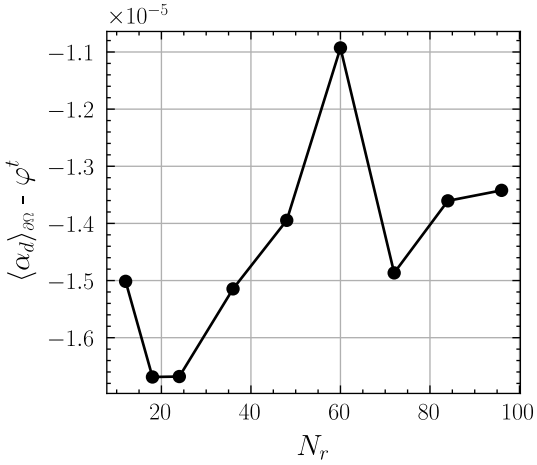

(b) The numerical error of the tube haematocrit with respect to the number of radial grid cells.

Figure 9.3: The Fåhræus effect and phasic mass conservation.

The numerical errors are depicted in figure 9.3 and were derived for cyclic pipe flow with a singular cell in the longitudinal direction, tube diameter of $D = 100\,\mu\text{m}$, average velocity of $U = 9.55\,\text{mm/s}$, and an initial uniform dispersed phase volume fraction of $\alpha_{d,0} = \langle\alpha_d(\boldsymbol{x})\rangle_{\partial\Omega} = 0.45$. The errors are presented with respect to an increasing amount of radial grid cells and appear to approach a constant value of about 0.6%. This observed error is an order lower than the error reported by Chandran et al. [22], where the difference can be attributed to the differing rheological model under consideration.
Additionally, the observation of the convergent behaviour to a nonzero value can be attributed to the consideration of the model coefficients $C^{\text{C}}_{\boldsymbol{\mathcal{T}}^D_{1_d}}$ and $C^{\mu}_{\boldsymbol{\mathcal{T}}^D_{1_d}}$. In this study, these were considered to be constants, denoted in table 8.2, which correspond to the lateral migration of spherical particles. Regarding the flow of blood, the exact value of these coefficients might differ or even be functions of the dependent variables and domain characteristics. The consideration of functional coefficients was already proposed as further work by Chandran et al. [22] to improve the accuracy of the diffusive flux model in the description of blood flow.
Lastly, the measurement of the tube or cross-sectional averaged haematocrit field allowed the review of the mass conservation of the diffusive flux model and the no-penetration wall boundary condition denoted in section 8.2.2. The resulting errors, with respect to the grid size, are presented in figure 9.3b and show chaotic behaviour that does not appear to converge to a singular value. However, the magnitude of the error is of the order 1×10^{-5} and shows a slight loss of mass. This slight loss in mass can be attributed to the gradual application of the wall boundary condition required to improve the stability of the solver, as was discussed in section 8.2.2.

9.3 Oxygenation Verification

In addition to the migration model, the physical correctness regarding the oxygenation modelling should be considered. While a proper validation, e.g. comparison to profile

development, would be preferred, this is generally impossible and appears unreported in the literature. Typically, however, the numerical solutions for the mean or mass-flow-averaged oxygen saturation or partial pressure at the outlet of the numerical domain are compared to empirically measured results. This comparison was considered out-of-scope in this study, and purely numerical considerations were made.

A straightforward consideration to verify whether the derived numerical results are physically relevant is to derive whether the mass of oxygen is indeed conserved in the numerical domain. The derivation of a numerically induced source or sink term was presented in section 8.5.3, and the scaled results are presented in figure 9.4.

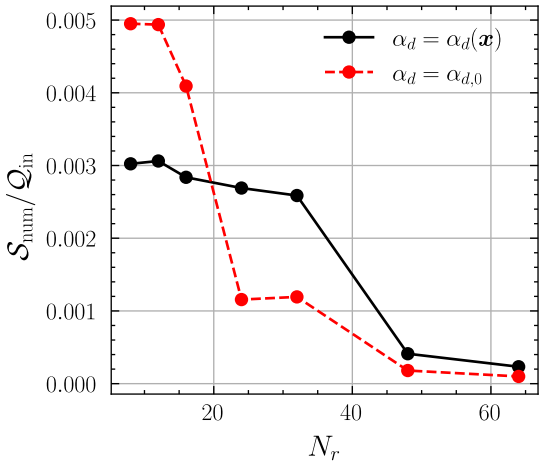

Figure 9.4: The relative total oxygen mass flow error or numerical source contribution for **variable** and **uniform** dispersed phase volume fraction profiles.

The resulting errors, depicted in figure 9.4, were derived for axisymmetric pipe flow with a tube radius of $R = 50\,\mu\text{m}$, average velocity of $U = 9.55\,\text{mm/s}$, and two dispersed phase volume fraction profiles. The profiles correspond to a uniform and variable profile where $\alpha_{d,0} = \langle \alpha_d(\boldsymbol{x}) \rangle_{\partial\Omega} = 0.45$. The variable profile is presented in figure 9.5a.
The figure shows that the relative numerical error for a coarse radial grid shows a slight creation of oxygen, composing about 0.5% of the inflow. This percentage rapidly decreased towards 0% as the number of grid cells in the radial dimension increased, and therefore, the wall flux approximation accuracy increased. The figure also depicts a difference in accuracy between the consideration of a uniform and a variable dispersed phase volume fraction profile. This difference might be attributed to a more accurate representation of the wall value of the dispersed phase volume fraction as the grid is refined.

9.4 The Influence of Particle Migration on Oxygenation in Axi-symmetric Pipe Flow

With the implementation and physical response of the numerical solver verified, the numerical results of particle migration and oxygenation can finally be discussed. In this section, the effect of the particle migration on the oxygenation in axisymmetric pipe flow is discussed.

9.4.1 Hydrodynamic Developed Profiles

The profile development of quantities of interest in axisymmetric pipe flow can generally be simplified into two-dimensional or even one-dimensional considerations. These considerations drastically reduce the computational cost and allow quick comparison between case studies. However, in the consideration of both migration and oxygenation, the observation of profile development requires the consideration of three-dimensional domains. The migration cannot be considered in an axisymmetric domain. The so-called wedge boundaries in the tangential direction simulate a zero gradient in the profile, not a zero migration flux, and would generally introduce a non-physical inflow of dispersed phase mass.
On the other hand, the analysis of oxygenation development could not be done with a cyclic inlet-outlet boundary condition, as this would quickly result in a uniform profile equal to the wall oxygen partial pressure. In this consideration, wedge domains were utilized to study the oxygenation to which the velocity and dispersed phase volume fraction profiles were mapped in the radial direction. The mapped profiles for two pipe diameters, average velocity of $U = 9.55\,\mathrm{mm/s}$, and initial dispersed phase volume fraction of $\alpha_{d,0} = \langle \alpha_d(\boldsymbol{x}) \rangle_{\partial\Omega} = 0.45$ are depicted in figure 9.5.

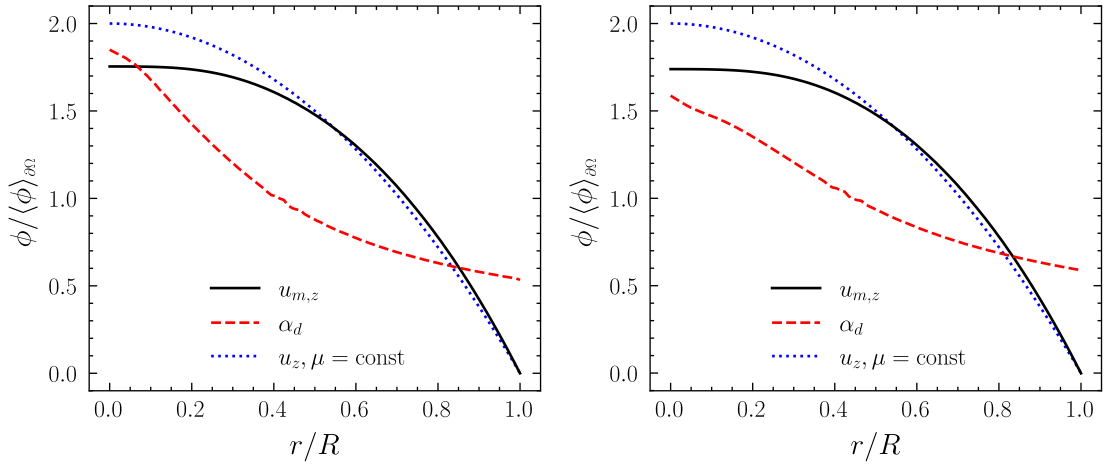

(a) $D = 100\,\mu\mathrm{m}$. (b) $D = 300\,\mu\mathrm{m}$.

Figure 9.5: Comparison of **non-Newtonian** and **Newtonian** velocity fields along with the **dispersed phase volume fraction** in pipe flow for two diameters, average velocity of $U = 9.55\,\mathrm{mm/s}$, and initial dispersed phase volume fraction of $\alpha_{d,0} = \langle \alpha_d(\boldsymbol{x}) \rangle_{\partial\Omega} = 0.45$.

The resulting profiles, as presented in figure 9.5, show nicely how a smaller domain with identical average velocity results in a higher shear rate magnitude gradient and, therefore, a more pronounced effect of migration. The dispersed phase volume fraction is especially of higher magnitude near the centre of the domain, i.e. $r = 0$. The velocity profile, on the other hand, although blunt compared to the Newtonian profiles, does not appear to be influenced significantly by the variation in dispersed phase volume fraction. The small oscillation near the centre of the profile in the dispersed phase volume fraction can be attributed to numerical errors related to the corner elements of the structured internal region of the OH-grid, illustrated in figure 8.2.

9.4.2 Oxygenation Boundary Layer Development

The profile development of the oxygen partial pressure and saturation fields in the entrance region were compared to review the influence of the variable dispersed phase volume fraction. The velocity field and dispersed phase volume fraction field were considered to be already fully developed and correspond to the profiles presented in figure 9.5b.
The profile development of the variable and uniform fields, alongside their boundary layer thickness profiles, are respectively presented in figures 9.6a and 9.6b. The boundary thickness values were derived by linear interpolating the field data along the radial axis. The interpolation minimised the stepping nature of the results due to the evaluation at the discrete cell-centred positions. This interpolation also causes a sudden increase in thickness near the end of the saturation thickness profiles. The maximum values of both fields along the radial axis scale the profile heights along the longitudinal axis. This scaling allows the comparison of the profile and magnitude of the fields for the variable and uniform cases. The resulting scaling for the partial pressure now does not correspond to the exact wall value, as only the cell-centred values were considered. This consideration improved the visibility of the profiles along the radial axis, as the internal field values were generally much smaller in the entrance region. However, the penetration depths of the partial pressure profiles now seem to mismatch the boundary layer thicknesses, which is thus a consequence of the altered scaling.

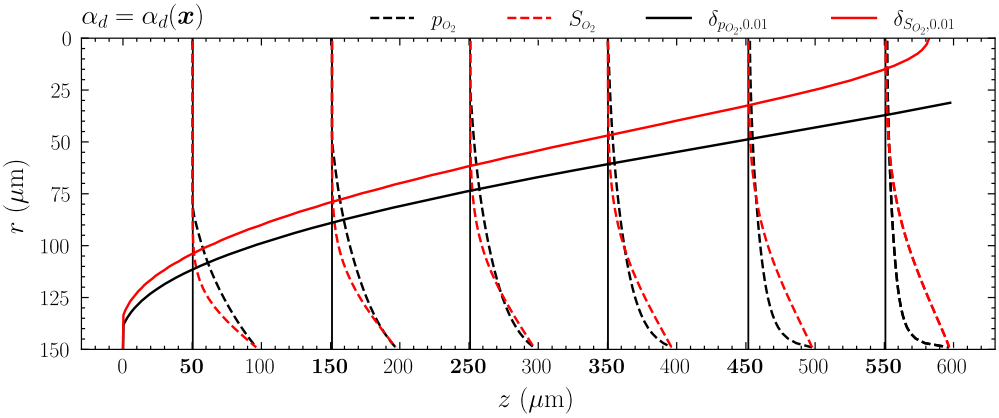

(a) Variable dispersed phase volume fraction field.

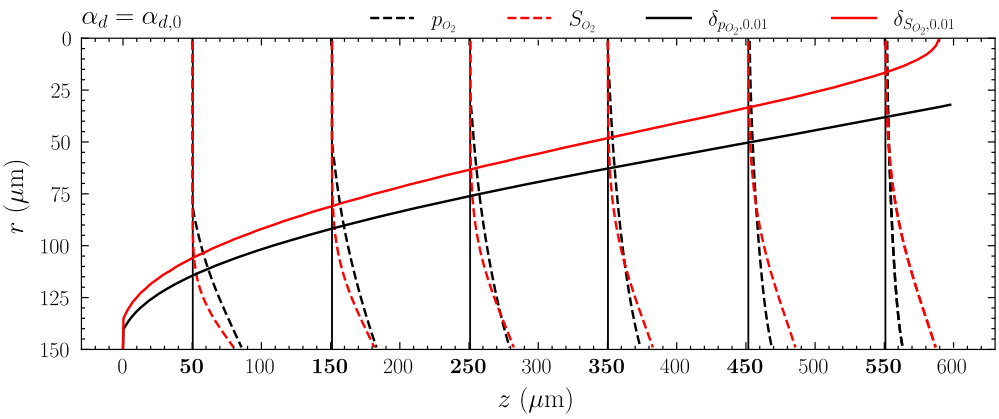

(b) Uniform dispersed phase volume fraction field.

Figure 9.6: **Oxygen partial pressure** and **saturation** profile development in the entrance region of pipe flow.

The resulting profiles presented in figure 9.6 show that, in the entrance region, the behaviour of the oxygen transport is significantly modified by the variable haematocrit profile. I.e. figure 9.6a generally shows a non-linear radial development with increasing non-linearity along the longitudinal axis. On the other hand, figure 9.6b shows nearly linear profiles. Additionally, the magnitude of the partial pressure and the saturation at the wall for the uniform dispersed phase volume fraction profile are generally lower than those observed for the variable profile.
This observation can rather intuitively be explained. The variable dispersed phase volume fraction profile has fewer red blood cells near the solid boundary than the uniform profile. This reduction effectively reduces the amount of available heme groups to which oxygen may bind, such that the smaller number of red blood cells achieve saturation much faster. When the red blood cells are fully saturated, the dissolved oxygen will pass through the saturated blood cells and diffuse towards the non-saturated blood cell core. This quickened diffusion is also evident from the significant increase in the dissolved oxygen partial pressure near the wall at the end of the variable profile. The partial pressure can increase faster because the oxygen is no longer bound to the blood cells.
The phenomenon can be further explored by considering the effective diffusivity profiles presented in figure 9.7.

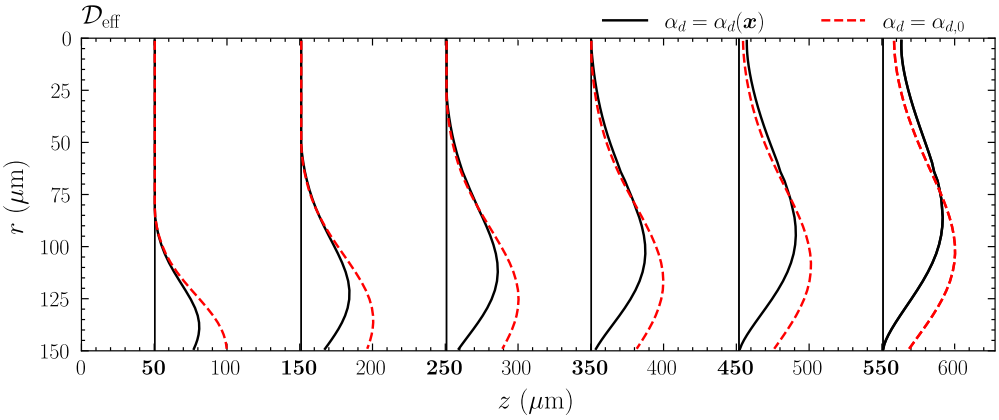

Figure 9.7: Effective diffusivity development profiles for **variable** and **uniform** dispersed phase volume fraction fields in the entrance region of pipe flow. The profiles correspond respectively to the partial pressure and saturation profiles shown in **figure 9.6a** and **figure 9.6b**.

The effective diffusivity for the uniform profile can be observed in figure 9.7 to be much larger near the inlet than that for the variable profile. This increased diffusivity effectively shows lower overall saturation of the blood cells due to the increased amount of blood cells present, coinciding with the observations in figure 9.6b. Furthermore, the faster saturation of the variable profile also becomes evident from the radial evolution of the effective diffusivity. As the blood cells become saturated, the value of the diffusivity again drops to that observed in the continuous phase. The saturation then causes the effective diffusivity for the variable field to drop drastically compared to that of the uniform field, causing a negative gradient in the field and, therefore, a flux cancellation. This cancellation is best envisioned by considering the expansion of the diffusive flux contribution, Which is denoted by,

$$\frac{1}{r}\frac{\partial}{\partial r}\left(r\mathcal{D}_{\text{eff}}\frac{\partial p_{O_2}}{\partial r}\right) = \mathcal{D}_{\text{eff}}\frac{\partial^2 p_{O_2}}{\partial r^2} + \left[\frac{\partial \mathcal{D}_{\text{eff}}}{\partial r} + \frac{\mathcal{D}_{\text{eff}}}{r}\right]\frac{\partial p_{O_2}}{\partial r}. \tag{9.1}$$

The gradient of the effective diffusivity, with respect to the radial direction, changes signs and effectively causes a diffusive flux directed towards the solid boundary. This flux cancellation causes the highly non-linear behaviour observed near the end of the entrance region in the oxygen partial pressure profile in figure 9.6a.

9.4.3 Oxygenation Developed Saturation Behaviour

The consideration of a uniform distribution for the dispersed phase volume fraction seemed to delay the oxygenation behaviour observed for the variable distribution primarily. This delayed behaviour is evidenced by the observation that, further from the entrance region, the radial dependence of the oxygen partial pressure and saturation profiles become equivalent, as presented in figure 9.8.

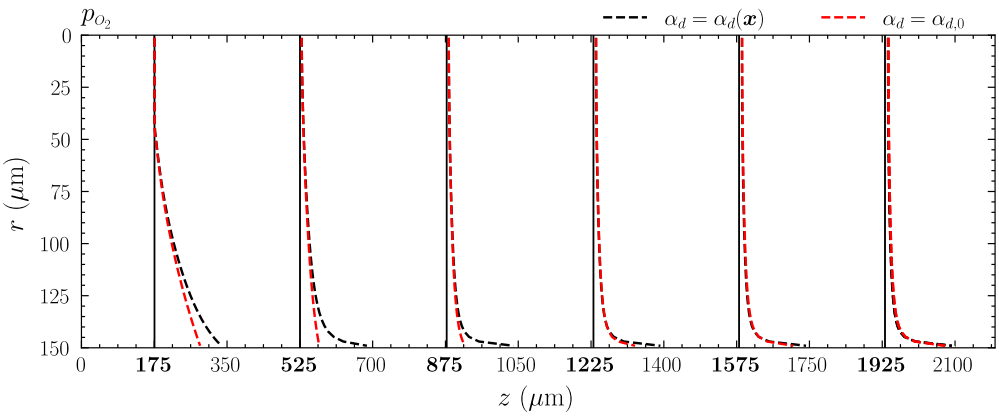

(a) Oxygen partial pressure.

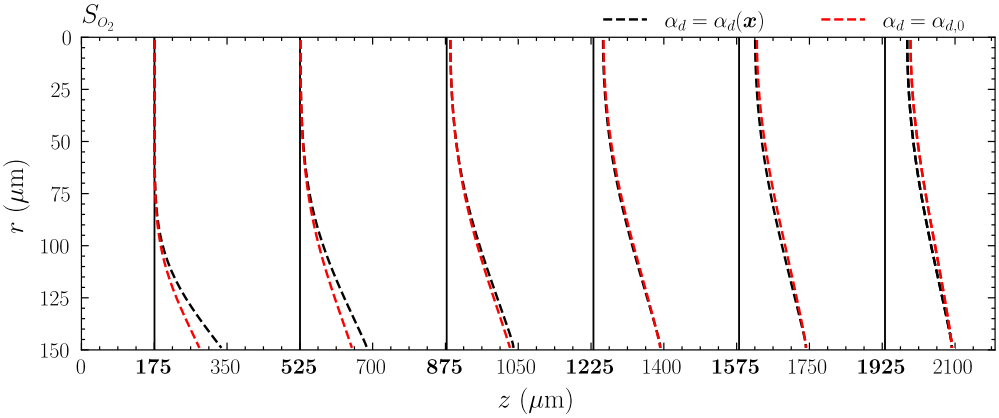

(b) Oxygen saturation.

Figure 9.8: Extended oxygen partial pressure and saturation profile development beyond the entrance region for **variable** and **uniform** dispersed phase volume fraction fields. The cases correspond to the entrance region development cases presented in figure 9.6.

The profiles for the uniform dispersed phase volume fraction oxygen partial pressure remained approximately linear for twice the entrance length, as can be observed in figure 9.8a, but show the development of the non-linear behaviour near the boundary similar to that of the variable profile results. The origin of this non-linear profile development can,

similarly to that observed for the variable case in the previous section, be attributed to the saturation of the blood cells near the domain boundary. Once these blood cells were fully saturated, the oxygen saturation profiles also appeared to become equivalent, with a slight difference near the central line of the pipe flow.
This slight difference in saturation appeared to be increasing along the longitudinal direction. It can be attributed to the heightened dispersed phase volume fraction, causing an elevated effective diffusivity, as shown in figure 9.9.

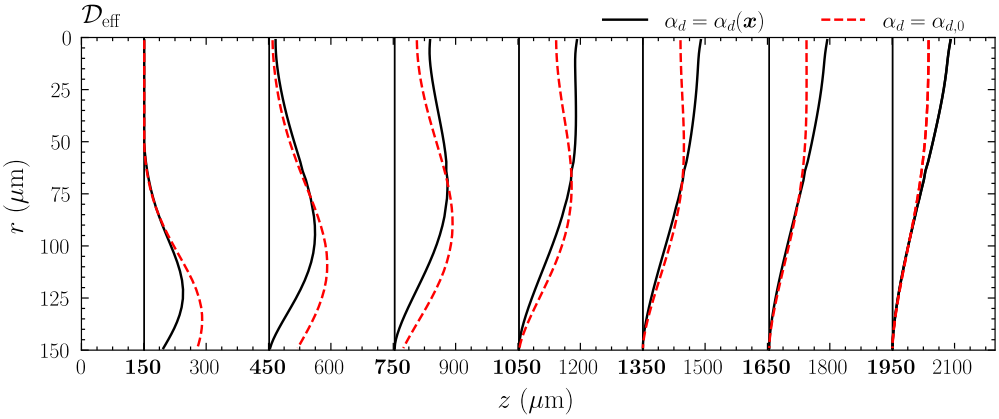

Figure 9.9: Extended effective diffusivity profile development beyond the entrance region for **variable** and **uniform** dispersed phase volume fraction fields. The profiles correspond to the oxygen partial pressure and saturation results presented in figure 9.8.

The effective diffusivity profiles presented in figure 9.9 show that, initially, there appears an inward propagation of a smoothed step function, similar to numerical dissipative results of advection scheme studies, with limiting values equivalent to the continuous phase diffusivity. In this regard, the propagation of the diffusivity for the uniform profile simply lags behind that of the variable profile. However, as the profile approaches the central line of the cylindrical domain, the value also increases faster, resulting in a nearly linear profile with respect to the radial direction. The final profiles show that the effective diffusivity in the variable dispersed phase volume fraction results is much higher near the central line. The heightened effective diffusivity causes the slight but increasing difference in the saturation along the longitudinal direction observed in figure 9.8b.

9.4.4 Pipe Flow Core Particle Distribution-Induced Oxygenation Resistance

The highly concentrated inner core of red blood cells in pipe flow was the primary resistance to oxygen uptake compared to a uniform distribution. The inner core appeared to show an increasing delay in blood oxygenation for the variable distribution, as illustrated in the preceding section. The delay can more conveniently be observed by considering the mass flow rate averaged saturation along the longitudinal axis presented in figure 9.10. Two types of mass flow rate averaging were considered, averaging with respect to the mixture and the dispersed phase. Both techniques were introduced in section 8.5.4.2.

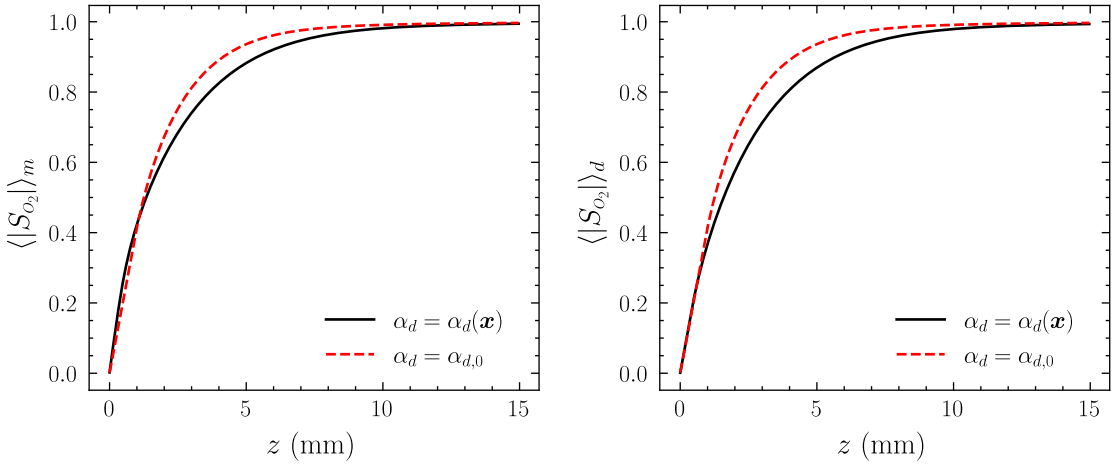

(a) Mixture.

(b) Dispersed phase.

Figure 9.10: The mass flow rate averaged oxygen saturation for **variable** and **uniform** dispersed phase volume fraction fields along the longitudinal axis.

The two averaging techniques depicted in figure 9.10 show that the primary difference in averaging techniques is found in the entrance region. The variable dispersed phase volume fraction profile for the mixture averaging, figure 9.10a, shows an overshoot compared to the uniform profile. This overshoot is solely caused by the consideration that blood is saturated faster when fewer red blood cells are present, extensively discussed in the two preceding sections. The dispersed phase mass flow rate averaging eliminates this distinction and shows that the two profiles overlap throughout the entrance region.
The delay in oxygenation showed, for this particular case, a difference up to about 10% in the averaged saturation and would suggest that the influence of migration is not negligible. The difference is, however, observed to diminish until the entire flow of blood is oxygenated. The maximum differences between the dispersed phase mass flow rate averaged oxygen saturation showed a linear dependence with respect to the difference between the wall and core value of dispersed phase volume fraction, as depicted in figure 9.11.

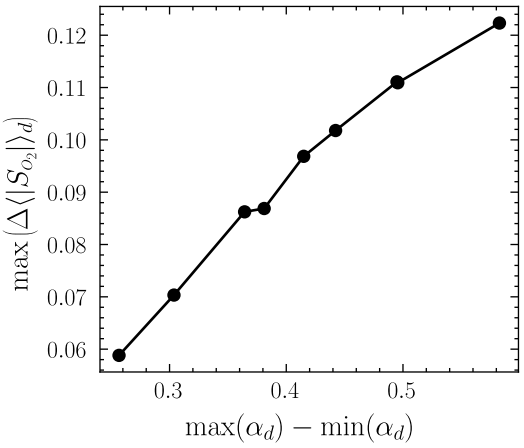

Figure 9.11: The maximum difference between the dispersed phase mass flow rate averaged saturation along the longitudinal axis for several pipe flow cases with differing degrees of migration.

The maximum differences of dispersed phase mass flow rate averaged saturation profiles, depicted in figure 9.11, were derived for the nine cases abiding $R = 50, 100, 150\,\mu\text{m}$, average velocity of $U = 2.12, 5.31, 9.55\,\text{mm/s}$, inspired by [51], and an initial uniform dispersed phase volume fraction of $\alpha_{d,0} = 0.45$.

9.5 Fully Developed Particle Migration and Oxygenation in a Two-Dimensional Oxygenator

The pipe flow considerations of the previous sections provided a convenient way to study and create an understanding of the influence of the variable red blood cell distributions on the oxygenation of whole blood. However, blood oxygenation in a pipe does not entirely represent the behaviour in a hollow-fibre membrane oxygenator. In this section, the fully developed migratory behaviour of red blood cells is studied in a two-dimensional staggered fibre arrangement, as was introduced in section 8.4.3.

9.5.1 Particle Migration Grid Sensitivity in a Cyclic Domain

First, a grid independence study is required to ensure the numerical solutions show the expected behaviour. This study considered phasic mass conservation accuracy and the comparison of dispersed phase volume fraction and velocity fields.

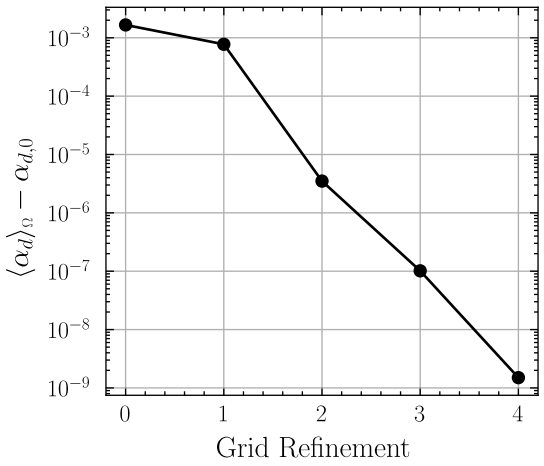

Figure 9.12: The numerical error of the volume-averaged dispersed phase volume fraction with respect to the grid refinement cases.

The phasic mass conservation with respect to the grid refinement cases is depicted in figure 9.12 and shows good agreement for all domains. The numerical solutions for the dispersed phase volume fraction and velocity fields are depicted in figure 9.13 and show convergent behaviour. The profiles are evaluated at the outlet of the cyclic numerical domain, located between two fibres. The velocity profile is already nearly converged for the first grid refinement, whereas the dispersed phase volume fraction still shows some fluctuations, even at the latest refinements.

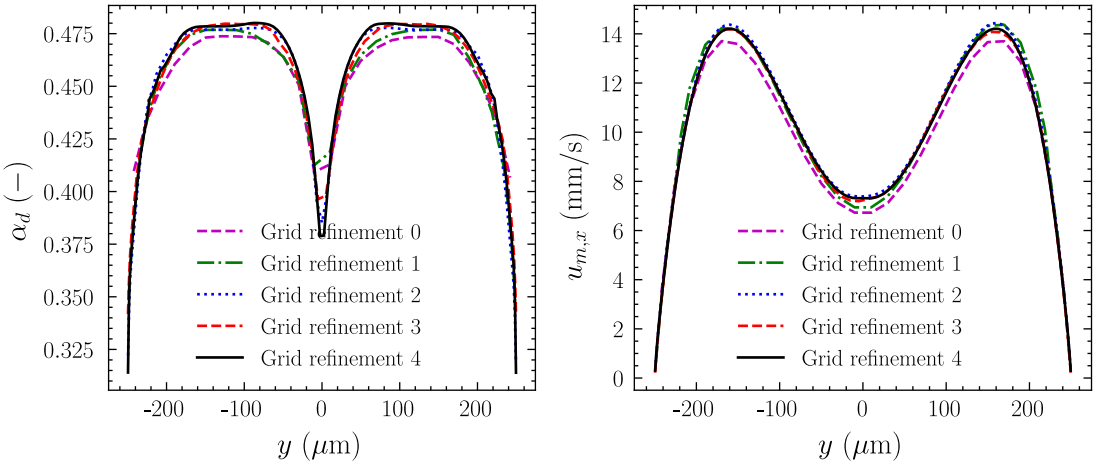

(a) Dispersed phase volume fraction.

(b) Velocity.

Figure 9.13: Grid independence study for the dispersed phase volume fraction and velocity fields measured in the cyclic staggered grid arrangement between two fibres.

9.5.2 Shear Induced Particle Migration in a Cyclic Domain

The shear-induced particle migration of red blood cells in whole blood is depicted in figures 9.13a and 9.14. The phenomenon appears dominant right next to the fibres and shows large local gradients. The bulk flow, however, remains primarily unaffected other than a slight increase in particle concentration due to mass conservation.

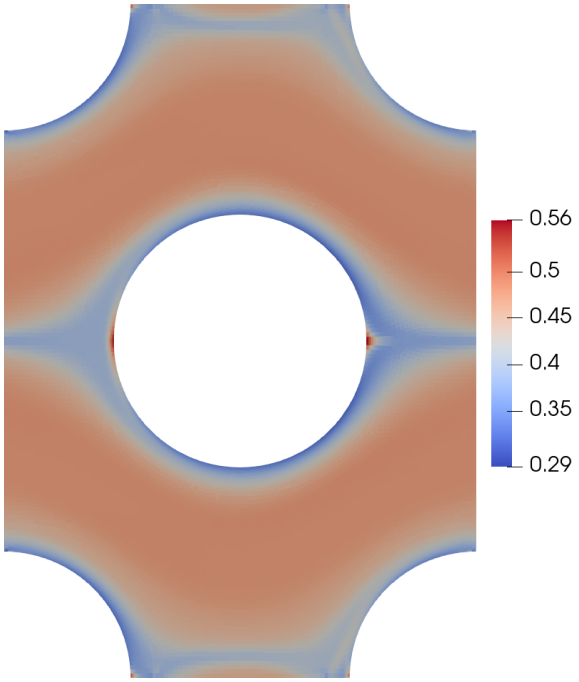

Figure 9.14: The fully developed dispersed phase volume fraction field for a cyclic staggered two-dimensional oxygenator domain for an average velocity of $U = 9.55\,\mathrm{mm/s}$, and initial dispersed phase volume fraction of $\alpha_{d,0} = \langle \alpha_d(\boldsymbol{x}) \rangle_\Omega = 0.45$.

The numerical results depicted in figure 9.14 were derived using an average velocity of $U = 9.55\,\mathrm{mm/s}$, and initial dispersed phase volume fraction of $\alpha_{d,0} = \langle \alpha_d(\boldsymbol{x}) \rangle_\Omega = 0.45$. The dispersed phase volume fraction field depicts a flow separation of particles introduced by the presence of the fibres in the flow. This behaviour opposes the migration observed in pipe flow, as the particles would concentrate away from the solid boundaries as depicted in figure 9.5. The opposing migratory behaviour would now also suggest that the primary resistance to oxygen uptake observed in pipe flow, as discussed in section 9.4.4, becomes non-existent in hollow-fibre membrane oxygenators.
The numerically derived solutions did show two non-physical numerical artefacts. Firstly, the migration profiles near the top and bottom of figure 9.14 show an increase rather than a decrease in particle concentration. The cyclic boundary conditions introduce this behaviour but do not influence the bulk flow around the central fibre. The migration model introduces the second numerical artefact. The results show a local particle concentration near the trailing edge of the fibre. While this behaviour makes sense near the stagnation point at the leading edge, near the trailing edge, this appears introduced by the typically low shear rate magnitude.

9.5.3 The Influence of Particle Migration on Oxygenation

The influence of shear-induced particle migration on the oxygenation of whole blood in a domain representative of an oxygenator was studied by considering the semi-cyclic two-dimensional oxygenator discussed in section 8.4.3. The mass flow rate averaged saturation behaviour of the solution can be studied similarly to the consideration of oxygenation resistance in pipe flow, discussed in section 9.4.4. In contrast to the pipe flow, there is no straightforward area of averaging. In this study, the boundary of axial periodicity was considered for the averaging, where the numerical solutions were derived through linear interpolation. Several domain discretizations were considered for both the migratory and non-migratory cases to ensure the solution was independent of the domain discretization. The solutions for this grid study are depicted in figure 9.15.

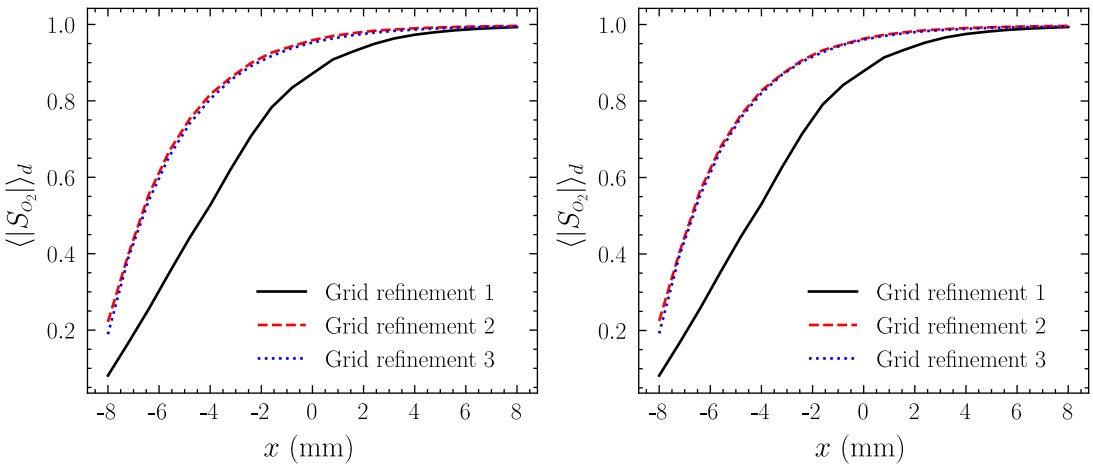

(a) Variable dispersed phase volume fraction field.

(b) Uniform dispersed phase volume fraction field.

Figure 9.15: Grid independence study for variable and uniform dispersed phase volume fraction field oxygenation in the semi-cyclic two-dimensional oxygenator. The grid refinement settings corresponded with the corresponding cases in figure 9.13.

The numerical results depicted in figures 9.15 and 9.16 were derived using an average velocity of $U = 9.55\,\mathrm{mm/s}$, and initial dispersed phase volume fraction of $\alpha_{d,0} = \langle \alpha_d(\boldsymbol{x}) \rangle_\Omega = 0.45$. The grid dependence studies show a good agreement between the two latest considered refinement cases for both the migratory and non-migratory results, such that the results can be considered independent of the domain discretization. The fine grid results for both cases are compared in figure 9.16a.

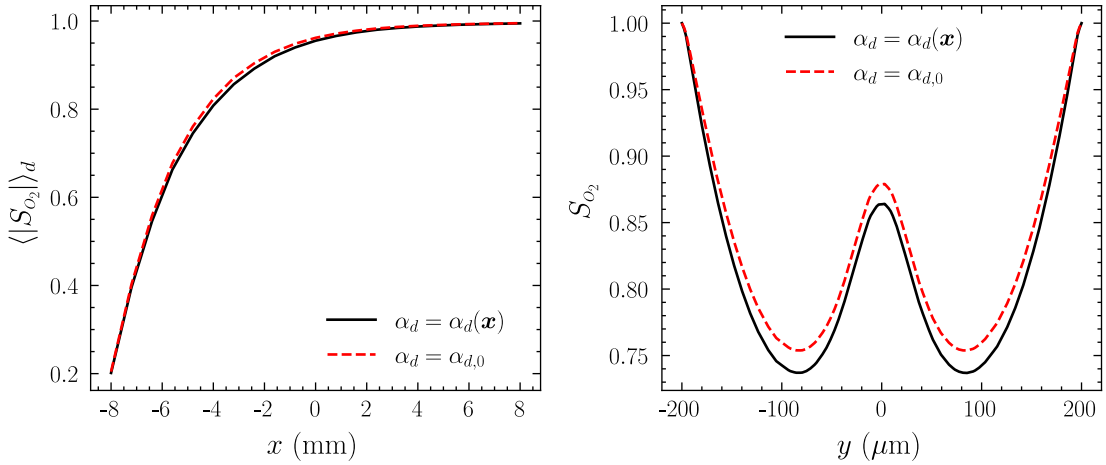

(a) Dispersed phase mass flow rate averaged oxygen saturation.

(b) Saturation profiles at $x = -4\,\mathrm{mm}$.

Figure 9.16: The oxygen saturation behaviour for **variable** and **uniform** dispersed phase volume fraction fields in the semi-cyclic two-dimensional oxygenator domain.

The dispersed phase mass flow rate averaged oxygen saturation profiles for both the variable and uniform dispersed phase volume fraction fields, depicted in figure 9.16a, show a maximum difference of 1.56%. The migratory behaviour of whole blood and observed cell-depleted boundary layers in figure 9.14 thus do not appear to have a significant influence on the oxygenation of whole blood. The saturation profiles considered between the cyclic slices depicted in figure 9.16b show that the differences in saturation are mainly found within the high-velocity regions of the flow. A slightly elevated dispersed phase volume fraction was also observed in this region, as depicted in figure 9.13a. The oxygenation then appears primarily restricted by the bulk value of the dispersed phase volume fraction rather than the cell depletion layer near the fibres.

9.6 The influence of Newtonian Rheology and Particle Presence on Oxygenation in a Two-Dimensional Oxygenator

The migration of red blood cells within whole blood discussed in the preceding sections was not the sole blood flow modelling considered in this study. Additionally, the non-Newtonian rheology of the fluid was also considered and the presence of the blood cells by means of a nonzero volume fraction. In this section the influence of these two modelling consideration is discussed.

9.6.1 The Influence of Newtonian Rheology

The non-Newtonian rheology of whole blood was primarily characterized by its shear-thinning behaviour and modelled an increased dissipation rate due to the interphasic interactions. A Newtonian consideration replaced this non-Newtonian consideration with a straightforward phasic averaged mixture viscosity to study its influence,

$$\mu_m = (1 - \alpha_{d,0})\overline{\overline{\mu}}_c + \alpha_{d,0}\overline{\overline{\mu}}_d. \tag{9.2}$$

Where the viscosities correspond to those discussed in section 2.2.3, such that the constant mixture viscosity equates to $\mu_m = 3.336 \times 10^{-3}\,\mathrm{Pa}\cdot\mathrm{s}$. The comparison of the mass flow rate averaged saturation behaviour of the Newtonian, and non-Newtonian solutions is depicted in figure 9.17a.

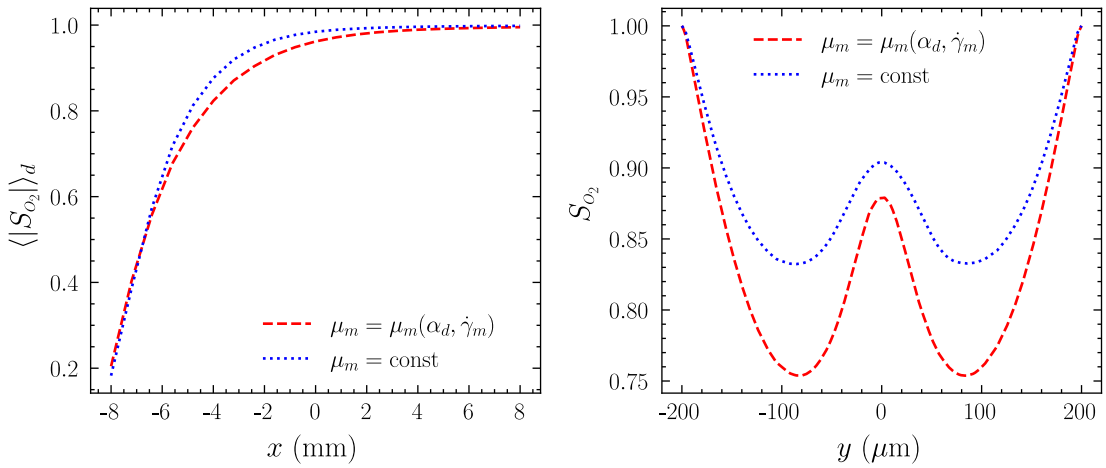

(a) Dispersed phase mass flow rate averaged oxygen saturation.

(b) Saturation profiles at $x = -4\,\mathrm{mm}$.

Figure 9.17: The oxygen saturation behaviour for **non-Newtonian** and **Newtonian** viscosity modelling in the semi cyclic two-dimensional oxygenator domain. The **non-Newtonian** consideration is congruent with the consideration of figure 9.16a and the constant **Newtonian** viscosity was taken as $\mu_m = 3.336 \times 10^{-3}\,\mathrm{Pa}\cdot\mathrm{s}$.

The numerical results for the dispersed phase mass flow rate averaged saturation for the differing rheological considerations of whole blood are depicted in figure 9.17a and show a maximum difference of 5.29%. The Newtonian saturation profile, depicted in figure 9.17b, shows a more evenly distribution of the oxygen saturation with differences up to about 9% compared to the non-Newtonian profile. These differences indicate that interphasic momentum interactions have a non-negligible impact on the oxygenation of whole blood, and blood flow cannot simply be taken Newtonian.
While the employed viscosity model accounts for the interphasic interactions of individual blood cells, it is essential to note that the parametric fitting also included the influence of blood cell aggregation. The aggregation of blood cells is, however, not observed in oxygenators. The influence of the aggregation on the viscosity model is most dominant in the regions of low shear and, thus, also in the regions where the primary differences in oxygenation are observed. The exact influence of this consideration was, however, not studied here.

9.6.2 The Influence of the Presence of Red Blood Cells

In addition to the complicated rheology, the influence of the actual presence of particles for non-migrating whole blood was studied. The exclusion of the particles is modelled by setting the dispersed phase volume fraction to zero, $\alpha_{d,0} = 0$. The limiting behaviour and its influence on the oxygenation model are discussed in appendix A.8, and the numerical results for the semi-cyclic two-dimensional oxygenator domain are depicted in figure 9.18.

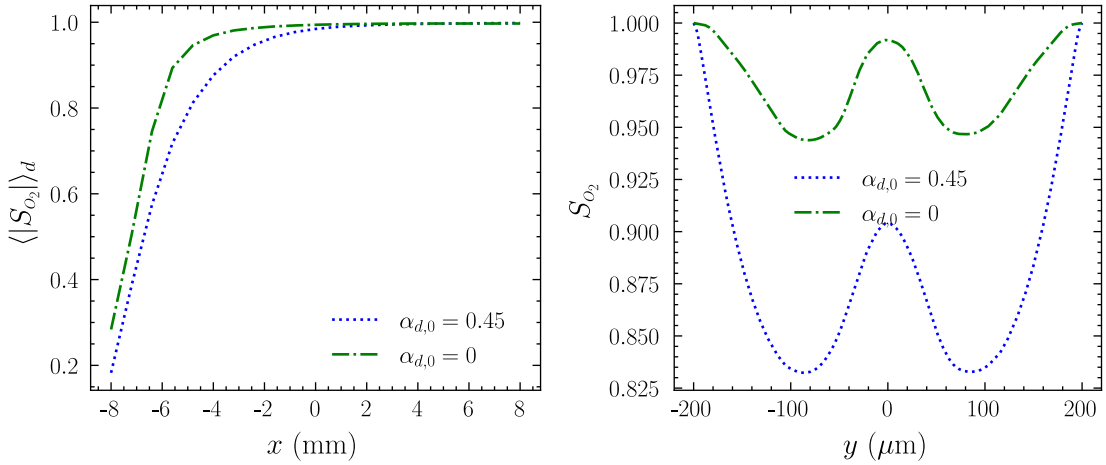

(a) Dispersed phase mass flow rate averaged oxygen saturation.

(b) Saturation profiles at $x = -4\,\text{mm}$.

Figure 9.18: The mass flow rate averaged saturation for **particle-laden** and **non-particulate** Newtonian modelling of whole blood. The **particle-laden** consideration is congruent with the consideration of figure 9.17a.

The numerical results for the dispersed phase mass flow rate averaged saturation for the influence of the presence of the red blood cells are depicted in figure 9.18a and show a maximum difference of 17.65%. The negligence of red blood cells thus greatly impacts the oxygenation and observed performance of an oxygenator. Due to the lack of blood cells, all oxygen is allowed to diffuse into the whole domain without the artificial uptake of the oxygen, causing an overall higher saturation throughout the domain as also depicted in figure 9.18b.

9.7 Validity and Limitations of the Chosen Models

This study considered several models to model fluid flow and mass transfer in a hollow-fibre membrane oxygenator. In this section, the validity of the assumptions required in order to allow the consideration of these models and the comparison between oxygenation models is discussed.

9.7.1 The Mixture Formulation Consideration of Whole Blood

The mixture model formulation was considered in this study based on the laminar Stokesian suspension character and the typical dense dispersion of the red blood cells in whole blood, as discussed in chapters 4 and 2. The applicability of the Stokesian suspension character was primarily determined by the typical Stokes and particulate Reynolds numbers denoted in equation 4.5 and 4.4. In consideration of non-Newtonian migratory blood

flow modelling in the semi-cyclic two-dimensional oxygenator domain, discussed in section 9.5.3, these numbers equate to $\mathrm{Re}_p = 9.22 \times 10^{-3}$ and $\mathrm{St} = 7.28 \times 10^{-4}$. Since both conditions $\mathrm{Re}_p \ll 1$ and $\mathrm{St} \ll 1$ hold for the domain and flow types considered in this study, the consideration of the mixture model appears appropriate.

9.7.2 Comparative Study of Oxygen Transport Governed by Mixture Formulation Oxygenation Models

The oxygenation behaviour of the newly derived conservation of the total mass of the oxygen model can be compared to that of the commonly considered effective oxygen diffusivity model. The comparison of the oxygen partial pressure and saturation results of non-migratory whole blood in pipe flow are presented in figure 9.19.

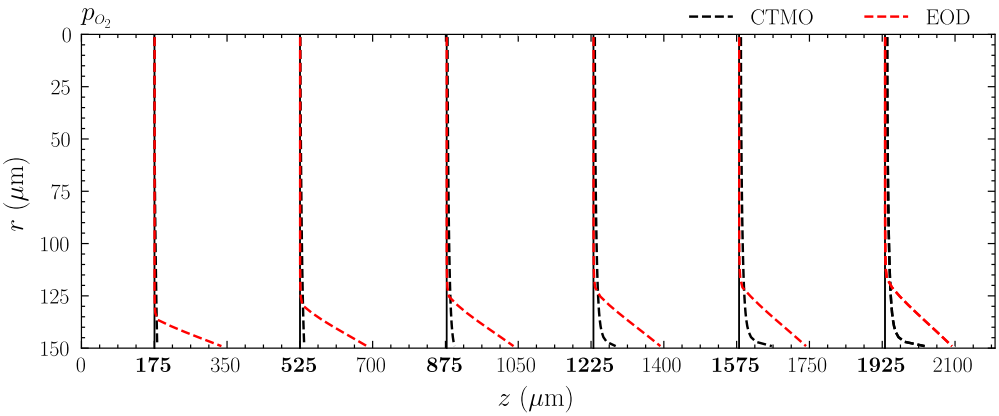

(a) Oxygen partial pressure.

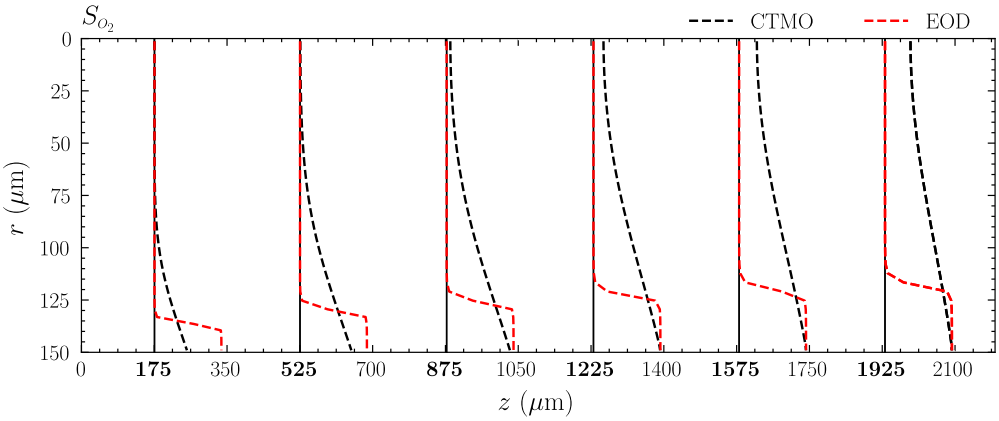

(b) Oxygen saturation.

Figure 9.19: Oxygen partial pressure and saturation profile development beyond the entrance region for the **CTMO** and **EOD** oxygenation models. The **CTMO** model results are congruent with uniform dispersed phase volume fraction results considered in figure 9.8.

The oxygen saturation results depicted in figure 9.19 indicate that the CTMO model overestimates the oxygen saturation compared to the EOD. This overestimation is purely rooted in how both models treat the oxygen uptake by the red blood cells. The EOD model can be observed to block the transport of oxygen entirely through the unsaturated

red blood cells. I.e. whenever the transported oxygen comes in contact with non-fully saturated blood cells, the oxygen is entirely bounded locally. The CTMO model treats the oxygen uptake as a local sink term and allows oxygen transport throughout the entire domain.
The difference in the uptake behaviour is additionally evident from the partial pressure profile comparison. The CTMO model shows a gradual increase of oxygen concentration throughout the entire domain and only approaches the high wall concentration once the wall-adjacent blood cells are fully saturated. The EOD model, in contrast, shows behaviour equivalent to simple steady-state diffusion up to the non-fully saturated blood cells.
The overestimation of the oxygen uptake in the CTMO model indicates the importance of the consideration of membrane resistances. The resistance was in the derivation of the model and, in this study, as a first guess, assumed negligible such that the dissolved oxygen concentrations of both phases could be taken equivalent. While the direct interphasic oxygen transport cannot be considered in a mixture model formulation, the transport is considered in the constitutive modelling of the oxyhaemoglobin discussed in appendix A.4. The oxygen saturation in this regard was modelled using the mixture oxygen partial pressure, while a more appropriate choice would be the partial pressure of the oxygen in the dispersed phase as considered by the micro-scale model discussed in section 7.3.2. This consideration would then require a constitutive model that relates the mixture partial pressure and the dispersed phase dissolved partial pressure, which should include the interphasic oxygen transport.

Chapter 10

Conclusions and Recommendations

The influence of shear-induced particle migration of red blood cells and non-Newtonian rheology of whole blood on the oxygenation of whole blood were studied in this thesis. The particle migration was modelled through the commonly considered phenomenological diffusive flux model, the rheology through a phase-averaged consideration of the Yeleswarapu-Wu model, and the oxygenation model was newly derived for this study in appendix A.

Firstly, the influence of the migration on oxygenation was reviewed for blood flow in an axisymmetric pipe. The migration typically caused a concentration of red blood cells near the central line of the pipe flow and a reduction near the wall compared to the mean concentration. The observed profiles for the oxygen partial pressure and saturation were found to differ most in the entrance region of the pipe. The exclusion of the particle migration delayed the overall oxygenation behaviour due to the more considerable resistance to oxygen transport caused by the higher concentration of particles at the wall. Once the near-wall particles were saturated, the oxygen partial pressure and saturation profiles were observed to become equivalent. In this region, the saturation of whole blood, including the migratory behaviour, exhibited a slightly lower saturation caused by the red blood cell concentration near the central line of the pipe. The lower saturation in this region was observed to be the primary difference between the migratory and non-migratory whole blood considerations. The maximum mean saturation differences were up to about 12% over-estimation due to the exclusion of particle migration.
However, these differences in the mean saturation were not observed to such a degree for the consideration of the shear-induced migration in a two-dimensional oxygenator domain. In the considered oxygenator, the maximum difference was observed to be 1.56%. The bulk behaviour of the particle migration in the oxygenator introduces the equivalence of the mean saturation for both cases. While significant particle concentration differences were observed locally adjacent to the fibres, the bulk particle concentration remained uniform at a slightly elevated value when particle migration was considered.
Additionally, the influence of the non-Newtonian rheology of whole blood on oxygenation was studied for the non-migratory modelling consideration. In pipe flow, the primary influence of the non-Newtonian viscosity modelling was a blunted velocity profile compared to the typical parabolic profile observed in Newtonian flows. The primary influence for observing this profile was the shear rate magnitude dependence of the viscosity model. The influence of the non-Newtonian viscosity in the two-dimensional oxygenator domain on the oxygen saturation showed local differences up to about 9%. This difference suggests

the non-Newtonian character of whole blood and its influence on oxygen transport is not as easily dismissed. However, the parametric fitting considered for the utilized viscosity model also included an influence of red blood cell aggregation into rouleaux, which is not observed inside oxygenators. The additional influence of this consideration is unknown, and further research should identify if the non-Newtonian behaviour is truly inadmissible for the oxygenation of whole blood.
Furthermore, the influence of the presence of red blood cells on oxygenation was studied for the non-migratory modelling consideration. The non-consideration of the particles was observed to influence the oxygenation of whole blood significantly. The exclusion of the oxygen-absorbing particles resulted in a quickly increasing oxygen content of the fluid and, therefore, a significant overestimation of saturation levels.
Lastly, the oxygen transport modelled by the newly derived conservation of the total mass of oxygen model, CTMO, was compared to that of the commonly considered effective oxygen diffusivity model, EOD. The CTMO model effectively considered the oxygen uptake by the red blood cells as a sink term, allowing the oxygen to transport through the entire domain. The EOD model, in contrast, exhibited a blockage of oxygen transport once non-fully saturated blood cells were reached. The CTMO model did show a saturation overestimation compared to the EOD model, caused by the exclusion of the interphasic transport of oxygen. As a first guess, in this study, the oxygen dissolved in the blood plasma and the cytoplasm were taken equivalent. The overestimating nature of the model then elucidates the importance of membrane resistance to oxygen uptake, and its modelling requires further research to improve the accuracy of the model.

Bibliography

[1] F. A. Amiri and J. Zhang. "Oxygen Transport across Tank-Treading Red Blood Cell: Individual and Joint Roles of Flow Convection and Oxygen-Hemoglobin Reaction". In: *Microvascular Research* (Jan. 2023). DOI: 10.1016/j.mvr.2022.104447.

[2] A. J. Apostolidis and A. N. Beris. "Modeling of the Blood Rheology in Steady-State Shear Flows". In: *Journal of Rheology* 58.3 (May 2014), pp. 607–633. DOI: 10.1122/1.4866296.

[3] M. Armstrong and J. Tussing. "A methodology for adding thixotropy to Oldroyd-8 family of viscoelastic models for characterization of human blood". In: *Physics of Fluids* 32.9 (Sept. 2020), p. 094111. DOI: 10.1063/5.0022501.

[4] A. Balachandran Nair, S. Pirker, and M. Saeedipour. "Resolved CFD-DEM Simulation of Blood Flow with a Reduced-Order RBC Model". In: *Computational Particle Mechanics* 9.4 (July 2022), pp. 759–774. DOI: 10.1007/s40571-021-00441-x.

[5] J. M. Baldwin. "A Model of Co-operative Oxygen Binding to Haemoglobin". In: *British Medical Bulletin* 32.3 (Sept. 1976), pp. 213–218. DOI: 10.1093/oxfordjournals.bmb.a071365.

[6] J. H. Barbee and G. R. Cokelet. "The Fahraeus effect". In: *Microvascular Research* 3.1 (Jan. 1971), pp. 6–16. DOI: 10.1016/0026-2862(71)90002-1.

[7] R. G. Bardón et al. "Haematocrit heterogeneity in blood flows past microfluidic models of oxygenating fibre bundles". In: *Medical Engineering and Physics* 73 (Nov. 2019), pp. 30–38. DOI: 10.1016/j.medengphy.2019.07.012.

[8] H. A. Barnes. *A Handbook of Elementary Rheology*. Aberystwyth: University of Wales Institute of Non-Newtonian Fluid Mechanics, 2000. 200 pp. ISBN: 978-0-9538032-0-0.

[9] J. Beaucourt, T. Biben, and C. Misbah. "Optimal Lift Force on Vesicles near a Compressible Substrate". In: *Europhysics Letters (EPL)* 67.4 (Aug. 2004), pp. 676–682. DOI: 10.1209/epl/i2004-10103-0.

[10] C. Beisbart and N. J. Saam, eds. *Computer Simulation Validation: Fundamental Concepts, Methodological Frameworks, and Philosophical Perspectives*. Simulation Foundations, Methods and Applications. Cham: Springer International Publishing, 2019. ISBN: 978-3-319-70765-5.

[11] A. N. Beris et al. "Recent Advances in Blood Rheology: A Review". In: *Soft Matter* 17.47 (2021), pp. 10591–10613. DOI: 10.1039/D1SM01212F.

[12] R. B. Bird, W. E. Stewart, and E. N. Lightfoot. *Transport Phenomena*. Brisbane, QLD, Australia: John Wiley and Sons (WIE), Jan. 1966. ISBN: 9780470115398.

[13] J. A. Boure. "Wave phenomena and one-dimensional two-phase flow models". In: *Multiphase Science and Technology* 9.1 (1997), pp. 63–107. DOI: 10.1615/multscientechn.v9.i1.30.

[14] E. Boyle and M. Massoudi. "A Theory for Granular Materials Exhibiting Normal Stress Effects Based on Enskog's Dense Gas Theory". In: *International Journal of Engineering Science* 28.12 (Jan. 1990), pp. 1261–1275. DOI: 10.1016/0020-7225(90)90074-S.

[15] E. Breitbarth et al. "The Bunsen Gas Solubility Coefficient of Ethylene as a Function of Temperature and Salinity and Its Importance for Nitrogen Fixation Assays". In: *Limnology and Oceanography: Methods* 2.8 (Aug. 2004), pp. 282–288. DOI: 10.4319/lom.2004.2.282.

[16] F. P. Bretherton. "The Motion of Rigid Particles in a Shear Flow at Low Reynolds Number". In: *Journal of Fluid Mechanics* 14.2 (Oct. 1962), pp. 284–304. DOI: 10.1017/S002211206200124X.

[17] M. Brust et al. "The plasma protein fibrinogen stabilizes clusters of red blood cells in microcapillary flows". In: *Sci. Rep.* 4.1 (Mar. 2014). DOI: https://doi.org/10.1038/srep04348.

[18] M. Brust et al. "Rheology of Human Blood Plasma: Viscoelastic Versus Newtonian Behavior". In: *Physical Review Letters* 110.7 (Feb. 15, 2013), p. 078305. DOI: 10.1103/PhysRevLett.110.078305.

[19] A. Buess et al. "Modeling of the Transport and Exchange of a Gas Species in Lungs With an Asymmetric Branching Pattern. Application to Nitric Oxide". In: *Frontiers in Physiology* 11 (Dec. 10, 2020), p. 570015. DOI: 10.3389/fphys.2020.570015.

[20] Y. Çengel and J. Cimbala. *Fluid Mechanics: Fundamentals and Applications*. McGraw-Hill Education, 2018. ISBN: 9781259921902.

[21] Y. Çengel and A. Ghajar. *Heat and Mass Transfer: Fundamentals & Applications*. McGraw-Hill Education, 2020. ISBN: 9789813158962.

[22] K. Chandran et al. "Numerical Simulation of Blood Flow Modeled as a Fluid-Particulate Mixture". In: *Journal of Non-Newtonian Fluid Mechanics* 285 (Nov. 2020), p. 104383. DOI: 10.1016/j.jnnfm.2020.104383.

[23] A. Clark et al. "Oxygen Delivery from Red Cells". In: *Biophysical Journal* 47.2 (Feb. 1985), pp. 171–181. DOI: 10.1016/S0006-3495(85)83890-X.

[24] L. H. Cohn and D. H. Adams. *Cardiac Surgery in the Adult*. 5th edition. New York: McGraw Hill Education, 2018. ISBN: 978-0-07-184602-8.

[25] G. Coupier et al. "Noninertial Lateral Migration of Vesicles in Bounded Poiseuille Flow". In: *Physics of Fluids* 20.11 (Nov. 1, 2008), p. 111702. DOI: 10.1063/1.3023159.

[26] M. Darzi and C. Park. "Experimental Visualization and Numerical Simulation of Liquid-Gas Two-Phase Flows in a Horizontal Pipe". In: *Volume 7: Fluids Engineering*. ASME 2017 International Mechanical Engineering Congress and Exposition. Tampa, Florida, USA: American Society of Mechanical Engineers, Nov. 3, 2017, V007T09A011. DOI: 10.1115/IMECE2017-72113.

[27] R. Dezube. *Exchanging oxygen and carbon dioxide - lung and airway disorders*. Jan. 2023. URL: https://www.msdmanuals.com/home/lung-and-airway-disorders/biology-of-the-lungs-and-airways/exchanging-oxygen-and-carbon-dioxide.

[28] I. Drijer. "Simulation of Shear Induced Diffusion Based Separation Processes". PhD thesis. Wageningen University, Oct. 10, 2018. DOI: 10.18174/452178.

[29] P. Ecker et al. “Microstructured Hollow Fiber Membranes: Potential Fiber Shapes for Extracorporeal Membrane Oxygenators”. In: *Membranes* 11.5 (May 20, 2021), p. 374. DOI: 10.3390/membranes11050374.

[30] A. Einstein. “Eine neue Bestimmung der Moleküldimensionen”. In: *Annalen der Physik* 324.2 (1906), pp. 289–306. DOI: 10.1002/andp.19063240204.

[31] S. Evje and T. Flåtten. “On the Wave Structure of Two-Phase Flow Models”. In: *SIAM Journal on Applied Mathematics* 67.2 (Jan. 2007), pp. 487–511. DOI: 10.1137/050633482.

[32] R. Fåhraeus. “The Suspension Stability of The Blood”. In: *Physiological Reviews* 9.2 (Apr. 1929), pp. 241–274. DOI: 10.1152/physrev.1929.9.2.241.

[33] A. Farina, F. Rosso, and A. Fasano. “A continuum mechanics model for the Fåhræus-Lindqvist effect”. In: *Journal of Biological Physics* 47.3 (July 2021), pp. 253–270. DOI: 10.1007/s10867-021-09575-8.

[34] A. Farutin and C. Misbah. “Symmetry Breaking and Cross-Streamline Migration of Three-Dimensional Vesicles in an Axial Poiseuille Flow”. In: *Physical Review E* 89.4 (Apr. 18, 2014), p. 042709. DOI: 10.1103/PhysRevE.89.042709.

[35] M. Gad-el-Hak. “Questions in Fluid Mechanics: Stokes’ Hypothesis for a Newtonian, Isotropic Fluid”. In: *Journal of Fluids Engineering* 117.1 (Mar. 1, 1995), pp. 3–5. DOI: 10.1115/1.2816816.

[36] F. Gadala-Maria and A. Acrivos. “Shear-Induced Structure in a Concentrated Suspension of Solid Spheres”. In: *Journal of Rheology* 24.6 (Dec. 1980), pp. 799–814. DOI: 10.1122/1.549584.

[37] X. Grandchamp et al. “Lift and Down-Gradient Shear-Induced Diffusion in Red Blood Cell Suspensions”. In: *Physical Review Letters* 110.10 (Mar. 5, 2013), p. 108101. DOI: 10.1103/PhysRevLett.110.108101.

[38] C. Greenshields and H. Weller. *Notes on Computational Fluid Dynamics: General Principles*. Reading, UK: CFD Direct Ltd, 2022. ISBN: 978-1-3999-2078-0.

[39] S. E. Harding. “Intrinsic Viscosity”. In: *Encyclopedia of Biophysics*. Springer Berlin Heidelberg, 2013, pp. 1123–1129. DOI: 10.1007/978-3-642-16712-6_283.

[40] D. S. Hariprasad and T. W. Secomb. “Motion of Red Blood Cells near Microvessel Walls: Effects of a Porous Wall Layer”. In: *Journal of Fluid Mechanics* 705 (Aug. 25, 2012), pp. 195–212. DOI: 10.1017/jfm.2012.102.

[41] R. G. Henríquez Rivera, X. Zhang, and M. D. Graham. “Mechanistic Theory of Margination and Flow-Induced Segregation in Confined Multicomponent Suspensions: Simple Shear and Poiseuille Flows”. In: *Physical Review Fluids* 1.6 (Oct. 18, 2016), p. 060501. DOI: 10.1103/PhysRevFluids.1.060501.

[42] F. Hesselmann et al. “Structure-Dependent Gas Transfer Performance of 3D-membranes for Artificial Membrane Lungs”. In: *Journal of Membrane Science* 634 (Sept. 2021), p. 119371. DOI: 10.1016/j.memsci.2021.119371.

[43] T. Holzmann. *Mathematics, Numerics, Derivations and OpenFOAM(R)*. Release 7.0. Holzmann CFD, 2023. DOI: 10.13140/RG.2.2.27193.36960.

[44] M. Hormes. *CFD-basierte Modellbildung und Validierung des Gastransfers zur Analyse der Blutoxygenierung über Hohlfasermembranen*. Aachener Beiträge zur Medizintechnik 6. Aachen: Shaker, 2011. ISBN: 978-3-8440-0062-7.

[45] M. Hormes et al. “A validated CFD model to predict O2 and CO2 transfer within hollow fiber membrane oxygenators”. In: *The International Journal of Artificial Organs* 34.3 (Mar. 2011), pp. 317–325. DOI: 10.5301/ijao.2011.6494.

[46] J. S. Horner et al. “Measurements of human blood viscoelasticity and thixotropy under steady and transient shear and constitutive modeling thereof”. In: *Journal of Rheology* 63.5 (Sept. 2019), pp. 799–813. DOI: 10.1122/1.5108737.

[47] V. H. Huxley and H. Kutchai. “Effect of Diffusion Boundary Layers on the Initial Uptake of O2 by Red Cells. Theory versus Experiment”. In: *Microvascular Research* 26.1 (July 1983), pp. 89–107. DOI: 10.1016/0026-2862(83)90058-4.

[48] M. Ishii and T. Hibiki. *Thermo-Fluid Dynamics of Two-Phase Flow*. Springer New York, 2011. DOI: 10.1007/978-1-4419-7985-8.

[49] H. Iwahashi, K. Yuri, and Y. Nosé. “Development of the Oxygenator: Past, Present, and Future”. In: *Journal of Artificial Organs* 7.3 (Sept. 2004), pp. 111–120. DOI: 10.1007/s10047-004-0268-6.

[50] A. Kaesler et al. “Computational Modeling of Oxygen Transfer in Artificial Lungs”. In: *Artificial Organs* 42.8 (July 2018), pp. 786–799. DOI: 10.1111/aor.13146.

[51] A. Kaesler et al. “How Computational Modeling can Help to Predict Gas Transfer in Artificial Lungs Early in the Design Process”. In: *ASAIO Journal* 66.6 (Nov. 2019), pp. 683–690. DOI: 10.1097/mat.0000000000001098.

[52] B. Kaoui et al. “Lateral Migration of a Two-Dimensional Vesicle in Unbounded Poiseuille Flow”. In: *Physical Review E* 77.2 (Feb. 5, 2008), p. 021903. DOI: 10.1103/PhysRevE.77.021903.

[53] J. Kim, J. F. Antaki, and M. Massoudi. “Computational Study of Blood Flow in Microchannels”. In: *Journal of Computational and Applied Mathematics* 292 (Jan. 2016), pp. 174–187. DOI: 10.1016/j.cam.2015.06.017.

[54] M. Kopernik et al. “Discrete Phase Model of Blood Flow in a Roughness Microchannel Simulating the Formation of Pseudointima”. In: *Acta of Bioengineering and Biomechanics* 24.1 (2022). DOI: 10.37190/ABB-01989-2021-02.

[55] C. V. Kulkarni et al. “Pressure Effects on a Protein–Lipid Model Membrane”. In: *Soft Matter* 9.28 (2013), p. 6525. DOI: 10.1039/c3sm50911g.

[56] R. S. Lakes. *Viscoelastic Materials*. Cambridge: Cambridge University Press, 2009. 461 pp. ISBN: 978-0-521-88568-3.

[57] L. Lanotte et al. “Red Cells’ Dynamic Morphologies Govern Blood Shear Thinning under Microcirculatory Flow Conditions”. In: *Proceedings of the National Academy of Sciences* 113.47 (Nov. 22, 2016), pp. 13289–13294. DOI: 10.1073/pnas.1608074113.

[58] D. Leighton and A. Acrivos. “The Shear-Induced Migration of Particles in Concentrated Suspensions”. In: *Journal of Fluid Mechanics* 181 (Sept. 1987), p. 415. DOI: 10.1017/S0022112087002155.

[59] S. Losserand, G. Coupier, and T. Podgorski. “Axial Dispersion of Red Blood Cells in Microchannels”. In: *Physical Review Fluids* 8.4 (Apr. 6, 2023), p. 043102. DOI: 10.1103/PhysRevFluids.8.043102.

[60] A. R. Malipeddi and K. Sarkar. “Shear-Induced Gradient Diffusivity of a Red Blood Cell Suspension: Effects of Cell Dynamics from Tumbling to Tank-Treading”. In: *Soft Matter* 17.37 (2021), pp. 8523–8535. DOI: 10.1039/D1SM00938A.

[61] M. Manninen, V. Taivassalo, and S. Kallio. “On the Mixture Model for Multiphase Flow”. In: ().

[62] M. Massoudi. “An Anisotropic Constitutive Relation for the Stress Tensor of a Rod-like (Fibrous-Type) Granular Material”. In: *Mathematical Problems in Engineering* 2005.6 (2005), pp. 679–702. DOI: 10.1155/MPE.2005.679.

[63] M. Massoudi. “On the flow of granular materials with variable material properties”. In: *International Journal of Non-Linear Mechanics* 36.1 (2001), pp. 25–37. DOI: https://doi.org/10.1016/S0020-7462(99)00085-2.

[64] M. Massoudi and J. F. Antaki. “An Anisotropic Constitutive Equation for the Stress Tensor of Blood Based on Mixture Theory”. In: *Mathematical Problems in Engineering* 2008 (2008), pp. 1–30. DOI: 10.1155/2008/579172.

[65] M. Massoudi, J. Kim, and J. F. Antaki. “Modeling and Numerical Simulation of Blood Flow Using the Theory of Interacting Continua”. In: *International Journal of Non-Linear Mechanics* 47.5 (June 2012), pp. 506–520. DOI: 10.1016/j.ijnonlinmec.2011.09.025.

[66] Jp. Matas, Jf. Morris, and E. Guazzelli. “Lateral Forces on a Sphere”. In: *Oil & Gas Science and Technology* 59.1 (Jan. 2004), pp. 59–70. DOI: 10.2516/ogst:2004006.

[67] J. Mauer et al. “Flow-Induced Transitions of Red Blood Cell Shapes under Shear”. In: *Physical Review Letters* 121.11 (Sept. 11, 2018), p. 118103. DOI: 10.1103/PhysRevLett.121.118103.

[68] “Mechanism of the Production of Small Eddies from Large Ones”. In: *Proceedings of the Royal Society of London. Series A - Mathematical and Physical Sciences* 158.895 (Feb. 3, 1937), pp. 499–521. DOI: 10.1098/rspa.1937.0036.

[69] *Modeling Approaches and Computational Methods for Particle-Laden Turbulent Flows*. Elsevier, 2023. ISBN: 978-0-323-90133-8.

[70] C. Morel. *Mathematical modeling of disperse two-phase flows*. en. 1st ed. Fluid Mechanics and Its Applications. Basel, Switzerland: Springer International Publishing, July 2015. ISBN: 978-3-319-20103-0.

[71] J. F. Morris and F. Boulay. “Curvilinear Flows of Noncolloidal Suspensions: The Role of Normal Stresses”. In: *Journal of Rheology* 43.5 (Sept. 1, 1999), pp. 1213–1237. DOI: 10.1122/1.551021.

[72] F. Municchi, P. P. Nagrani, and I. C. Christov. “A Two-Fluid Model for Numerical Simulation of Shear-Dominated Suspension Flows”. In: *International Journal of Multiphase Flow* 120 (Nov. 2019), p. 103079. DOI: 10.1016/j.ijmultiphaseflow.2019.07.015.

[73] S. T. Munkejord. “Analysis of the two-fluid model and the drift-flux model for numerical calculation of two-phase flow”. PhD thesis. Norwegian University of Science and Technology, 2006. ISBN: 82-471-7338-7.

[74] National Center for Biotechnology Information. *PubChem Compound Summary for CID 977, Oxygen*. https://pubchem.ncbi.nlm.nih.gov/compound/Oxygen. Retrieved November 17, 2023. 2023.

[75] T. Nierhaus. “Modeling and simulation of dispersed two-phase flow transport phenomena in electrochemical processes”. PhD thesis. Aachen, 2009, XXII, 172 S. : Ill., graph. Darst. URL: https://publications.rwth-aachen.de/record/51363.

[76] N. Norouzi, H. C. Bhakta, and W. H. Grover. "Sorting Cells by Their Density". In: *PLOS ONE* 12.7 (July 19, 2017). Ed. by V. M. Ugaz, e0180520. DOI: 10.1371/journal.pone.0180520.

[77] P. R. Nott and J. F. Brady. "Pressure-Driven Flow of Suspensions: Simulation and Theory". In: *Journal of Fluid Mechanics* 275 (Sept. 25, 1994), pp. 157–199. DOI: 10.1017/S0022112094002326.

[78] P. R. Nott, E. Guazzelli, and O. Pouliquen. "The Suspension Balance Model Revisited". In: *Physics of Fluids* 23.4 (Apr. 1, 2011), p. 043304. DOI: 10.1063/1.3570921.

[79] W. L. Oberkampf, T. G. Trucano, and C. Hirsch. "Verification, validation, and predictive capability in computational engineering and physics". In: *Applied Mechanics Reviews* 57.5 (Sept. 2004), pp. 345–384. DOI: 10.1115/1.1767847.

[80] M. I. W. Paper. *A Basic Introduction to Rheology*. Tech. rep. 2016. URL: https://cdn.technologynetworks.com/TN/Resources/PDF/WP160620BasicIntroRheology.pdf.

[81] N. Phan-Thien. *Understanding Viscoelasticity: An Introduction to Rheology*. Graduate Texts in Physics. Berlin, Heidelberg: Springer Berlin Heidelberg, 2013. ISBN: 978-3-642-32957-9.

[82] R. J. Phillips et al. "A Constitutive Equation for Concentrated Suspensions That Accounts for Shear-induced Particle Migration". In: *Physics of Fluids A: Fluid Dynamics* 4.1 (Jan. 1992), pp. 30–40. DOI: 10.1063/1.858498.

[83] A. Pincot and M. Armstrong. "Novel Tensorial Thixo-Visco-Plastic Framework for Rheological Characterization of Human Blood". In: *Scientific Reports* 11.1 (Nov. 9, 2021), p. 22004. DOI: 10.1038/s41598-021-01362-8.

[84] T. Poinsot and D. Veynante. *Theoretical and Numerical Combustion*. 2nd ed. Philadelphia: Edwards, 2005. 522 pp. ISBN: 978-1-930217-10-2.

[85] J. Poiseuille. "Observations of Blood Flow". In: *Annales des Sciences Naturelles* 5 (1836), pp. 111–115.

[86] A. R. Pries, D. Neuhaus, and P. Gaehtgens. "Blood Viscosity in Tube Flow: Dependence on Diameter and Hematocrit". In: *American Journal of Physiology-Heart and Circulatory Physiology* 263.6 (Dec. 1, 1992), H1770–H1778. DOI: 10.1152/ajpheart.1992.263.6.H1770.

[87] K. R. Rajagopal and A. S. Wineman. "Flow of Electro-Rheological Materials". In: *Acta Mechanica* 91.1-2 (Mar. 1992), pp. 57–75. DOI: 10.1007/BF01194033.

[88] A. Ramachandran and D. T. Leighton. "The Influence of Secondary Flows Induced by Normal Stress Differences on the Shear-Induced Migration of Particles in Concentrated Suspensions". In: *Journal of Fluid Mechanics* 603 (May 25, 2008), pp. 207–243. DOI: 10.1017/S0022112008000980.

[89] T. Rodrigues, F. Galindo-Rosales, and L. Campo-Deaño. "Haemodynamics around confined microscopic cylinders". In: *Journal of Non-Newtonian Fluid Mechanics* 286 (Dec. 2020), p. 104406. DOI: 10.1016/j.jnnfm.2020.104406.

[90] T. Rodrigues et al. "Understanding the complex rheology of human blood plasma". In: *Journal of Rheology* 66.4 (July 2022), pp. 761–774. DOI: 10.1122/8.0000442.

[91] M. Sarkar and V. Prabhu. "Basics of Cardiopulmonary Bypass". In: *Indian Journal of Anaesthesia* 61.9 (2017), p. 760. DOI: 10.4103/ija.IJA_379_17.

[92] T. Schenkel and I. Halliday. "Continuum Scale Non Newtonian Particle Transport Model for Hæmorheology". In: *Mathematics* 9.17 (Aug. 30, 2021), p. 2100. DOI: 10.3390/math9172100.

[93] P. C. Schlanstein. "Experimental and Numerical Investigations of Anisotropic Permeabilities in Blood Oxygenators". PhD thesis. Rheinisch-Westfälischen Technischen Hochschule Aachen, 2019.

[94] G. A. Schmidt, ed. *Extracorporeal Membrane Oxygenation for Adults*. Respiratory Medicine. Cham: Springer International Publishing, 2022. ISBN: 978-3-031-05298-9.

[95] T. W. Secomb. "Blood Flow in the Microcirculation". In: *Annual Review of Fluid Mechanics* 49.1 (Jan. 2017), pp. 443–461. DOI: 10.1146/annurev-fluid-010816-060302.

[96] G. Segré and A. Silberberg. "Behaviour of Macroscopic Rigid Spheres in Poiseuille Flow Part 2. Experimental Results and Interpretation". In: *Journal of Fluid Mechanics* 14.1 (Sept. 1962), pp. 136–157. DOI: 10.1017/S0022112062001111.

[97] K. R. Sharma. *Transport Phenomena in Biomedical Engineering: Artificial Organ Design and Development and Tissue Engineering*. New York: McGraw-Hill, 2010. ISBN: 978-0-07-166398-4.

[98] Z. Shen et al. "Inversion of Hematocrit Partition at Microfluidic Bifurcations". In: *Microvascular Research* 105 (May 2016), pp. 40–46. DOI: 10.1016/j.mvr.2015.12.009.

[99] O. Siggaard-Andersen et al. "Measured and derived quantities with modern pH and blood gas equipment: Calculation algorithms with 54 equations". In: *Scandinavian Journal of Clinical and Laboratory Investigation* 48.sup189 (Jan. 1988), pp. 7–15. DOI: 10.1080/00365518809168181.

[100] M. Sommerfeld. "Numerical Methods for Dispersed Multiphase Flows". In: *Particles in Flows*. Ed. by T. Bodnár, G. P. Galdi, and Š. Nečasová. Cham: Springer International Publishing, 2017, pp. 327–396. ISBN: 978-3-319-60281-3.

[101] M. E. Taskin et al. "Micro-scale modeling of flow and oxygen transfer in hollow-fiber membrane bundle". In: *Journal of Membrane Science* 362.1-2 (Oct. 2010), pp. 172–183. DOI: 10.1016/j.memsci.2010.06.034.

[102] T. Tohme, P. Magaud, and L. Baldas. "Transport of Non-Spherical Particles in Square Microchannel Flows: A Review". In: *Micromachines* 12.3 (Mar. 7, 2021), p. 277. DOI: 10.3390/mi12030277.

[103] J. Tu, G. Yeoh, and C. Liu. *Computational Fluid Dynamics: A Practical Approach*. Elsevier Science, 2012. ISBN: 9780080982434.

[104] A. Viallat and M. Abkarian, eds. *Dynamics of blood cell suspensions in microflows*. London, England: CRC Press, Dec. 2019. ISBN: 978-1-138-03205-7.

[105] D. J. Vitello et al. "Blood Density Is Nearly Equal to Water Density: A Validation Study of the Gravimetric Method of Measuring Intraoperative Blood Loss". In: *Journal of Veterinary Medicine* 2015 (Jan. 29, 2015), pp. 1–4. DOI: 10.1155/2015/152730.

[106] H. M. Vollebregt, R. G. M. Van Der Sman, and R. M. Boom. "Suspension Flow Modelling in Particle Migration and Microfiltration". In: *Soft Matter* 6.24 (2010), p. 6052. DOI: 10.1039/c0sm00217h.

[107] C. Wagner, P. Steffen, and S. Svetina. “Aggregation of red blood cells: From rouleaux to clot formation”. In: *Comptes Rendus Physique* 14.6 (June 2013), pp. 459–469. DOI: 10.1016/j.crhy.2013.04.004.

[108] M. H. Weissman and L. F. Mockros. “Oxygen and Carbon Dioxide Transfer in Membrane Oxygenators”. In: *Medical & Biological Engineering* 7.2 (Mar. 1969), pp. 169–184. DOI: 10.1007/BF02474173.

[109] M. H. Weissman and L. F. Mockros. “Oxygen Transfer to Blood Flowing in Round Tubes”. In: *Journal of the Engineering Mechanics Division* 93.6 (Dec. 1967), pp. 225–244. DOI: 10.1061/jmcea3.0000917.

[110] S. Wickramasinghe, J. Garcia, and B. Han. “Mass and Momentum Transfer in Hollow Fibre Blood Oxygenators”. In: *Journal of Membrane Science* 208.1-2 (Oct. 2002), pp. 247–256. DOI: 10.1016/S0376-7388(02)00281-8.

[111] W. Wu et al. “Simulation of Blood Flow in a Sudden Expansion Channel and a Coronary Artery”. In: *Journal of Computational and Applied Mathematics* 376 (Oct. 2020), p. 112856. DOI: 10.1016/j.cam.2020.112856.

[112] W.-T. Wu et al. “A Non-Linear Fluid Suspension Model for Blood Flow”. In: *International Journal of Non-Linear Mechanics* 109 (Mar. 2019), pp. 32–39. DOI: 10.1016/j.ijnonlinmec.2018.11.002.

[113] F. Yilmaz and M. Gundogdu. “A critical review on blood flow in large arteries; relevance to blood rheology, viscosity models, and physiologic conditions”. In: *Korea-Australia Rheology Journal* 20 (Dec. 2008), pp. 197–211.

[114] J. Zhou et al. “Isolation of Cells from Whole Blood Using Shear-Induced Diffusion”. In: *Scientific Reports* 8.1 (June 20, 2018), p. 9411. DOI: 10.1038/s41598-018-27779-2.

Appendices

Appendix A

Conservation of the Total Mass of Oxygen

A.1 Introduction

The complex process of oxygenation in whole blood was explored in chapter 7. In the literature, two model types are proposed to describe this phenomenon: a mixture and a two-phase formulation. While this study focused on a mixture model for blood flow, necessitating a mixture formulation for oxygenation, the existing mixture model in the literature was not derived from the considerations discussed in chapter 3. Thus, this appendix delves into the derivation of a new oxygenation model, aligning with the mixture formulations considered throughout this study. Throughout the derivation, mathematical contributions are marked in **red** to indicate changes with respect to previous derivation steps.

A.2 Total Mass of Oxygen

The total mass of oxygen in whole blood at any given time for an arbitrary fluid element consists of three contributions: the oxygen dissolved in blood plasma, the oxygen dissolved in the cytoplasm of the red blood cells, and the oxygen bound to the haemoglobin in the cytoplasm of the red blood cells [50]. These three species can reversibly exchange oxygen, but their combined mass remains constant, ensuring the total amount of oxygen is conserved for the fluid element. For now, these oxygen species may be distinguished by the phase in which they are suspended. The contribution of the mass of the bound oxygen should be determined using the stoichiometric relation that governs the reaction between oxygen and haemoglobin. The one-step approximation for this reversible reaction, as was introduced in equation 7.6, is denoted by,

$$1 \text{ mol } O_2 + 1 \text{ mol } Hb \rightleftharpoons 1 \text{ mol } HbO_2. \tag{7.6}$$

Where O_2 denotes the oxygen species, Hb the haemoglobin species, and HbO_2 the bound oxygen or oxyhaemoglobin species. The total mass of oxygen can now be expressed as the sum of all three contributions while distinguishing the contributions of both phases,

$$m_{O_2,t} \coloneqq \underbrace{m_{O_2,c}}_{\text{Continuous}} + \underbrace{m_{O_2,d} + \frac{M_{O_2}}{M_{HbO_2}} m_{HbO_2,d}}_{\text{Dispersed}}. \tag{A.1}$$

Where m denotes the mass, M the molar mass, the sub-scripted t the consideration of total mass, c the mass in the continuous phase, and d the mass in the dispersed phase. The relation for the total mass of oxygen can now be expressed in terms of the partial mass density of each species for the volume of an arbitrary fluid element, $\Omega(t)$. The partial volumes correspond to those depicted in figure 3.2, with the exclusion of the oxygen mass contribution within the interface, i.e. the cell membrane. The total mass of oxygen in the arbitrary fluid element is then expressed as,

$$\int_{\Omega(t)} \rho_{O_2,t} dV = \int_{\Omega_c(t)} \rho_{O_2,c} dV + \int_{\Omega_d(t)} \left[\rho_{O_2,d} + \frac{M_{O_2}}{M_{HbO_2}} \rho_{HbO_2,d} \right] dV. \tag{A.2}$$

Where ρ denotes the mass density, and with the neglect of the interface volume, $\Omega(t) = \Omega_c(t) + \Omega_d(t)$. The integrands on the right-hand side may now be recognized as the conserved quantities per unit volume of either phase, such that the conservation of their respective mass fraction is governed by the local-instant formulation denoted in equation 3.4. With the mass fractions denoted by,

$$\begin{aligned} \omega_{O_2,c,t} &\coloneqq \omega_{O_2,c} \equiv \frac{\rho_{O_2,c}}{\rho_c}, \\ \omega_{O_2,d,t} &\coloneqq \frac{\rho_{O_2,d}}{\rho_d} + \frac{M_{O_2}}{M_{HbO_2}} \frac{\rho_{HbO_2,d}}{\rho_d}. \end{aligned} \tag{A.3}$$

Where the sub-scripted inclusion of t denotes the combined or total consideration of the dissolved and bound oxygen mass fractions. In the continuous phase, this total mass fraction is simply equal to that of the dissolved oxygen.

The derivation of the two-fluid model formulations for these local-instant formulations requires the process of time-averaging, as detailed in section 3.2.2, where generally the conserved variable per unit mass is averaged using Favre averaging. While the mass fraction of each species is not a candidate for Favre averaging in the general sense, i.e. the product of the conserved variable per unit mass with the phasic density is generally considered to be an extensive property of the phase such as momentum or energy, it does represent an additive set function of mass. This consideration for the mass fraction is best envisioned by considering the generic notion of mass conservation for the phases, where the conserved quantity per unit mass is taken as unity. The value resembles the consideration of a mass fraction for a single species, which is naturally equal to unity. The consideration of mass conservation for the entire mixture can still be done using the value of unity, considering the mass fraction for the total mass of oxygen is generally assumed negligible compared to the mass fractions of the individual phases. The Favre-averaged total mass fractions of oxygen for the individual phases are now denoted by,

$$\begin{aligned} \widetilde{\omega}_{O_2,c,t} &= \widetilde{\omega}_{O_2,c}, \\ \widetilde{\omega}_{O_2,d,t} &= \widetilde{\omega}_{O_2,d} + \frac{M_{O_2}}{M_{HbO_2}} \widetilde{\omega}_{HbO_2,d}. \end{aligned} \tag{A.4}$$

Where the additive property of integrals is used in the time-averaging of the dispersed phase total oxygen mass fraction, and the fraction of molecular weights is assumed to be constant. The mixture total oxygen mass fraction is now defined by considering the mixture definition for the Favre-averaged quantities, as defined in equation 3.16, for both the dissolved and bound oxygen separately such that it is denoted by,

$$\begin{aligned} \omega_{O_2,m,t} &= \omega_{O_2,m} + \frac{M_{O_2}}{M_{HbO_2}} \omega_{HbO_2,m} \\ &= \frac{1}{\rho_m} \left(\alpha_c \overline{\overline{\rho}}_c \widetilde{\omega}_{O_2,c} + \alpha_d \overline{\overline{\rho}}_d \widetilde{\omega}_{O_2,d} \right) + \frac{1}{\rho_m} \frac{M_{O_2}}{M_{HbO_2}} \left(\alpha_d \overline{\overline{\rho}}_d \widetilde{\omega}_{HbO_2,d} \right). \end{aligned} \tag{A.5}$$

A.3 Mixture Conservation

The mass fraction for the total mass of oxygen in the mixture, as defined in the preceding section, is a conserved quantity per unit mass. The conservation of the quantity inside the mixture can be described using the drift-flux model, presented in equation 3.20. The conservation equation for the mass of oxygen in whole blood may then be denoted by substitution of $\phi_m = \omega_{O_2,m,t}$,

$$\begin{aligned} &\underbrace{\frac{\partial \rho_m \omega_{O_2,m,t}}{\partial t}}_{\text{Temporal}} + \underbrace{\nabla \cdot (\rho_m \omega_{O_2,m,t} \boldsymbol{u}_m)}_{\text{Advection}} = \underbrace{-\nabla \cdot \left(\boldsymbol{\mathcal{J}}_{\omega_{O_2,m,t}} \right)}_{\text{Diffusion}} + \underbrace{\rho_m \mathcal{S}_{\omega_{O_2,m,t}}}_{\text{Source}} \\ &\underbrace{-\nabla \cdot \left(\boldsymbol{\mathcal{J}}^D_{\omega_{O_2,m,t}} \right)}_{\text{Drift}} \underbrace{-\nabla \cdot \left(\boldsymbol{\mathcal{J}}^T_{\omega_{O_2,m,t}} \right)}_{\text{Turbulence}} + \underbrace{\mathcal{I}_{\omega_{O_2,m,t}}}_{\text{Interface}} . \end{aligned} \tag{A.6}$$

The resulting conservation equation may already be simplified by considering there is no production or destruction of oxygen inside of the arbitrary fluid element, such that $\mathcal{S}_{\omega_{O_2,m,t}} = 0$. The influence of turbulence may also be omitted following the considerations for momentum described in section 4.2 or 8.1, such that $\boldsymbol{\mathcal{J}}^T_{\omega_{O_2,m,t}} \rightarrow \mathbf{0}\ \forall \boldsymbol{x}, t$. Lastly, it may be assumed that the interfacial transfer of oxygen, i.e. the transport of oxygen over the cell membrane, does not enhance the total amount of oxygen, such that $\mathcal{I}_{\omega_{O_2,m,t}} = 0\ \forall \boldsymbol{x}, t$. The simplified consideration can now be expressed as,

$$\frac{\partial \rho_m \omega_{O_2,m,t}}{\partial t} + \nabla \cdot (\rho_m \omega_{O_2,m,t} \boldsymbol{u}_m) = -\nabla \cdot \left(\boldsymbol{\mathcal{J}}_{\omega_{O_2,m,t}} \right) - \nabla \cdot \left(\boldsymbol{\mathcal{J}}^D_{\omega_{O_2,m,t}} \right). \tag{A.7}$$

This formulation can now be expanded by substitution of equation A.5, and simplified by the consideration of mixture mass conservation, and assuming the mass fractions are continuous in space and time,

$$\rho_m \frac{D_m \omega_{O_2,m}}{Dt} + \overline{\overline{\rho}}_d \frac{M_{O_2}}{M_{HbO_2}} \frac{D_m}{Dt} \left(\alpha_d \widetilde{\omega}_{HbO_2,d} \right) = -\nabla \cdot \left(\boldsymbol{\mathcal{J}}_{\omega_{O_2,m,t}} \right) - \nabla \cdot \left(\boldsymbol{\mathcal{J}}^D_{\omega_{O_2,m,t}} \right). \tag{A.8}$$

Where the mass densities for the mixture and the individual phases are assumed constant, considering whole blood and its primary constituents can be assumed incompressible fluids as described in section 8.1. Additionally, the operator $\frac{D_m}{Dt}(.)$ denotes the material derivative in terms of the mixture velocity, which is defined for an arbitrary scalar quantity ϕ by,

$$\frac{D_m \phi}{Dt} = \frac{\partial \phi}{\partial t} + \boldsymbol{u}_m \cdot \nabla \phi. \tag{A.9}$$

The final conservation relation for the total mass of oxygen now contains several quantities that generally are not explicitly solved for and must thus be closed using constitutive modelling.

A.4 Constitutive Modelling of the Oxyhaemoglobin

The Favre-averaged oxyhaemoglobin mass fraction can be modelled using the local oxygen saturation under the assumption that the oxygen dissolved in the red blood cell phase and the haemoglobin are in chemical equilibrium. While this equilibrium consideration does not generally hold for the entire cell, it is the case in the bulk of the cell. The non-equilibrium is only observed in a boundary layer near the cell membrane, which is

generally much smaller than the characteristic length scale of the red blood cell [23]. The oxygen saturation, described by the oxygen dissociation curve, is a non-linear function of the partial pressure of the dissolved oxygen in blood and, as was introduced in equation 7.7, may be related to the haemoglobin concentration by,

$$S_{O_2}(p_{O_2}) \coloneqq \frac{c_{HbO_2,d}}{c_{Hb,t}} \equiv \frac{c_{HbO_2,d}}{c_{Hb} + c_{HbO_2,d}}. \tag{7.7}$$

Where $c_{Hb,t}$ denotes the total haemoglobin concentration, which is a constant. The mass fraction of the oxyhaemoglobin can now be derived using the relation between mass and molar concentrations [12],

$$\widetilde{\omega}_{HbO_2,d} = \frac{c_{Hb,t} M_{HbO_2}}{\overline{\overline{\rho}}_d} S_{O_2}(p_{O_2}). \tag{A.10}$$

Where the oxygen saturation can be modelled using the Hill equation, given in equation 7.8. The oxygen partial pressure of the mixture will be considered here for simplicity, given that there is no general definition for it in terms of a two-phase consideration. The oxygen partial pressure for the mixture itself can finally be related to the mixture mass fraction of oxygen using the Henry-Dalton law, defined in equation 7.4, along with the relation between mass and molar concentrations,

$$p_{O_2,m} \equiv \frac{\rho_m}{\beta_{O_2,m} M_{O_2}} \omega_{O_2,m}. \tag{A.11}$$

Where $\beta_{O_2,m}$ denotes the Bunsen solubility coefficient of oxygen in the mixture, for which the variations may generally be neglected [23]. Additionally, the mixture dissolved oxygen mass fraction was assumed normalized using the mixture mass density. This normalization effectively defines the mixture dissolved oxygen mass density as the phase average of the densities of both phases,

$$\overline{\overline{\rho}}_{O_2,m} = \rho_m \omega_{O_2,m} = \alpha_c \overline{\overline{\rho}}_c \widetilde{\omega}_{O_2,c} + \alpha_d \overline{\overline{\rho}}_d \widetilde{\omega}_{O_2,d} = \alpha_c \overline{\overline{\rho}}_{O_2,c} + \alpha_d \overline{\overline{\rho}}_{O_2,d} \tag{A.12}$$

The constitutive model for the mass fraction of the oxyhaemoglobin may now be substituted into equation A.8 as follows,

$$\rho_m \frac{D_m \omega_{O_2,m}}{Dt} + c_{Hb,t} M_{O_2} \frac{D_m}{Dt} \left(\alpha_d S_{O_2}(p_{O_2,m})\right) = -\nabla \cdot \left(\boldsymbol{\mathcal{J}}_{\omega_{O_2,m,t}}\right) - \nabla \cdot \left(\boldsymbol{\mathcal{J}}^D_{\omega_{O_2,m,t}}\right). \tag{A.13}$$

This formulation can be expanded by assuming the dispersed phase volume fraction and oxygen saturation are continuous in space and time,

$$\begin{aligned} \rho_m \frac{D_m \omega_{O_2,m}}{Dt} + c_{Hb,t} M_{O_2} \left[S_{O_2}(p_{O_2,m}) \frac{D_m \alpha_d}{Dt} + \alpha_d \frac{\partial S_{O_2}}{\partial p_{O_2,m}} \frac{D_m p_{O_2,m}}{Dt} \right] \\ = -\nabla \cdot \left(\boldsymbol{\mathcal{J}}_{\omega_{O_2,m,t}}\right) - \nabla \cdot \left(\boldsymbol{\mathcal{J}}^D_{\omega_{O_2,m,t}}\right). \end{aligned} \tag{A.14}$$

Finally, the formulation may be simplified using the relation between the oxygen partial pressure and the mass fraction of the mixture, denoted in equation A.11,

$$\begin{aligned} \rho_m \left(1 + \alpha_d \frac{c_{Hb,t}}{\beta_{O_2,m}} \frac{\partial S_{O_2}}{\partial p_{O_2,m}}\right) \frac{D_m \omega_{O_2,m}}{Dt} + c_{Hb,t} M_{O_2} S_{O_2}(p_{O_2,m}) \frac{D_m \alpha_d}{Dt} \\ = -\nabla \cdot \left(\boldsymbol{\mathcal{J}}_{\omega_{O_2,m,t}}\right) - \nabla \cdot \left(\boldsymbol{\mathcal{J}}^D_{\omega_{O_2,m,t}}\right). \end{aligned} \tag{A.15}$$

A.5 Constitutive Modelling of the Molecular Diffusion

Molecular diffusion is characterized by the diffusion of the dissolved and bound oxygen in both the continuous and dispersed phases such that, $\boldsymbol{\mathcal{J}}_{\omega_{O_2,m,t}} = \boldsymbol{\mathcal{J}}_{\omega_{O_2,m}} + \boldsymbol{\mathcal{J}}_{\omega_{HbO_2,m}}$. The mixture diffusion fluxes are, in turn, governed by the phase-averaged diffusion fluxes, given in equation 3.15, and the phase-averaged fluxes by Fick's first law of binary diffusion, as was introduced in equation 7.1,

$$\boldsymbol{\mathcal{J}}_{\omega_a} = -\rho_t \mathcal{D}_{a,b} \nabla \omega_a. \tag{7.1}$$

The total molecular diffusion flux for the total mass of oxygen is now denoted by,

$$\begin{aligned} \boldsymbol{\mathcal{J}}_{\omega_{O_2,m,t}} = &-\alpha_c \overline{\overline{\rho}}_c \mathcal{D}_{O_2,c} \nabla \widetilde{\omega}_{O_2,c} - \alpha_d \overline{\overline{\rho}}_d \mathcal{D}_{O_2,d} \nabla \widetilde{\omega}_{O_2,d} \\ &- \alpha_d \overline{\overline{\rho}}_d \mathcal{D}_{HbO_2,d} \nabla \widetilde{\omega}_{HbO_2,d}. \end{aligned} \tag{A.16}$$

Where the molecular diffusion coefficient of oxygen in the continuous and dispersed phases are typically taken constant and equal [50], e.g. $\mathcal{D}_{O_2,c} \approx \mathcal{D}_{O_2,d} \approx \mathcal{D}_{O_2,m}$. The constitutive model for the mass fraction of the oxyhaemoglobin can be substituted in the definition of this molecular diffusion flux such that the flux can be expressed as,

$$\begin{aligned} \boldsymbol{\mathcal{J}}_{\omega_{O_2,m,t}} = &-\alpha_c \overline{\overline{\rho}}_c \mathcal{D}_{O_2,c} \nabla \widetilde{\omega}_{O_2,c} - \alpha_d \overline{\overline{\rho}}_d \mathcal{D}_{O_2,d} \nabla \widetilde{\omega}_{O_2,d} \\ &- \alpha_d \mathcal{D}_{HbO_2,d} c_{Hb,t} M_{HbO_2} \nabla S_{O_2}(p_{O_2,m}). \end{aligned} \tag{A.17}$$

The molecular diffusion flux for the oxyhaemoglobin may now be rewritten in terms of the mass fraction of the mixture, denoted in equation A.10, such that the total molecular diffusion flux is denoted by,

$$\begin{aligned} \boldsymbol{\mathcal{J}}_{\omega_{O_2,m,t}} = &-\alpha_c \overline{\overline{\rho}}_c \mathcal{D}_{O_2,c} \nabla \widetilde{\omega}_{O_2,c} - \alpha_d \overline{\overline{\rho}}_d \mathcal{D}_{O_2,d} \nabla \widetilde{\omega}_{O_2,d} \\ &- \alpha_d \rho_m \mathcal{D}_{HbO_2,d} \frac{c_{Hb,t}}{\beta_{O_2,m}} \frac{M_{HbO_2}}{M_{O_2}} \frac{\partial S_{O_2}}{\partial p_{O_2,m}} \nabla \omega_{O_2,m}. \end{aligned} \tag{A.18}$$

The consideration of chemical equilibrium in the complete red blood cell, considered in the constitutive model of the oxyhaemoglobin, also allows for a simplified consideration of the molecular diffusion in the blood cell phase. The bulk chemical equilibrium is caused by a major resistance of molecular diffusion inside the boundary layer and causes $\nabla \widetilde{\omega}_{O_2,d} \to \mathbf{0}$ [23]. The total molecular diffusion flux can then be reduced to,

$$\begin{aligned} \boldsymbol{\mathcal{J}}_{\omega_{O_2,m,t}} = &-\alpha_c \overline{\overline{\rho}}_c \mathcal{D}_{O_2,c} \nabla \widetilde{\omega}_{O_2,c} \\ &- \alpha_d \rho_m \mathcal{D}_{HbO_2,d} \frac{c_{Hb,t}}{\beta_{O_2,m}} \frac{M_{HbO_2}}{M_{O_2}} \frac{\partial S_{O_2}}{\partial p_{O_2,m}} \nabla \omega_{O_2,m}. \end{aligned} \tag{A.19}$$

The gradient of the phase-averaged mass fraction of oxygen dissolved in the continuous phase can be written in terms of the mixture mass fraction by expanding it as follows,

$$\begin{aligned} \nabla \omega_{O_2,m} &= \frac{1}{\rho_m} \nabla \left(\alpha_c \overline{\overline{\rho}}_c \widetilde{\omega}_{O_2,c} + \alpha_d \overline{\overline{\rho}}_d \widetilde{\omega}_{O_2,d} \right) \\ &= \alpha_c \frac{\overline{\overline{\rho}}_c}{\rho_m} \nabla \widetilde{\omega}_{O_2,c} + \frac{\overline{\overline{\rho}}_d \widetilde{\omega}_{O_2,d} - \overline{\overline{\rho}}_c \widetilde{\omega}_{O_2,c}}{\rho_m} \nabla \alpha_d. \end{aligned} \tag{A.20}$$

Where the gradient of the continuous phase volume fraction was written in terms of the dispersed phase volume fraction using the axiom of continuity, as given in equation 8.1. The second contribution is here assumed negligible compared to the first contribution, effectively neglecting molecular diffusion governed by the difference in phasic dissolved oxygen concentrations, such that the final total molecular diffusion flux is denoted by,

$$\boldsymbol{\mathcal{J}}_{\omega_{O_2,t}} = -\rho_m \left[\mathcal{D}_{O_2,c} + \alpha_d \mathcal{D}_{HbO_2,d} \frac{c_{Hb,t}}{\beta_{O_2,m}} \frac{M_{HbO_2}}{M_{O_2}} \frac{\partial S_{O_2}}{\partial p_{O_2,m}} \right] \nabla \omega_{O_2,m}. \tag{A.21}$$

A.6 Constitutive Modelling of the Phase Diffusion

The relative phase motion characterizes the macroscopic phase diffusion of the oxygen. The mixture flux, as was introduced in equation 3.21, is here denoted by,

$$\boldsymbol{\mathcal{J}}^{D}_{\phi_m} = \sum_k \boldsymbol{\mathcal{J}}^{D}_{\phi_k} = \sum_k \alpha_k \overline{\overline{\rho}}_k \widetilde{\phi}_k \boldsymbol{V}_{km}. \tag{3.21}$$

The macroscopic phase diffusion flux may now be determined using the Favre-averaged mass fractions defined in equation A.4, along with the phase diffusion velocities defined in equation 3.18. Generally, however, only one of the two-phase diffusion velocities is modelled, of which the dispersed phase diffusion velocity is typically modelled. The continuous phase diffusion velocity must then be derived from the following relating identity, as was introduced in equation 4.16,

$$\sum_k \frac{\alpha_k \overline{\overline{\rho}}_k}{\rho_m} \boldsymbol{V}_{km} = \boldsymbol{0}. \tag{4.16}$$

The continuous phase diffusion velocity is denoted in terms of the dispersed phase diffusion velocity by,

$$\boldsymbol{V}_{cm} = -\frac{\alpha_d \overline{\overline{\rho}}_d}{\alpha_c \overline{\overline{\rho}}_c} \boldsymbol{V}_{dm} \tag{A.22}$$

The macroscopic phase diffusion flux is then denoted by,

$$\boldsymbol{\mathcal{J}}^{D}_{\omega_{O_2,t}} = \alpha_d \overline{\overline{\rho}}_d \left[\widetilde{\omega}_{O_2,d} - \widetilde{\omega}_{O_2,c} + \frac{M_{O_2}}{M_{HbO_2}} \widetilde{\omega}_{HbO_2,d} \right] \boldsymbol{V}_{dm}. \tag{A.23}$$

Where, similarly to the derivation of the constitutive model for the molecular diffusion flux, the effect due to the difference in phasic dissolved oxygen concentration is assumed negligible, and the constitutive model for the mass fraction of the oxyhaemoglobin may be substituted, such that the macroscopic phase diffusion flux is denoted by,

$$\boldsymbol{\mathcal{J}}^{D}_{\omega_{O_2,t}} = \alpha_d c_{Hb,t} M_{O_2} S_{O_2}(p_{O_2,m}) \boldsymbol{V}_{dm}. \tag{A.24}$$

A.7 Conservation of the Total Mass of Oxygen

The final relation that describes the conservation of the total mass of oxygen based on a mixture consideration can now be derived by substituting the constitutive models for the molecular and phase diffusion fluxes into equation A.15,

$$\begin{aligned} &\underbrace{\rho_m \left(1 + \alpha_d \frac{c_{Hb,t}}{\beta_{O_2,m}} \frac{\partial S_{O_2}}{\partial p_{O_2,m}} \right) \frac{D_m \omega_{O_2,m}}{Dt} + c_{Hb,t} M_{O_2} S_{O_2}(p_{O_2,m}) \frac{D_m \alpha_d}{Dt}}_{\text{Temporal + Advection}} \\ &= \underbrace{\nabla \cdot \left(\rho_m \left[\mathcal{D}_{O_2,c} + \alpha_d \mathcal{D}_{HbO_2,d} \frac{M_{HbO_2}}{M_{O_2}} \frac{c_{Hb,t}}{\beta_{O_2,m}} \frac{\partial S_{O_2}}{\partial p_{O_2,m}} \right] \nabla \omega_{O_2,m} \right)}_{\text{Diffusion}} \\ &\quad \underbrace{- \nabla \cdot \left(\alpha_d c_{Hb,t} M_{O_2} S_{O_2}(p_{O_2,m}) \boldsymbol{V}_{dm} \right)}_{\text{Drift}}. \end{aligned} \tag{A.25}$$

The resulting relation can be simplified by separating the macroscopic phase diffusion or drift flux into a contribution in terms of saturation and the phase diffusion velocity.

Consequently, the latter contribution and the second term of the resulting relation cancel as these exactly make up the dispersed phase mass conservation denoted in equation 8.6. The relation is now denoted by,

$$\begin{aligned}\rho_m \left(1 + \alpha_d \frac{c_{Hb,t}}{\beta_{O_2,m}} \frac{\partial S_{O_2}}{\partial p_{O_2,m}}\right) \frac{D_m \omega_{O_2,m}}{Dt} + \rho_m \alpha_d \frac{c_{Hb,t}}{\alpha_{O_2,m}} \frac{\partial S_{O_2}}{\partial p_{O_2,m}} \boldsymbol{V}_{dm} \cdot \nabla \omega_{O_2,m} \\ = \nabla \cdot \left(\rho_m \left[\mathcal{D}_{O_2,c} + \mathcal{D}_{HbO_2,d} \frac{M_{HbO_2}}{M_{O_2}} \alpha_d \frac{c_{Hb,t}}{\beta_{O_2,m}} \frac{\partial S_{O_2}}{\partial p_{O_2,m}}\right] \nabla \omega_{O_2,m}\right).\end{aligned} \tag{A.26}$$

For convenience, an oxyhaemoglobin transport coefficient, an effective diffusivity coefficient, and an arbitrary oxygen concentration variable may be defined such that the oxygen transport in a mixture consideration of whole blood is governed by,

$$(1 + C_{HbO_2}) \frac{D_m \phi_{O_2,m}}{Dt} + C_{HbO_2} \boldsymbol{V}_{dm} \cdot \nabla \phi_{O_2,m} = \nabla \cdot (\mathcal{D}_{\text{eff}} \nabla \phi_{O_2,m}). \tag{A.27}$$

Where,

$$\begin{aligned} C_{HbO_2} &\coloneqq \alpha_d \frac{c_{Hb,t}}{\beta_{O_2,m}} \frac{\partial S_{O_2}}{\partial p_{O_2,m}}, \\ \mathcal{D}_{\text{eff}} &\coloneqq \mathcal{D}_{O_2,c} + \mathcal{D}_{HbO_2,d} \frac{M_{HbO_2}}{M_{O_2}} \alpha_d \frac{c_{Hb,t}}{\beta_{O_2,m}} \frac{\partial S_{O_2}}{\partial p_{O_2,m}} \\ &\equiv \mathcal{D}_{O_2,c} + \mathcal{D}_{HbO_2,d} \frac{M_{HbO_2}}{M_{O_2}} C_{HbO_2}. \end{aligned} \tag{A.28}$$

The choice of the arbitrary oxygen concentration variable is now solely dependent on the conversion of the variable to the mixture partial pressure of dissolved oxygen, which can, for common oxygen concentration variables, be determined using table A.1.

$\phi_{O_2,m}$	$\omega_{O_2,m}$	$\rho_{O_2,m}$	$c_{O_2,m}$	$p_{O_2,m}$
$p_{O_2,m}$	$\frac{\rho_m}{\beta_{O_2,m} M_{O_2}} \phi_{O_2,m}$	$\frac{1}{\beta_{O_2,m} M_{O_2}} \phi_{O_2,m}$	$\frac{1}{\beta_{O_2,m}} \phi_{O_2,m}$	$\phi_{O_2,m}$

Table A.1: Conservation of total mass of oxygen model conversion table.

A.8 Model Derivation Verification

A newly derived model must thoroughly be verified and validated to assess whether it behaves according to expectations.

A.8.1 Dimensions

A first verification, rooted in good engineering practices, is to verify whether the dimensions of the derived governing relation are consistent. From the initial contribution denoted in the governing relation, equation A.27, it can be deduced that the oxyhaemoglobin transport coefficient should be dimensionless. The dimensions of the Bunsen solubility coefficient are easily deduced from the Henry-Dalton law denoted in equation 7.4,

$$[\beta_{a,b}] = \left[\frac{c_a}{p_a}\right] = \frac{\text{mol/m}^3}{\text{Pa}} = \text{mol/(Pa} \cdot \text{m}^3). \tag{A.29}$$

The dimensions of the oxyhaemoglobin transport coefficient are now denoted by,

$$[C_{HbO_2}] = \left[\alpha_d \frac{c_{Hb,t}}{\beta_{O_2,m}} \frac{\partial S_{O_2}}{\partial p_{O_2,m}}\right] = [-] \frac{\mathrm{mol/m^3}}{\mathrm{mol/(Pa \cdot m^3)}} \frac{[-]}{\mathrm{Pa}} = [-]\,. \tag{A.30}$$

The effective diffusivity should by its own definition have the dimensions of a diffusivity coefficient, its dimensions are denoted by,

$$[\mathcal{D}_{\mathrm{eff}}] = \left[\mathcal{D}_{O_2,c} + \mathcal{D}_{HbO_2,d} \frac{M_{HbO_2}}{M_{O_2}} C_{HbO_2}\right] = \mathrm{m^2/s} + \mathrm{m^2/s} \frac{\mathrm{g/mol}}{\mathrm{g/mol}} [-] = \mathrm{m^2/s}. \tag{A.31}$$

The dimensions of the entire governing relation are now denoted by,

$$\begin{aligned} &\left[(1 + C_{HbO_2}) \frac{D_m \phi_{O_2,m}}{Dt}\right] + [C_{HbO_2} \boldsymbol{V}_{dm} \cdot \nabla \phi_{O_2,m}] = [\nabla \cdot (\mathcal{D}_{\mathrm{eff}} \nabla \phi_{O_2,m})]\,. \\ &\quad \Rightarrow ([-] + [-]) \frac{[\phi_{O_2,m}]}{\mathrm{s}} + [-]\,\mathrm{m/s} \cdot \frac{1}{\mathrm{m}} [\phi_{O_2,m}] = \frac{1}{\mathrm{m}} \cdot \left(\mathrm{m^2/s} \frac{1}{\mathrm{m}} [\phi_{O_2,m}]\right). \end{aligned} \tag{A.32}$$

Where it is implied that the dimensions of the governing relation are consistent, and every contribution has the dimensions of the arbitrary oxygen concentration variable per unit time.

A.8.2 Limiting Behaviour

With the dimensions of the governing relation verified in the preceding section, the physical response of the model should be reviewed. Here, the response in terms of the limiting behaviour is considered. The two considerations of most interest are the limiting behaviour of the dispersed phase volume fraction and the saturation gradient. In the limit of zero dispersed phase volume fraction, i.e. the exclusion of red blood cells, the oxyhaemoglobin transport coefficient also approaches zero. The resulting differential equation then approaches a simple linear advection-diffusion equation in terms of oxygen through blood plasma,

$$\frac{D_m \phi_{O_2,m}}{Dt} = \mathcal{D}_{O_2,c} \nabla^2 \phi_{O_2,m}. \tag{A.33}$$

Which resembles Fick's second law of binary diffusion for an advecting fluid element, which is in line with the expected behaviour.
The saturation gradient has two limits of interest, zero and fully saturated blood cells. Both of these limits result in a zero gradient, as can be deduced from figure 7.2. The resulting governing relation then, similarly to the exclusion of red blood cells, results in the simple linear advection-diffusion equation denoted in equation A.33. While this results may seem counter-intuitive, it essentially states that the time-averaged behaviour of the chaotic oxygen transport around and through the red blood cells approaches that of single-phase blood plasma diffusion.

Appendix B

Solver Implementation Verification

B.1 Introduction

The PIMPLE-algorithm-based solver, PimpleFoam, included in the open-source OpenFOAM framework, was enhanced for this study to incorporate the drift flux model denoted in equation 8.4. This model enables the description of the fluid flow behaviour of whole blood, including the migration of red blood cells. The diffusive flux model denoted in equation 8.6 included the migratory behaviour. Additionally, the solver adopted the conservation of total mass of oxygen, oxygenation model as denoted in equation 8.7. This model represents the oxygen transport and oxygen binding to the haemoglobin. The implementation and validation of these models into the existing PimpleFoam solver was considered through the method of manufactured solutions (MMS). The method and the proposed solutions are discussed in this appendix.

B.2 The Method of Manufactured Solutions

The method of manufactured solutions provides a systematic procedure to validate the numerical implementation of governing partial differential equations [79]. The framework is relatively straightforward and works by supplying a proposal solution as a function of space and time, e.g. $\phi = \Phi(\boldsymbol{x}, t)$. This proposal solution is not limited to physically accurate solutions, and any form may be proposed, providing it is a nontrivial, analytic solution that exercises all included derivative orders [10].
The methodology involves substituting the proposal solution into the governing relation and utilizing the resulting remainder within the numerical implementation to correct the right-hand side of the system of algebraic equations. For instance, consider a one-dimensional autonomous second-order linear operator derived from the general single-phase conservation law as proposed in equation 3.2,

$$\mathcal{L}_\phi(\phi) \equiv \frac{\partial \rho\phi}{\partial t} - \frac{\partial}{\partial x}\left(\Gamma \frac{\partial \phi}{\partial x}\right) = 0. \tag{B.1}$$

Here the advection and volumetric source contributions are omitted, the density is taken as some constant scalar, and the diffusion flux is taken as $\boldsymbol{\mathcal{J}_\phi} = -\Gamma\nabla\phi$, with Γ some constant scalar. To ensure all derivative orders are exercised, a simple harmonic solution in terms of space and time may be employed,

$$\Phi(x, t) = A \sin(x - Bt). \tag{B.2}$$

Where A and B are some constant scalars. The correction, or artificial source term, then simply becomes,

$$\mathcal{L}_\phi(\Phi) = -\rho A \left(B \cos\left(x - Bt\right) + \Gamma \sin\left(x - Bt\right) \right). \tag{B.3}$$

The modified governing relation then becomes,

$$\mathcal{L}_\Phi(\phi) \equiv \frac{\partial \rho\phi}{\partial t} - \frac{\partial}{\partial x}\left(\Gamma \frac{\partial \phi}{\partial x}\right) = -\rho A \left(B \cos\left(x - Bt\right) + \Gamma \sin\left(x - Bt\right) \right). \tag{B.4}$$

This modified relation may now be resolved numerically to validate the implementation by examining whether $\phi(x,t) \to \Phi(x,t)$ using, e.g. grid convergence studies [10]. The initial and boundary conditions for this analysis are simply given by $\Phi(x,t)$ under the appropriate conditions, where any canonical boundary condition type and combination of can be applied, i.e. Dirichlet, Neumann, Robin.

B.3 Manufactured Solutions

To ensure the implementations of the governing relation are appropriately checked, an appropriate manufactured solution must be proposed for each solution variable. As discussed in the preceding section, these manufactured solutions are not limited by physical correctness but must be nontrivial, analytic solutions that exercise all derivative orders. The manufactured solutions for the mixture velocity, mixture kinematic pressure, dispersed phase volume fraction, and oxygen partial pressure equipped to check the implementation are proposed in this section.

B.3.1 Taylor-Green Vortex Flow

The manufactured solutions proposed for the mixture velocity field is the three-dimensional Taylor-Green Vortex flow as proposed by Taylor and Green in 1937 [68]. The field is used for its inherent complexity that will ensure, firstly, spatial and temporal differentiability over all included derivative orders, a divergence-free velocity field, a constraint imposed by the pressure-velocity coupling of the PIMPLE algorithm and the inability to propose an artificial source term for the pressure equation in OpenFOAM. The velocity field is, in its most general form, denoted by,

$$\boldsymbol{u}_m^{MMS} = \begin{Bmatrix} A\cos(ax)\sin(by)\sin(cz) \\ B\sin(ax)\cos(by)\sin(cz) \\ C\sin(ax)\sin(by)\cos(cz) \end{Bmatrix}. \tag{B.5}$$

Where A, B, C are arbitrary coefficients and a, b, c wave numbers. For simplicity, the wave numbers are taken equal and as an integer multiple of π, $a = b = c = n\pi$ with $n \in \mathbb{Z}$. The coefficients of the components in the x and y direction are set as $A = B = \dfrac{u_{max}}{2} e^{-2t}$, such that a divergence-free velocity field can be retrieved using [68],

$$Aa + Bb + Cc = 0 \quad \Rightarrow \quad C = u_{max} e^{-2t}. \tag{B.6}$$

The final, divergence-free, manufactured mixture velocity is then denoted by,

$$\boldsymbol{u}_m^{MMS} = \begin{Bmatrix} \dfrac{u_{max}}{2} e^{-2t}\cos(n\pi x)\sin(n\pi y)\sin(n\pi z) \\ \dfrac{u_{max}}{2} e^{-2t}\sin(n\pi x)\cos(n\pi y)\sin(n\pi z) \\ u_{max} e^{-2t}\sin(n\pi x)\sin(n\pi y)\cos(n\pi z) \end{Bmatrix}. \tag{B.7}$$

B.3.2 Mixture Kinematic Pressure

The manufactured solution proposed for the mixture pressure field is the sum of the squares of the spatial coordinates,

$$p_m^{MMS} = x^2 + y^2 + z^2. \tag{B.8}$$

The field is applied for its twice differentiability in space, as required by the pressure equation supplied by the pressure-velocity coupling used in the PIMPLE algorithm [38],

$$\nabla \cdot \left(\frac{1}{\mathcal{A}^h_{\boldsymbol{u}_m}} \nabla p_m \right) = \nabla \cdot \left(\frac{\mathcal{H}^h_{\boldsymbol{u}_m}(\boldsymbol{u}_m)}{\mathcal{A}^h_{\boldsymbol{u}_m}} \right). \tag{B.9}$$

Where $\mathcal{H}^h_{\boldsymbol{u}_m}(\boldsymbol{u}_m)$ denotes the off-diagonal components of the coefficient matrix, multiplied by the vector of velocity solutions, and subtracted by the right-hand side of the system of equations.

B.3.3 Dispersed Phase Volume Fraction

The manufactured solution proposed for the dispersed phase volume fraction field will be the sum of the spatial coordinates and time squared, and divided by their maximum value,

$$\alpha_d^{MMS} = \frac{(x + y + z + t)^2}{\max(\alpha_d^{MMS})}. \tag{B.10}$$

The division restricts the solution to the interval $\alpha_d^{MMS} \in [0, 1]$ in order to retrieve relevant solutions for the mixture viscosity field presented in equation 5.10.

B.3.4 Oxygen Partial Pressure

The manufactured solution proposed for the oxygen partial pressure field is the sum of the spatial coordinates and time, divided by the sum of the squares of the spatial coordinates. A value of unity is additionally added to the denominator to prevent unbounded solutions as $x, y, z \to 0$, and the relation is scaled such that the maximum value is on the interval $P_{O_2}^{MM} \in [0, 120]$,

$$P_{O_2}^{MM} = \frac{120}{\max(P_{O_2}^{MM})} \frac{x + y + z + t}{x^2 + y^2 + z^2 + 1}. \tag{B.11}$$

The scaling allows the observation of $S_{O_2}(\max(P_{O_2}^{MM})) \to 1$.

Appendix C

OpenFOAM Code Implementations

This appendix provides the crucial code implementation listings used for the numerical analyses considered in this study.

C.1 Governing Relations

C.1.1 Conservation of Mixture Momentum

The conservation of mixture momentum implementation, corresponding to equation 8.4.

```
tmp<fvVectorMatrix> tUEqn
(
    fvm::ddt(U)
  + fvm::div(phi, U)
  - fvc::div(nu_m * dev2(T( fvc::grad(U))) )
  - fvm::laplacian(nu_m, U)
 ==
    fvOptions(U)
);
```

Listing C.1: Conservation of mixture momentum.

C.1.2 Conservation of Dispersed Phase Mass

The conservation of dispersed phase mass implementation, or migration model implementation, corresponding to equation 8.6.

```
fvScalarMatrix HtEqn
(
    fvm::ddt(Ht)
  + fvm::div(phi_, Ht)
  - K_c*sqr(a)*fvm::laplacian(Ht*shearRateMag_, Ht)
  - K_c*sqr(a)*fvc::laplacian(sqr(Ht), shearRateMag_)
  - K_mu*sqr(a)*fvc::laplacian(shearRateMag_*sqr(Ht)/nu_m_, nu_m_)
  ==
    fvOptions(Ht)
);
```

Listing C.2: Conservation of dispersed phase mass.

C.1.3 Conservation of Oxygen mass

The conservation of oxygen mass implementation, or oxygenation model implementation, corresponding to equation 8.7.

```
fvScalarMatrix PO2Eqn
(
    (1.0 + C_HbO2_) * (fvm::ddt(PO2) + fvm::div(phi_, PO2))
  - fvm::laplacian(D_eff_, PO2)
  ==
    fvOptions(PO2)
);
```

Listing C.3: Conservation of oxygen mass.

C.2 Boundary Conditions and Source Terms

C.2.1 Newtonian Inlet Velocity

The Newtonian inlet velocity implementation.

```
inlet
{
    type            codedFixedValue;
    value           uniform (0 0 9.55e-3);
    name            inletVelocity;
    code            #{
        const fvPatch& boundaryPatch = patch();
        const vectorField& Cf = boundaryPatch.Cf();
        vectorField& inletVelocity = *this;

        forAll(Cf, faceI)
        {
            const scalar y = Cf[faceI].y();
            const scalar x = Cf[faceI].x();

            const vector solU (0,0, 2*9.55e-3*(1 - sqr( sqrt(
                sqr(x) + sqr(y) ) / 50e-6) ));
            inletVelocity[faceI] = (solU);
        }
    #};
}
```

Listing C.4: Hagen-Poiseuille velocity profile.

C.2.2 No-Penetration Boundary Condition

The no-penetration boundary condition implementation, corresponding to equation 8.15.

```
wall
{
    type            codedMixed;
    refValue        uniform 0;
    refGradient     uniform 0;
    valueFraction   uniform 0;
    source          uniform 0;
```

```
    value           uniform 0;
    name            wallHematocrit;
    codeInclude     #{
        #include "fvCFD.H"
    #};
    code            #{
        // Get the reference of the mesh
        const fvMesh& mesh = patch().boundaryMesh().mesh();
        // Get the variable fields
        const volScalarField& Ht =
            db().lookupObject<volScalarField>("Ht");
        const volScalarField& shearRateMag =
            db().lookupObject<volScalarField>("shearRateMag");
        const volScalarField& nu_m =
            db().lookupObject<volScalarField>("nu_m");
        // Get temp gradient fields
        surfaceScalarField snGradGamma
        (
            IOobject
            (
                "snGradGamma",
                db().time().timePath(),
                db(),
                IOobject::NO_READ,
                IOobject::NO_WRITE
            ),
            mesh,
            dimensionedScalar("snGradGamma",
                dimless/dimTime/dimLength, 0.0)
        );
        surfaceScalarField snGradNu
        (
            IOobject
            (
                "snGradNu",
                db().time().timePath(),
                db(),
                IOobject::NO_READ,
                IOobject::NO_WRITE
            ),
            mesh,
            dimensionedScalar("snGradNu", dimViscosity/dimLength,
                0.0)
        );
        // Set temp gradient fields
        snGradGamma = fvc::snGrad(shearRateMag);
        snGradNu = fvc::snGrad(nu_m);
        // Get current patch object reference
        scalarField& field = *this;
        // Model coefficients
        const scalar Kc = 0.4;
        const scalar Km = 0.6;
        // outerCorrector coefficients
        const scalar Nx0 = 0.45;
        const scalar Ny0 = 0.5;
        const scalar Nx1 = 0.8;
```

```
59          const scalar Ny1 = 1.0;
60          const scalar& N =
               readScalar(db().lookupObject<IOdictionary>
            ("solverControlDict").lookup("outerCorrectorIndex"))
62          /readScalar(db().lookupObject<IOdictionary>
            ("solverControlDict").lookup("nOuterCorrectors"));
64          scalar fN = (Ny1-Ny0)*erf(2.0/(Nx1-Nx0)*(N-Nx0))+Ny0;
65          // Loop over patch faces
66          forAll(field, faceI)
67          {
68              const scalar Ht_I =
                   Ht.boundaryField()[patch().index()][faceI];
69              const scalar Y_I =
                   shearRateMag.boundaryField()[patch().index()][faceI];
70              const scalar gradY_I =
                   snGradGamma.boundaryField()[patch().index()][faceI];
71              const scalar Nu_I =
                   nu_m.boundaryField()[patch().index()][faceI];
72              const scalar gradNu_I =
                   snGradNu.boundaryField()[patch().index()][faceI];
73
74              this->refGrad()[faceI] = - fN * (1.0/Y_I * gradY_I +
                   Km/Kc * 1.0/Nu_I*gradNu_I)*Ht_I;
75          }
76      #};
77  }
```

Listing C.5: No-penetration boundary condition.

C.2.3 Cyclic Mixture Momentum Source

The cyclic mixture momentum source implementation.

```
1  momentumSource
2  {
3    type     meanVelocityForce;
4    active     true;
5
6    meanVelocityForceCoeffs
7    {
8      selectionMode    all;
9
10     fields       (U);
11     Ubar       (0 0 9.55e-3);
12   }
13 }
```

Listing C.6: Cyclic mixture momentum source.

C.3 Closure Models

C.3.1 Mixture Shear Rate Magnitude

The mixture shear rate magnitude implementation, corresponding to equation 5.2.

```
void setShearRateMagnitude(const volVectorField& U, const
    dimensionedScalar& baseShearRateMag, volScalarField&
    shearRateMag)
{
    // Set internal field velocity gradient
    const volTensorField gradU = fvc::grad(U);
    // Set strain rate tensor
    const volTensorField D = 0.5 * (gradU + gradU.T());
    // Set shear rate magnitude
    shearRateMag = sqrt(2 * (D && D)) + baseShearRateMag;
}
```

Listing C.7: Mixture shear rate magnitude.

C.3.2 Yeleswarapu-Wu Mixture Viscosity

The Yeleswarapu-Wu viscosity model implementation, corresponding to equation 5.10.

```
void setKinematicViscosity (volScalarField& nu_m) override
{
    // Set bounding viscosities
    // Get hematocrit powers
    const volScalarField Ht2_ = pow(Ht_,2);
    const volScalarField Ht3_ = pow(Ht_,3);
    // Get viscosities
    const volScalarField mu_0  = a1*Ht_ + a2*Ht2_ + a3*Ht3_;
    const volScalarField mu_00 = b1*Ht_ + b2*Ht2_ + b3*Ht3_;

    // Set log operand
    const volScalarField operand = 1.0 + k*(shearRateMag_ + y0);

    // Set kinematic viscosity
    nu_m = ((1.0 - Ht_)*mu_c + Ht_*(mu_00 + (mu_0 - mu_00)*(1.0 +
        log(operand))/operand))/rho_m;
}
```

Listing C.8: Yeleswarapu-Wu viscosity model.

C.3.3 Hill Equation

The Hill equation implementation and its derivative, corresponding to equations 7.8 and 8.8.

```
void setSaturation(const volScalarField& PO2, volScalarField&
    S_O2) override
{
    S_O2 = pow(PO2, n)/(pow(PO2, n) + pow(p_50, n));
}
```

Listing C.9: Hill equation.

```
void setSaturationChange(const volScalarField& PO2,
    volScalarField& dS_O2dPO2) override
{
     dS_O2dPO2 = n*pow(p_50, n)*pow(PO2, (n-1.0))/sqr(pow(PO2, n) +
        pow(p_50, n));
}
```

Listing C.10: Hill equation derivative.

Appendix D

Additional Blood Flow Modelling Considerations

This appendix considers two fluid model approaches to blood flow modelling deemed out-of-scope throughout the main body of the thesis.

D.1 Interphasic Interactions

D.1.1 Two-Fluid Model Interphasic Interactions

The most important interphasic interaction modelling consideration in a dispersed two-fluid model is the generalized drag force [48], which describes the total force exerted on the dispersed phase [70]. The total force should mathematically capture the physical response of the red blood cells to the fluidic behaviour of the blood plasma, as was described in section 2.3.2. The general approach of modelling is to consider the generalized drag force to consist of a linear combination of all important interfacial forces [48],

$$\mathcal{I}_{\boldsymbol{u}_d} = \frac{\alpha_d}{V_d}\left(\boldsymbol{F}_d^D + \boldsymbol{F}_d^V + \boldsymbol{F}_d^L + \cdots\right). \tag{D.1}$$

Where subscript d denotes the consideration of the dispersed phase, V_d the typical dispersed phase or particle volume, $\boldsymbol{F}_d^D$ the standard drag force, $\boldsymbol{F}_d^{VM}$ the virtual mass force, $\boldsymbol{F}_d^L$ the lift forces which will be discussed in more detail in chapter 6. Depending on the application, many other forces may be considered, such as [48, 53, 64, 75, 106]:

- **Pressure Gradient Forces:** These forces arise due to spatial variations in fluid pressure, causing particles to move towards regions of lower pressure.
- **Bassett Forces:** Bassett forces consider the influence of the particle's past motion on its current behaviour, contributing to inertial effects.
- **Faxén Forces:** Non-uniform flow Faxén forces arise from spatial variations in fluid velocity, influencing particle motion near boundaries or interfaces.
- **Magnus Forces:** Magnus forces occur when particles move toward regions of higher fluid velocity, resulting in their deviation from expected trajectories.
- **Turbulent Dispersion Forces:** Turbulent dispersion forces lead to the dispersion and mixing of particles in turbulent flows.
- **Buoyancy Forces:** Buoyancy forces are caused by the density difference between particles and the surrounding fluid, resulting in upward or downward forces.
- **Thermal, Chemical, or Electro-magnetic Interaction Forces:** These forces arise from particles and fluid interactions based on temperature, chemical composition, or electro-magnetic properties.

D.1.2 Drag Force

The standard drag force is that observed by particles under steady-state [75], and is in combination with the consideration of lift forces the most important type of force in consideration of blood flow [65]. Many different types of drag force models exist, but they generally fall into two flavours. The first flavour considers the drag force as a function of the drag coefficient [48, 70],

$$\boldsymbol{F}_d^D = -\frac{1}{2} C_{\boldsymbol{F}_d}^D(Re_d) A_d^P \boldsymbol{V}_{dj} |\boldsymbol{V}_{dj}|. \tag{D.2}$$

Where A_d^P denotes the projected area of the dispersed phase and C_d^D the drag coefficient for which numerous empirical relations are considered in [48, 70].
The second flavour considers the drag force as a function of a hindrance coefficient [53],

$$\boldsymbol{F}_d^D = \frac{9\overline{\overline{\mu}}_c}{2a_d^2} C_{\boldsymbol{F}_d}^H(\alpha_d) \boldsymbol{V}_r. \tag{D.3}$$

Where μ denotes the dynamic viscosity, a_d the characteristic particle size and C_d^H the hindrance coefficient for which several closure relations are available in [106].

D.1.3 Virtual Mass Force

The virtual mass force is exerted by the continuous phase on the dispersed phase due to acceleration of the dispersed phase with respect to the continuous phase [31]. The force may thus also be denoted the unsteady drag force and may be denoted by [31, 75],

$$\begin{aligned} \boldsymbol{F}_d^{VM} = C_{\boldsymbol{F}_d}^{VM,[0]}(\alpha_d) \overline{\overline{\rho}}_c V_d \Bigg(\frac{D_d \boldsymbol{V}_r}{Dt} + \boldsymbol{V}_r \cdot \Big[(C_{\boldsymbol{F}_d}^{VM,[1]}(\alpha_d) - 2) \nabla \otimes \widetilde{\boldsymbol{u}}_d \\ + \ (1 - C_{\boldsymbol{F}_d}^{VM,[1]}(\alpha_d)) \nabla \otimes \widetilde{\boldsymbol{u}}_c \Big] \Bigg). \end{aligned} \tag{D.4}$$

Where $C_{\boldsymbol{F}_d}^{VM,[0\wedge 1]}$ denote two model coefficients related to the interactions between the phases and the shape of the dispersed phase.

D.1.4 Drift-Flux Model Interphasic Interactions

The interphasic interactions for the drift-flux model in dispersed flows are generally modelled using the macroscopic phase diffusion flux, equation 3.21. This phasic drift flux can be closed directly or modelled through its relation to the relative phase motion as discussed in section 3.2.3.2.
The direct modelling of the flux is generally considered in studies where the migration of the dispersed phase is dominant and will be considered in more detail in chapter 6. In contrast, the relative motion is often modelled through the slip relation, which generally depends on the exact flow regime and flow type, i.e. sub-classifications of dispersed flows, under consideration and is modelled through a complicated combination of analytical and empirical considerations [73]. A variety of generalized algebraic and differential analytical models are discussed in [13] and empirical models in [48].
A more generalized, force-based approach is to derive the relative motion using the momentum equations for the dispersed phase and mixture in combination with the generalized drag force discussed in the previous section. Following [61], the mixture momentum conservation may be subtracted from the dispersed phase momentum conservation, where the sources and mixture interface contribution are generally neglected. Using the respective

mass conservation relations, neglecting the source and interface contributions, the relation for the generalized drag force may be denoted by,

$$\begin{aligned}\mathcal{I}_{\boldsymbol{u}_d}(\boldsymbol{V}_{dm}) = \alpha_d &\left[\overline{\overline{\rho}}_d \frac{\partial \boldsymbol{V}_{dm}}{\partial t} + (\overline{\overline{\rho}}_d - \rho_m)\frac{\partial \boldsymbol{u}_m}{\partial t}\right] \\ &+ \alpha_d \left[\overline{\overline{\rho}}_d \widetilde{\boldsymbol{u}}_d \cdot (\nabla \otimes \widetilde{\boldsymbol{u}}_d) - \rho_m \boldsymbol{u}_m \cdot (\nabla \otimes \boldsymbol{u}_m)\right] \\ &+ \nabla \cdot \left(\alpha_d \left[\overline{\overline{\boldsymbol{\mathcal{J}}}}_{\boldsymbol{u}_d} + \boldsymbol{\mathcal{J}}^T_{\boldsymbol{u}_d}\right]\right) - \alpha_d \nabla \cdot \left(\boldsymbol{\mathcal{J}}_{\boldsymbol{u}_m} + \boldsymbol{\mathcal{J}}^D_{\boldsymbol{u}_m} + \mathcal{J}^T_{\boldsymbol{u}_m}\right).\end{aligned} \tag{D.5}$$

Where it is assumed all forces included in the generalized drag force are related to the phase diffusion velocity, i.e. $\mathcal{I}_{\boldsymbol{u}_d} = \mathcal{I}_{\boldsymbol{u}_d}(\boldsymbol{V}_{dm})$, and $\widetilde{\boldsymbol{u}}_d$ in the temporal derivative was replaced using the phase diffusion velocity, see equation 3.18. $\otimes$ denotes the outer or dyadic vector product and $\nabla \otimes \boldsymbol{u}$ the velocity field gradient, often more concisely but mathematically inconsistent denoted by $\nabla \boldsymbol{u}$ [43]. To simplify the relation, it is generally assumed that the temporal derivative of the phase diffusion velocity, momentum diffusion contributions, and momentum drift contributions are negligible and that the advection contributions of the dispersed phase and mixture are roughly equal. The resulting generalized drag is then denoted by,

$$\mathcal{I}_{\boldsymbol{u}_d}(\boldsymbol{V}_{dm}) = \alpha_d(\overline{\overline{\rho}}_d - \rho_m)\left[\frac{\partial \boldsymbol{u}_m}{\partial t} - \boldsymbol{u}_m \cdot (\nabla \otimes \boldsymbol{u}_m)\right]. \tag{D.6}$$

Where the turbulent contributions were omitted, the resulting relation may now be used to approximate the phase diffusion velocity for the dispersed phase, which, depending on the included forces, should also be done numerically.

D.2 Rheology of whole blood

D.2.1 Thixotropy

Although the exact physical driving force behind the aggregation is unknown, as discussed in section 2.3.1, several models exist to simulate this time-dependent behavior [3, 46, 83]. These models commonly incorporate three factors to describe the response: shear breakage accounts for the breaking apart of rouleaux under shear rate [3]; shear aggregation describes the formation of rouleaux through particle interactions [83]; and Brownian aggregation characterizes the spontaneous aggregation of red blood cells due to Brownian motion [83]. The modelling of the thixotropic contribution to the mixture stress tensor is generally done through the consideration of the temporal change of a scalar quantity which describes the number of rouleaux present and is denoted by [3, 11],

$$\frac{d\lambda_r}{dt} = \frac{1}{C^{(0)}_{\lambda_r}}\left(\underbrace{-C^{(0)}_{\lambda_r}\lambda_r|\dot{\gamma}_p|}_{\substack{\text{Shear}\\ \text{breakage}}} + \underbrace{C^{(1)}_{\lambda_r}(1-\lambda_r)|\dot{\gamma}_p|^{\frac{1}{2}}}_{\substack{\text{Shear}\\ \text{aggregation}}} + \underbrace{(1-\lambda_r)}_{\substack{\text{Brownian}\\ \text{aggregation}}}\right) \tag{D.7}$$

Where λ_r denotes the scalar quantity ranging from 0 to 1, where zero indicates no observation of rouleaux and unity represents complete observation, $\dot{\gamma}_p$ the plastic contribution of the shear rate, and $C^{(0,1,2)}_{\lambda_r}$ are model coefficients associated with the build-up and breakdown of the rouleaux. The precise relationship between the mixture stress tensor and the thixotropic scalar quantity, as well as the determination of the plastic contribution of the shear rate, depend on the viscoelasticity and viscoplasticity of the mixture, which will be discussed in the following section.

D.2.2 Viscoelasticity

The modelling of the viscoelastic effects is generally a complicated matter due to its time-dependency, and most models do not contribute to the mixture viscosity, as was discussed for the shear-thinning, but rather a model for the complete mixture stress tensor. These models generally consist of a linear superposition of the viscoelastic contributions due to the behaviour of rouleaux along with those of isolated red blood cells, which are usually modelled through variations of Maxwell or Oldroyd-B viscoelasticity models [3, 46]. These models are typically complicated first-order inhomogeneous ordinary differential equations in time where, for example, the standard Oldroyd-B model is denoted by [113],

$$\boldsymbol{\sigma}_{O-B} + C^{(0)}_{\boldsymbol{\sigma}_{O-B}} \overset{\nabla}{\boldsymbol{\sigma}}_{O-B} = \mu_m(\mathcal{D}_m + C^{(1)}_{\boldsymbol{\sigma}_{O-B}} \overset{\nabla}{\mathcal{D}}_m). \tag{D.8}$$

Where $C^{(0\wedge 1)}_{\boldsymbol{\sigma}_{O-B}}$ respectively denote the characteristic relaxation and retardation times, and $\overset{\nabla}{(.)}$ the upper convected derivative denoted for an arbitrary quantity by [113],

$$\overset{\nabla}{\mathcal{F}} = \frac{\partial \mathcal{F}}{\partial t} + \boldsymbol{u} \cdot \nabla \mathcal{F} - (\nabla \boldsymbol{u}) T \cdot \mathcal{F} - \mathcal{F}(\nabla \boldsymbol{u}). \tag{D.9}$$

The contributions due to the viscoelasticity of the rouleaux may, in turn, be modelled as an ordinary differential equation dependent on the behaviour of the thixotropy [46],

$$\frac{d\boldsymbol{\sigma}_{r,ve}}{dt} = \begin{cases} G\lambda_r^{1.5}\left(\dot{\gamma}_p - \dfrac{\boldsymbol{\sigma}_{r,ve}}{\mu_R \lambda_r^{1.5}}\right) & \text{if } \dfrac{d\lambda_r}{dt} \geq 0, \\ G\lambda_r^{1.5}\left(\dot{\gamma}_p - \dfrac{\boldsymbol{\sigma}_{r,ve}}{\mu_R \lambda_r^{1.5}}\right) + 1.5\dfrac{\boldsymbol{\sigma}_{r,ve}}{\lambda_r}\dfrac{d\lambda_r}{dt} & \text{if } \dfrac{d\lambda_r}{dt} < 0. \end{cases} \tag{D.10}$$

Where G denotes the shear-modulus of the rouleaux and μ_R the rouleaux viscosity

D.2.3 Viscoplasticity

The Casson-type viscosity models are typically variations of the Sisko model and model viscoplasticity through the consideration of a yield stress. A Casson-type model in the consideration of blood flow is denoted by [22],

$$\mu_m = \left(\sqrt{\frac{\sigma_y^{VP}}{\dot{\gamma}_m}} + \mu_C\right)^2, \tag{D.11}$$

where,

$$\mu_C = \overline{\overline{\mu}}_c \left(1 + 2.0703\alpha_d + 3.722\alpha_d^2\right) \times \exp\left(-7.0276\left(1 - \frac{T_0}{T_b}\right)\right). \tag{D.12}$$

Further modelling approaches are extensively discussed in [11], [113].

D.3 Shear-Induced Migration Modelling of Red Blood Cells

D.3.1 Lift Force-Based Migration Modelling

The constitutive momentum modelling for a dispersed two-phase flow was discussed in chapter 4. Additionally, it was shown in appendix D.1 how various dynamical effects can be included through force-based modelling using a generalized drag force, see equation

D.1. While this methodology extends to modelling the migration mechanisms in blood, its utilization within the continuum modelling literature for whole blood appears limited. The relevant literature adopting such a force-based modelling methodology, including work such as [53, 54, 65], predominantly considered the two-fluid model described in section D.1.1, and primarily included the standard drag force and a shear-induced lift force.
The shear-induced lift force is related to the velocity profile-induced particle lift as was discussed in section 6.1.2, and may be modelled using a generalized Saffman lift force, which is denoted by [53],

$$\boldsymbol{F}_d^L = C_{\boldsymbol{F}_d}^S(\rho_c, \mu_c, a_d)|\boldsymbol{\mathcal{D}}_c|^{\frac{1}{2}}\boldsymbol{\mathcal{D}}_c\boldsymbol{V}_r. \tag{D.13}$$

Where $C_{\boldsymbol{F}_d}^S(\rho_c, \mu_c, a_d)$ denotes a model coefficient characterizing the generalized Saffman-lift force. Additionally, the spin-lift force was also considered in [53], where the spin-lift force is induced by the rotation of the particle around the major axis, as was discussed for red blood cells in section 2.3.2. However, the order-of-magnitude analysis showed that this is generally negligible compared to the shear-induced lift forces [65].
Lastly, the force induced by shear-induced diffusion can be modelled by [65],

$$\boldsymbol{F}_d^{SID} = C_{\boldsymbol{F}_d}^{SID}\nabla\alpha_d. \tag{D.14}$$

Where $C_{\boldsymbol{F}_d}^{SID}$ denotes a model constant.

D.3.2 Mathematical Model Equivalence

In addition to the model equivalence presented in section 6.4, the particle migration models can also be rewritten in the interest of force-based modelling. The shear-induced migration force is then denoted by [28],

$$\boldsymbol{F}_d^{SIM} = -\nabla\mu^*. \tag{D.15}$$